THE EFFECTS OF MINERALIZATION AND CRYSTALLINITY ON THE MECHANICAL BEHAVIOR OF BONE

A Dissertation

Presented to the Faculty of the Graduate School

of Cornell University

in Partial Fulfillment of the Requirements for the Degree of

Doctor of Philosophy

by

Grace Kim

May 2013

THE EFFECTS OF MINERALIZATION AND CRYSTALLINITY ON THE MECHANICAL BEHAVIOR OF BONE

Grace Kim, Ph.D.

Cornell University 2013

The application of engineering theory and analysis to bone has led to many insights regarding the etiology of increased skeletal fragility with aging and diseases such as osteoporosis. According to mechanics of materials theory, whole bone mechanical behavior should depend on the amount of bone tissue, bone geometry, and tissue material properties. Through the use of micro-computed tomography, the influence of bone mass and geometry on whole bone strength and stiffness have been confirmed and quantified. With the application of nanoindentation to the study of bone, the ability to measure the mechanical properties of bone at the micron length scale is now possible. However, most studies using nanoindentation have focused only on tissue-level properties and, therefore, relatively little is known about the relationships between tissue-level properties and whole bone mechanical behavior. The objectives of this research were to 1) examine the effects of two composition changes, mineralization and crystallinity, on whole bone and tissue-level mechanical behavior, and 2) examine changes in tissue-level composition and mechanical properties due to osteoporosis.

To investigate the effects of mineralization and crystallinity independently, two separate dietary interventions in rodents were used. First, vitamin D deficiency in growing rats was used to reduce cortical bone mineralization. The vitamin D deficient animals had compromised whole bone mechanical behav-

ior, as indicated by the lower failure moment and bending stiffness. To take into account the mechanical property heterogeneity and cortex geometry when predicting whole bone mechanical behavior, a density-weighted section modulus was calculated using composite beam theory. The weighted section moduli predicted whole bone mechanical behavior better than geometric parameters or average mechanical properties alone.

In the second study, growing rats given fluoride had increased cortical bone crystallinity and reduced measures of whole bone mechanical behavior. Cortical cross-sectional geometry was not different with fluoride, implying a difference in mechanical properties was responsible for the altered whole bone mechanical behavior; however, indentation modulus and hardness were not different. The discrepancies between tissue-level and whole bone mechanical behavior suggest that interfaces between microstructural features and other mesoscale features influence whole bone mechanical behavior.

In the third study, tissue-level composition and mechanical properties of osteoporotic cancellous bone from a fracture prone location were examined. Vertebral cancellous bone from female cadavers was divided into two groups, osteoporotic and not osteoporotic based on T-scores from dual-energy x-ray absorptiometry scans. Tissue from osteoporotic donors had lower indentation moduli and showed a trend towards being less mineralized compared to tissue from normal and osteopenic individuals. Independent of reduced bone mass and altered trabecular architecture, lower indentation moduli of osteoporotic bone could contribute to skeletal fragility associated with osteoporosis.

BIOGRAPHICAL SKETCH

Grace Kim was born in San Francisco, California and raised in the Bay Area. Her love of science was evident from a young age and kindled by her father, Johann, who encouraged her to take apart perfectly functioning household items and toys to see how they worked, set things on fire for the sake of science, and create glowing concoctions of slightly questionable chemicals. She attended the University of California, Berkeley, torn between majoring in biology and mechanical engineering. In the end, Grace decided to pursue mechanical engineering and through her undergraduate coursework also found an interest in material science. During her undergraduate career, she had the opportunity to combine engineering with her interest in biology through laboratory research involving the mechanical properties of mineralized tissues. In 2006, Grace graduated with a Bachelor's of Science in Mechanical Engineering and Materials Science. In 2007 she enrolled in the Master's of Engineering program at Cornell University and started on a research project in the van der Meulen laboratory. A few degree changes later, she received her Ph.D in mechanical engineering in May 2013.

Though not about designing airplanes,

I dedicate this work to Young-Ran Hong.

ACKNOWLEDGEMENTS

This research would not have been possible without the help of many people. First and foremost I would like to thank my committee chair, Dr. Marjolein van der Meulen, for the opportunity to pursue a Ph.D, her scientific knowledge, and mentorship. I would also like to thank committee members Dr. Shefford Baker and Dr. Adele Boskey for their expert technical knowledge and guidance over the years.

Lab members past and present, Maureen Lynch, Jayme Burket, Garry Brock, Frank Ko, and Katie Melville, as well as students and faculty members of the biomechanics group for providing assistance and valuable feedback on research presentations and conference abstracts. I would like to thank John Grazul, John Hunt, Kit Umbach, and Mark Riccio for instrument training and technical advice, Hystitron Inc. for use of the nanoindenter and Cornell CARE staff for help with the animal studies. Judy Thoroughman and Marcia Sawyer, thank you for your support and help navigating the sea of forms and requirements.

Maureen Lynch and Natalie Galley, thank you for your technical and non-technical advice, the many lasting memories and wonderful friendship. I wouldn't have made it this far without the two of you. Natalie, your advice as a former resident of the Tundra was invaluable to this Californian for surviving the winters.

Anna Legard, Brendan Murday, and Miki Kunitake, thank you for your generosity, hospitality and sharing many wonderful meals and memories with me. Alwin Wan, thank you for believing in the winningest bacon. Our many two wheeled adventures helped me see the beauty of upstate New York. Your scientific story-telling and problem solving abilities will always be something I aspire to. Melissa Takahashi, thank you for always being there for me with your calm

and level-headedness when I needed it most. My parents for their boundless love and support, most frequently embodied by words of encouragement over the phone and USPS flat rate boxes full of Trader Joe's snacks.

Funding for this research was provided by NIH/NAIMS grant R01-AR053571, R01-AR041325 and P30-AR046121. This work made use of the Cornell Center for Materials Research Facilities supported by the National Science Foundation under Award Number DMR-0520404.

TABLE OF CONTENTS

LIST OF TABLES

LIST OF FIGURES

CHAPTER 1

INTRODUCTION

Bone is a hierarchically organized tissue that serves two primary functions in the body. Bone is a mineral reservoir, storing and providing vital minerals such as calcium, magnesium, and phosphorus for the body [1]. The skeleton is also a load bearing organ that protects internal organs and enables locomotion in concert with skeletal muscles, tendons and ligaments. When considering bone as a load bearing structure, engineering approaches that are commonly used to analyze man-made structures can also be applied to bone. Three main factors determine the load bearing ability of a structure: the amount of material used, the spatial arrangement of the material, and the mechanical properties of the material. Mechanics of materials theory can predict the strength and stiffness of a structure based on geometry and mechanical properties.

1.1 Bone Composition and Microstructure

Bone, along with wood, seashells, and fish scales, can be thought of as naturally occurring composite materials in the sense that two disparate constituents are combined in a specific manner to optimize strength, stiffness, toughness, and weight. Like engineered composites, the mechanical performance of bone depends on the composition of the constituents and their organization. On average bone tissue is composed of 43% mineral, 25% water, and 32% organic matrix by volume [2]. The mineral portion is comprised of plate-like hydroxyapatite crystals similar in composition to geological hydroxyapatite but with substitutions including, carbonate, fluoride, and citrate. The organic matrix is primarily

(90%) composed of type I collagen in addition to proteoglycans and other non-collagenous proteins [3]. However, unlike engineering materials, bone is a living organ with cells that regulate bone modeling, remodeling, and adaptation in concert. Three types of cells exist in bone: osteoblasts, osteocytes and osteoclasts. Osteoid, the unmineralized substance laid down by osteoblasts, mineralizes and surrounds the osteoblasts in a mineralized matrix. Once osteoblasts are trapped into the matrix, they mature into osteocytes residing in small voids in the bone matrix known as lacunae. Radiating from each lacuna are small channels, canaliculi, that contain osteocyte processes. The vast canalicular network connects lacunae throughout the bone matrix connecting osteocytes with each other and vasculature.[4, 5].

Bone has structural features that span 6 orders of magnitude, from the size and shape of individual mineral crystals, to varying cross-sectional geometry of whole bones [6–8]. Type I collagen molecules present in bone are aligned in a staggered array forming fibrils. Collagen fibrils provide a template for mineralization [9–11]. The mineral crystals are organized such that their c-axis is in the same direction as the long axis of the collagen fibrils [2, 12]. The collagen fibrils align and form larger fibers that are oriented in a specific manner depending on the microstructure of the bone tissue. In healthy bone tissue, the collagen fibers for layer like structures known as lamellae. The combined organic matrix and mineral in bone create a composite structure that enables bone to be an extremely efficient load bearing structure that is both stiff and tough.

Macroscopically the two main types of bone structures found in the healthy skeleton, cortical and cancellous, can be distinguished based on their porosity. Cortical bone is found along the shafts of long bones and has a porosity of

5-10%, while the highly porous cancellous bone is found in the ends of longs bones and in vertebral bodies, with porosities ranging from 75-95% [3]. Bone can also be distinguished by its microstructure, woven and lamellar. Woven bone in adults is only found in fracture calluses. Lamellae in remodeled cortical bone is found in cylindrical structures called osteons. The osteonal structure arises from bone remodeling and appears as circumferential lamellae around a Haversian canal containing blood vessels and nerves, with alternating regions of highly aligned and less aligned collagen [13–15]. In cancellous bone the lamellae do not form osteons, trabeculae have a distinctly layered structure. Ultimately the composition and structural features, ranging from the microscale to the macroscale contribute to bone's mechanical behavior.

1.2 The Mechanical Properties of Bone

Determining the mechanical properties of bone tissue requires considering the hierarchical organization of bone. The measured mechanical properties depend on the length scale of testing. There are three main methods used to measure bone mechanical properties, whole bone testing, microbeam/core testing, and nanoindentation. Whole bone testing is the largest length scale and uses an entire bone. Common loading modalities include 3 or 4 point bending, compression, tension, and torsion. Bone geometry and beam theory are used to calculate the strength and Young's modulus from load-displacement curves. Variations in bone cross-sectional geometry, compositional heterogeneities, and porosity violate many of the assumptions required when using beam theory to calculate mechanical properties.

Prismatic beams or cylinders with regular cross sections can be cut from larger portions of cortical or cancellous bone and can be tested using the same loading modes as whole bone testing. Using microbeams/cores eliminates errors due to irregular and varying cross-sectional geometries. Tests using microbeams/cores measure what are known as apparent level mechanical properties. Young's modulus of cortical bone from C57/B6 mice assessed from cortical microbeams was nearly 3 times larger than values calculated from whole bone bending tests, 10 GPa compared to 3 GPa [16, 17]. The larger modulus values from microbeam testing are due to elimination of errors associated with the geometric irregularities of whole bones as validated by finite element models [18]. However, apparent level mechanical properties measure from microbeam testing is still affected the amount of discontinuities in the tissue such as pores, blood, vessels, and lacunae.

Nanoindetation can measure the mechanical properties of bone at the submicron length scale while avoiding surface discontinuities. Bone samples must be dehydrated, embedded and polished to avoid effects of surface roughness on measurements [19]. Again considering values from cortical bone of the C57B6 mouse, the Young's modulus from nanoindentation is 29 GPa, or nearly 3 times larger than values from microbeam testing [20]. However, up to 16% of the increase may be due to dehydration of the sample [21]. Additionally, heterogeneities due to tissue microstructure and discontinuities such as cellular lacunae and blood vessels are presumably the reason that modulus values derived from indentation tests are larger than those from microbeam testing [19–23].

1.2.1 Composition and Mechanical Properties at the Apparent Level

Much of the literature examining bone material properties has focused on the apparent level through the use of machined samples of cortical and cancellous bone. Although apparent level measurements of mechanical properties do not take into account heterogeneities due to tissue microstructure, many important relationships between apparent level composition, porosity and mechanical properties have been established in these studies. Utilizing the natural variation in mineral content and porosity of bones from different species, Currey found that that mineralization and porosity were correlated with Young's modulus and together were able to predict over 80% of the variation in Young's modulus [24]. Even within a single species apparent density, a function of porosity and mineralization, was correlated with Young's modulus and strength [25–27]. Mineralization also plays an integral role beyond the elastic behavior of bone as the yield and ultimate stresses of cortical bone have also been shown to decrease with decreasing mineral content [28–30].

Although much more compliant than hydroxyapatite, 1-2 MPa for type I collagen versus 150 GPa for a single crystal of hydroxyapatite, collagen plays an important role the post-yield behavior of bone [31, 32]. Studies using in vitro methods of altering collagen have shown dramatic effects on the strength and toughness of bone but not Young's modulus. Using either heat or enzymatic digestion to systematically denature collagen lowered the strength and toughness of cortical bone while the Young's modulus remained unchanged [30, 33]. Because collagen comprises $\sim$ 30% of bone tissue by volume, it is not surprising that destroying the collagen network has a substantial effect on the

mechanical behavior of bone tissue. Interestingly, even subtle changes to the collagen network can change the mechanical behavior of bone. Collagen cross-links form naturally between fibrils, stabilizing the collagen matrix [34]. The use of non-enzymatic glycation to alter collagen cross-linking of the collagen network in vitro increased the yield stress of bone without changes in stiffness [35]. On the other hand, inhibiting collagen cross-linking in vivo using β-amino-propionitrile in rats reduced cortical and cancellous bone strength and stiffness [36, 37]. Although the relationship between collagen cross-linking and mechanical properties is not straight forward, the importance of cross-links are clear. Because the collagen fibril network is vital to the mineralization process, changes in the mineral phase may also occur concurrently with collagen changes in vivo.

1.2.2 Tissue-Level Mechanical Properties and Composition

Apparent level tests have provided insights regarding the relationships between composition and mechanical properties, and whole bone mechanical behavior is ultimately of clinical interest. To identify the effects of microscale heterogeneities in composition due to microstructural constituents, and discontinuities such as cellular lacunae and blood vessels, a testing methodology with higher resolution is needed. The importance of the local changes in material properties are evidenced in the behavior of cracks propagating through bone tissue [38, 39] (Figure 1.1).

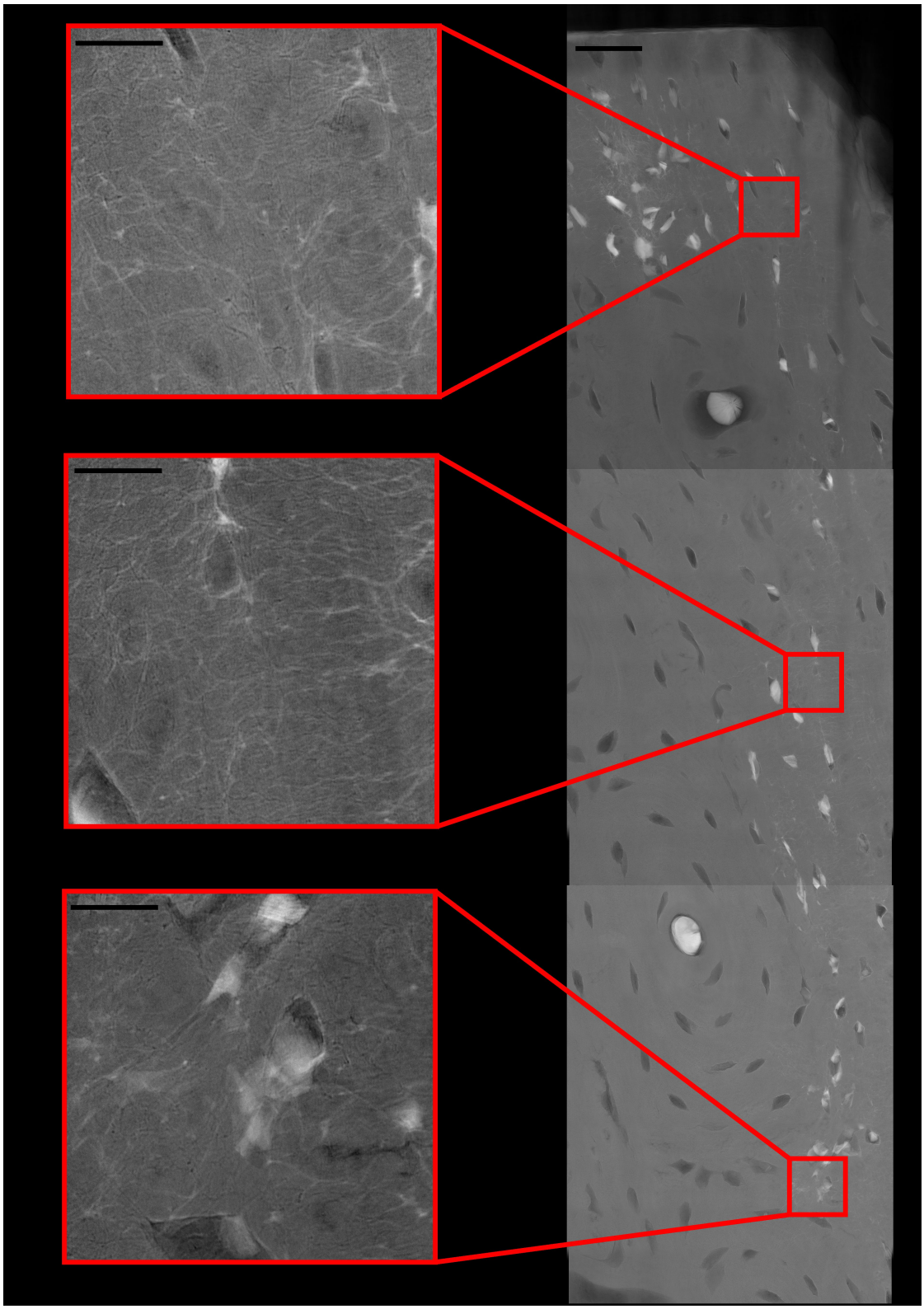

Figure 1.1: Transmission x-ray image of bone stained with lead-uranyl acetate. Damage (white) influenced by the osteonal tissue microstructure. Image courtesy of Garry Brock.

Composition Using Raman Microspectroscopy

Compositional analyses of bone, particularly of the mineral portion, have been assessed by ashing. However this technique is clearly destructive and cannot provide information about the spatial variation in mineralization. Calibrated microcomputed tomography (microCT) scans of bones can provide spatially resolved and average values of mineralization [40]. In addition to voxel-by-voxel values of mineralization, cortical geometry and trabecular architecture can also be quantified with isotropic voxel sizes smaller than 1μm [8]. Although microCT scans can compute average and spatially resolved mineralization data, no information is provided about the non-mineral components of bone or chemical changes within the mineral component such as carbonate substitution, collagen cross-linking or crystallinity.

Vibrational spectroscopy can provide compositional information about both the mineral and organic phase of bone with $1 - 10\mu$m spatial resolution. The most common forms of vibrational spectroscopy used to assess bone composition are Fourier Transform Infra-red (FTIR) and Raman microspectroscopy. Both spectroscopic methods provide complementary compositional data. Raman spectroscopy has higher spatial resolution than FTIR spectroscopy and can be done on in bulk samples negating the need for thin sections. Raman spectroscopy works on the basis of inelastically scattered light from the sample due to interactions of incident photons with molecular bonds in the sample. The phosphate ν_1 ($957cm^{-1}$) and carbonate peak ($1065cm^{-1}$) intensities and the full width half max (FWHM) of the phosphate ν_1 peak are commonly reported parameters that characterize the mineral portion of bone. Peaks that are related to the organic matrix include the Amide I ($1650cm^{-1}$) and CH_2 ($1447cm^{-1}$) wag

peaks. Compositional parameters are reported as peak height or peak area ratios. Common ratios include the mineral to matrix ratio ($957cm^{-1}$/ $1650cm^{-1}$) or $957cm^{-1}$/ $1447cm^{-1}$, B-type carbonate substitution ($1065cm^{-1}$/ $957cm^{-1}$), and mineral crystallinity (FWHM of $957cm^{-1}$) [41, 42]. The carbonate substitution measured by Raman is indicative of only B-type carbonate substitution while FTIR measures both labile, A-type and B-type carbonate [43].

Mechanical Properties Using Nanoindentation

The advent of depth sensing indentation and Oliver and Pharr's seminal paper in 1992 increased the use of nanoindentation to measure mechanical properties of bone at the submicron length scale [44] (Figure 1.2). Quasistatic nanoindentation tests are performed by loading and unloading an indenter with known tip geometry into a sample while monitoring the load and displacement. Scanning nanoindenters can resolve mechanical properties at the submicron length scale while enabling the placement of indentations on specific bone microstructures by acquiring topographical scans of the test location [13, 45–47]. The load displacement curves from depth sensing indentation devices are analyzed using the Oliver-Pharr method to calculate the indentation modulus (E_i) and hardness (H) [44]. Though a Young's Modulus for the sample can be calculated, this requires choosing a Poisson's ratio. From apparent level measurements, the Poisson's ratio for cortical bone is approximately 0.37 and has a variability of 30%, but depends on the orientation of the microstructure [3, 48]. Fortunately altering the Poisson's ratio by ±0.1 changes the Young's modulus by less than 10% [49, 50]. However this does not account for bone's anisotropic nature. Instead, the indentation modulus can be reported without assuming a Poisson's

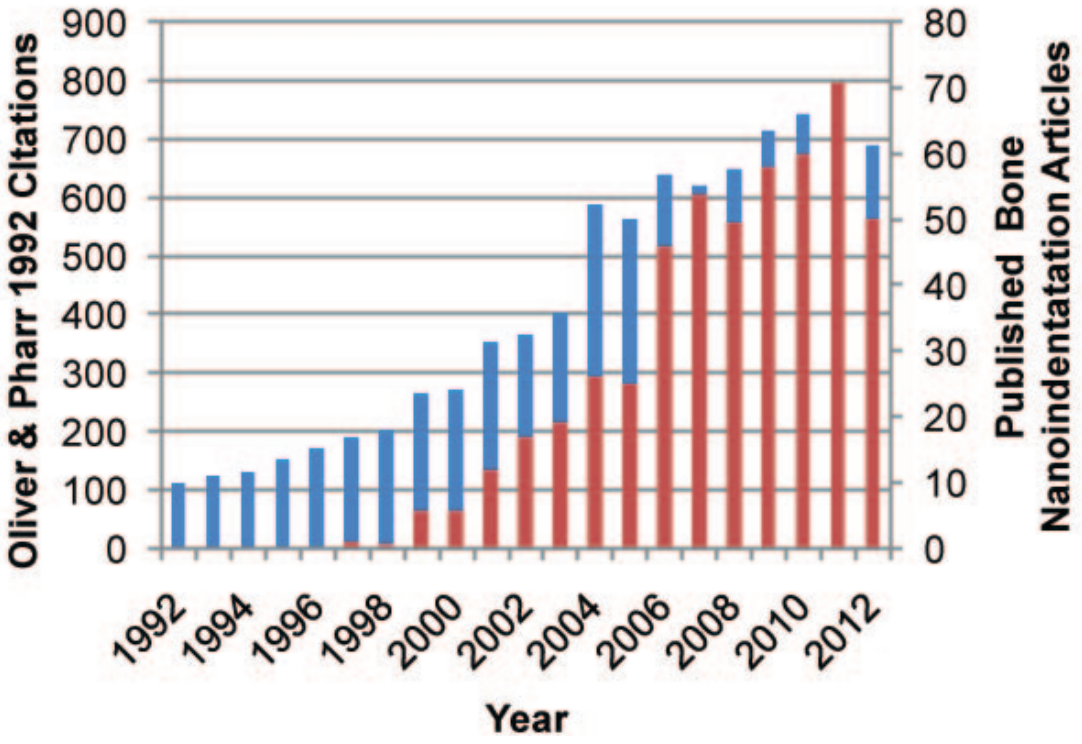

Figure 1.2: Blue bars represent the number of articles citing Oliver and Pharr 1992. Red bars represent the number of article published each year using nanoindentation to the mechanical properties of bone. Citation found using ISI Web of Science.

ratio as the indentation modulus is a function of both the Young's Modulus and Poisson's ratio. Where E_r is the reduced modulus, E and ν are the Young's modulus and Poisson's ratio of the sample and E_tip and ν_tip are the Young's modulus and Poisson's ratio of the indenter tip and the slope of the unloading curve is related to the reduced modulus [44].

$$E_i = \frac{E}{1-\nu^2} = \frac{1}{\frac{1}{E_r} - \frac{1-\nu_{tip}^2}{E_{tip}}} \tag{1.1}$$

Nanoindentation has been able to resolve the mechanical properties of specific microstructural features such as lamellar and interlamellar tissue, and interstitial and osteonal tissue [13, 46, 51–54]. The aforementioned microstructural

features have differences in composition that were associated with the differences in mechanical behavior. For instance, the lamellar regions have more aligned collagen than interlamellar regions [13], and interstitial bone is more mineralized than osteonal bone [54]. Additionally some studies have used the natural gradient in tissue age that occurs radially in growing rodents to correlate tissue-level mechanical properties to compositional parameters, specifically mineralization and carbonate substitution [55–57]. These studies demonstrated the ability of nanoindentation to resolve mechanical properties at a length scale smaller than most microstructural features of bone and changes in tissue-level mechanical properties are correlated with compositional changes.

1.3 Changes in Material Properties with Osteoporosis and Aging

Bone is a heterogeneous tissue that varies not only spatially, but temporally as well. Many studies have quantified the detrimental effects of aging on the mechanical competence of both cortical and cancellous bone. Apparent level strength, stiffness, and toughness of cortical and cancellous bone all decline with age after the 3rd to 5th decade of life [58–64]. Changes in the apparent level mechanical properties are associated with age related increases in porosity and reduced collagen content and apparent density [58–64], again highlighting the importance of architecture, porosity and composition. However, as previously stated, apparent level compositional measurements cannot resolve changes in composition to individual microstructural features.

The age of a volume of bone the tissue within the skeleton may not be equal

to the age to the donor or animal due to bone growth and remodeling. Thus within temporal changes, the difference between animal age and tissue age must be considered. In rodents, long bones grow via appositional growth with minimal remodeling creating a radial gradient in tissue age. Increases in mineralization and carbonate substitution, indentation modulus and hardness were associated with increasing tissue age [55–57]. Differences in both composition and mechanical properties as assessed by nanoindentation and vibrational spectroscopy change with tissue age and animal age [47].

The effect of osteoporosis on tissue-level mechanical properties is less clear, though studies have found a variety of compositional changes associated with osteoporosis. Osteoporosis was initially considered a disease only characterized by low bone mass, however, the occurrence of fragility fractures in individuals with normal bone mineral density as measured by dual x-ray absorptiometry (DXA) suggest changes in tissue-level material properties occur and may be crucial to increased fracture risk. Indeed, a variety of different compositional changes have been found to occur with osteoporosis at the tissue-level. Changes in collagen cross-link ratios [65], decreased mineralization and carbonate substitution heterogeneity [66] have been reported in samples from donors with fragility fractures compared to samples from donors without previous fragility fracture. Reduced bone mineralization [67], and increased carbonate substitution and crystallinity have also been associated with osteoporosis [68, 69].

Many studies have examined compositional changes with osteoporosis, but far fewer studies have examined changes in mechanical properties with osteoporosis. From the few that exist, mechanical properties appear not to change with osteoporosis. Indentation modulus and hardness did not differ between

sample from donors with and without femoral neck fractures despite decreases in mineralization as measured by quantitative backscattered electron imaging (qBEI) [70]. Additionally, cancellous bone from donors with preexisting vertebral fractures did not have different nanomechanical properties based on iliac crest cancellous bone sample [71]. The existing studies examining changes in mechanical properties with osteoporosis suggest changes at cortical sites may differ from those at cancellous site due differences in metabolic activity and changes in tissue material properties may not be uniform across cancellous sites [72, 73]. Additional studies examining tissue-level mechanical properties from other fracture prone sites such as the vertebrae and wrist would be insightful.

1.4 Relating Material Properties to Whole Bone Mechanical Behavior

From an engineering perspective, tissue-level mechanical properties should contribute to whole bone mechanical behavior. However the relationship between the mechanical responses of bone at vastly different length scales is not always clear due to the heterogeneous nature of bone tissue. Differences in mechanical properties of microstructural features have been measured using nanoindentation including a 31% difference in indentation modulus between lamellar and interlamellar tissue, and a 15% difference between osteonal and interstitial tissue. Typical test volumes for nanoindentation are on the order of microns and it is unrealistic to test enough locations that the total test volume approaches the volume used for whole bone testing. Even if the entire cortex could be tested, it is not clear which features of the tissue microstructure are

most influential to whole bone mechanical behavior. Most studies have averaged multiple nanoscale mechanical properties measurements to obtain a single value per sample that can be compared to outcomes of whole or apparent level mechanical testing. Based on studies combining whole bone mechanical testing and nanoindentation, whole bone mechanical behavior does not always correlate with average tissue-level material properties. In a hind-limb suspension study in rats, a 48% reduction in whole bone stiffness was not accompanied by a change in mechanical properties as assessed by nanoindentation [74]. In vitamin D deficient rats, whole bone stiffness was reduced 47% without a difference in indentation modulus [57]. A study on cortical bone from the senescence accelerated mouse, SAMP6, found reduced Young's Modulus and ultimate strength from whole bone tests, and increased indentation modulus and hardness from tissue-level indentation tests compared with SAMR1 control mice [20]. Upon first inspection the inconsistent correlation between whole bone and tissue-level properties is surprising; however this finding draws attention to the fact mechanical properties must be considered in conjunction with microstructure and tissue heterogeneities are neglected when averaging tissue-level data.

Though in vivo models are more clinically relevant than in vitro models, they include additional complexities due to the systemic effects and compensatory mechanisms. Modifying bone composition through dietary or genetic means is often accompanied by changes in bone geometry and mass. In the oim/oim mouse, a mouse model of osteogenesis imperfecta, reduced collagen content and collagen defects were accompanied by reductions in femur length and moment of inertia [75]. In the senescence accelerated SAMP6 mouse, both bone mineralization and the moment of inertia increased [76]. Similarly, vitamin D deficiency in rats reduced bone mineralization and cross-sectional area

[57, 77, 78]. Unlike traditional engineering structures, altering a single factor of bone strength in in vivo models becomes difficult, thus material properties, bone mass and architecture must all be considered concurrently to understand the contribution of a single factor to bone strength.

1.5 Study Objectives and Approaches

The importance of bone tissue composition of both the mineral and organic constituents of bone has been demonstrated at the apparent level, and several studies have indicated a similar composition-mechanical property relationship at the tissue-level [13, 15, 55, 56, 79]. However, very few studies have examined the relationship between tissue-level mechanical properties and whole bone mechanical behavior. Changes in mineralization and crystallinity have been confirmed with aging and osteoporosis, both of which alter apparent level mechanical behavior. Thus the objectives of this research were: First, to further the understanding of the effects of mineralization and crystallinity on tissue-level mechanical properties by using an in vivo model with dietary interventions to carefully control tissue composition, second, to relate tissue level-mechanical properties to whole bone mechanical behavior by using both microscale and macroscale mechanical testing techniques, third, to examine composition-mechanical property relationships in a more complex but clinically relevant sample of osteoporotic human cancellous bone.

For the first objective, the effect of mineralization on whole bone mechanical behavior and tissue-level mechanical properties were investigated. We hypothesized that mineralization influences both tissue-level properties and whole

bone mechanical behavior and that taking into account spatial heterogeneity of mechanical properties would improve predictions of whole bone mechanical behavior. Mineralization was reduced through the use of a vitamin D deficient diet in growing rats. Whole bone tissue mineralization and cross-sectional geometry were reduced in the experimental groups compared to controls. Whole bone mechanical behavior was altered as indicated by reduced bending stiffness and failure moment. At the tissue-level, the indentation modulus and hardness increased with tissue age, but no differences due to dietary intervention were measured. Additionally across the entire cortex, the mineral:matrix ratio was correlated with the indentation modulus. Average tissue-level mechanical properties were not correlated with whole bone mechanical behavior. Composite beam theory and the intrinsic tissue-level relationship between mineralization and indentation modulus were used to improve predictions of whole bone mechanical behavior. This study demonstrated that in a model for varying mineralization, a composite beam model using tissue-level data better predicted whole bone mechanical behavior than averaged tissue-level properties.

For the second objective, the effects of mineral crystallinity on whole bone mechanical behavior and tissue-level material properties were investigated. The effects of crystallinity on tissue-level mechanical properties have not been examined, however, their importance has been hypothesized [68]. We hypothesized increased crystallinity would reduce measures of tissue-level mechanical properties and whole bone mechanical behavior. Fluoride was given rats during a period of rapid growth and bone formation to alter crystallinity in vivo. Whole bone mechanical behavior was altered in fluoride treated animals without associated changes in cross-sectional geometry and whole bone mineralization based on microCT scans. In whole bone tests, fluoride treatment reduced the

bending stiffness and failure moment while increasing the total deformation. At the tissue-level, the mechanical behavior changed in a non-monotonic manner, the indentation modulus and hardness increased in tissue from animals given the lower dose of fluoride but no change was present in the higher dose group compared with controls. The mineral:matrix ratio as measured by Raman spectroscopy followed a trend similar to the indentation outcomes, increasing in the lower fluoride group. The difference in trends between tissue-level mechanical properties and whole bone mechanical behavior suggested that interactions between tissue constituents and microarchitectural features could be affected by changes in crystallinity and that those interactions influence whole bone mechanical behavior.

For the third objective, the same techniques used to assess tissue-level properties were applied to a more complex, yet clinically relevant system, cancellous bone from female human vertebrae. We hypothesized that there are material level changes associated with osteoporosis at anatomic locations prone to fracture, and that changes in mechanical properties are related to changes in composition. In this study, the effects of osteoporosis on the tissue-level mechanical properties and correlate any changes in mechanical properties with compositional changes, at a fracture prone location. Osteoporotic status was defined from aBMD measurements from DXA scans of the L1-L4 vertebrae. Cores of cancellous bone were prepared from the T12 vertebrae and used for tissue-level analyses. Compositional parameters, mineral:matrix ratio, crystallinity, and carbonate substitution, were measured using Raman spectroscopy, and tissue-level mechanical properties were assessed using nanoindentation. The indentation modulus of osteoporotic cancellous bone was reduced compared to osteopenic and normal samples and correlated with tissue-level mineralization. The ad-

dition of more compositional measures in addition to the mineral:matrix ratio improved the predictions for the indentation modulus and hardness. To our knowledge, this tissue-level study is the first examine cancellous bone from a fracture prone location. The reduction in the indentation modulus associated with osteoporosis as indicated by areal bone mineral density (aBMD) supports the idea that osteoporosis related changes in mechanical properties in addition to changes in bone mass and architecture contribute to increased fracture risk.

References

1. Harris WH and Heaney RP. Skeletal renewal and metabolic bone disease. New England Journal of Medicine 1969;280:193–202.

2. Robinson RA and Elliott SR. The Water Content of Bone I. The Mass of Water, Inorganic Crystals, Organic Matrin, and CO2 Space Components in a Unit Volume of Dog Bone. The Journal of Bone and Joint Surgery 1957;39:167–188.

3. Martin RB, Burr DB, and Sharkey NA. Skeletal Tissue Mechanics. Springer, 1998.

4. Burger EH and Klein-Nulend J. Mechanotransduction in bonerole of the lacuno-canalicular network. The Journal of the Federation of American Societies for Experimental Biology 1999;13:S101–S112.

5. Duncan RL and Turner CH. Mechanotransduction and the functional response of bone to mechanical strain. Calcified Tissue International 1995;57:344–358.

6. Lakes R. Materials with structural hierarchy. Nature 1993;361:511–515.

7. Weiner S and Wagner HD. The material bone: structure-mechanical function relations. Annual Review of Materials Science 1998;28:271–298.

8. Müller R. Hierarchical microimaging of bone structure and function. Nature Reviews Rheumatology 2009;5:373–381.

9. Landis WJ, Song MJ, Leith A, McEwen L, and McEwen BF. Mineral and organic matrix interaction in normally calcifying tendon visualized in three dimensions by high-voltage electron microscopic tomography and graphic image reconstruction. Journal of Structural Biology 1993;110:39–54.

10. Hodge AJ and Petruska JA. Recent studies with the electron microscope on ordered aggregates of the tropocollagen molecule. Aspects of Protein Structure 1963:289–300.

11. Boskey AL. Mineral-matrix interactions in bone and cartilage. Clinical Orthopaedics and Related Research 1992:244.

12. Weiner S and Traub W. Organization of hydroxyapatite crystals within collagen fibrils. FEBS letters 1986;206:262–266.

13. Donnelly E, Williams RM, Downs SA, Dickinson ME, Baker SP, and Meulen MCH van der. Quasistatic and dynamic nanomechanical properties of cancellous bone tissue relate to collagen content and organization. Journal of Materials Research 2006;21:2106–2117.

14. Ambekar R, Chittenden M, Jasiuk I, and Toussaint KC. Quantitative second-harmonic generation microscopy for imaging porcine cortical bone: comparison to SEM and its potential to investigate age-related changes. Bone 2011.

15. Burket JC, Brooks DJ, MacLeay JM, Baker SP, Boskey AL, and Meulen MCH van der. Variations in nanomechanical properties and tissue composition within trabeculae from an ovine model of osteoporosis and treatment. Bone 2012.

16. Jepsen KJ, Schaffler MB, Kuhn JL, Goulet RW, Bonadio J, and Goldstein SA. Type I collagen mutation alters the strength and fatigue behavior of Mov13 cortical tissue. Journal of Biomechanics 1997;30:1141–1147.

17. Wallace JM, Rajachar RM, Allen MR, Bloomfield SA, Robey PG, Young MF, and Kohn DH. Exercise-induced changes in the cortical bone of growing mice are bone-and gender-specific. Bone 2007;40:1120–1127.

18. Lenthe GH van, Voide R, Boyd SK, and Müller R. Tissue modulus calculated from beam theory is biased by bone size and geometry: implications for the use of three-point bending tests to determine bone tissue modulus. Bone 2008;43:717–723.

19. Donnelly E, Baker SP, Boskey AL, and Meulen MCH van der. Effects of surface roughness and maximum load on the mechanical properties of cancellous bone measured by nanoindentation. Journal of Biomedical Materials Research Part A 2006;77:426–435.

20. Silva MJ, Brodt MD, Fan Z, and Rho JY. Nanoindentation and whole-bone bending estimates of material properties in bones from the senescence accelerated mouse SAMP6. Journal of Biomechanics 2004;37:1639–1646.

21. Rho JY and Pharr GM. Effects of drying on the mechanical properties of bovine femur measured by nanoindentation. Journal of Materials Science: Materials in Medicine 1999;10:485–488.

22. Hengsberger S, Kulik A, and Zysset PH. Nanoindentation discriminates the elastic properties of individual human bone lamellae under dry and physiological conditions. Bone 2002;30:178–184.

23. Bushby AJ, Ferguson VL, and Boyde A. Nanoindentation of bone: Comparison of specimens tested in liquid and embedded in polymethylmethacrylate. Journal of Materials Research 2004;19:249–259.

24. Currey JD. The effect of porosity and mineral content on the Young's modulus of elasticity of compact bone. Journal of Biomechanics 1988;21:131 – 139.

25. Schaffler MB and Burr DB. Stiffness of compact bone: Effects of porosity and density. Journal of Biomechanics 1988;21:13 –16.

26. Martin RB and Boardman DL. The effects of collagen fiber orientation, porosity, density, and mineralization on bovine cortical bone bending properties. Journal of Biomechanics 1993;26:1047–1054.

27. Hernandez CJ, Beaupré GS, Keller TS, and Carter DR. The influence of bone volume fraction and ash fraction on bone strength and modulus. Bone 2001;29:74–78.

28. Burstein AH, Zika JM, Heiple KG, and Klein L. Contribution of collagen and mineral to the elastic-plastic properties of bone. The Journal of Bone and Joint Surgery 1975;57:956.

29. Burr DB. The contribution of the organic matrix to bones material properties. Bone 2002;31:8–11.

30. Wang X, Bank RA, TeKoppele JM, Hubbard GB, Althanasiou KA, and Agrawal C. Effect of collagen denaturation on the toughness of bone. Clinical Orthopaedics and Related Research 2000;371:228.

31. Saber-Samandari S and Gross KA. Micromechanical properties of single crystal hydroxyapatite by nanoindentation. Acta Biomaterialia 2009;5:2206–2212.

32. Christiansen DL, Huang EK, and Silver FH. Assembly of type I collagen: fusion of fibril subunits and the influence of fibril diameter on mechanical properties. Matrix Biology 2000;19:409 –420.

33. Wang X, Bank RA, Tekoppele JM, and Agrawal C. The role of collagen in determining bone mechanical properties. Journal of Orthopaedic Research 2006;19:1021–1026.

34. Fratzl P, Gupta HS, Paschalis EP, and Roschger P. Structure and mechanical quality of the collagen–mineral nano-composite in bone. Journal of Materials Chemistry 2004;14:2115–2123.

35. Vashishth D, Gibson GJ, Khoury JI, Schaffler MB, Kimura J, and Fyhrie DP. Influence of nonenzymatic glycation on biomechanical properties of cortical bone. Bone 2001;28:195–201.

36. Oxlund H, Barckman M, Ørtoft G, and Andreassen TT. Reduced concentrations of collagen cross-links are associated with reduced strength of bone. Bone 1995;17:S365–S371.

37. Paschalis EP, Tatakis DN, Robins S, et al. Lathyrism-induced alterations in collagen cross-links influence the mechanical properties of bone material without affecting the mineral. Bone 2011;49:1232 –1241.

38. Zioupos P, Gresle M, and Winwood K. Fatigue strength of human cortical bone: age, physical, and material heterogeneity effects. Journal of Biomedical Materials Research Part A 2008;86:627–636.

39. Nalla RK, Stalken JS, Kinney JH, and Ritchie RO. Fracture in human cortical bone: local fracture criteria and toughening mechanisms. Journal of Biomechanics 2005;38:1517 –1525.

40. Bouxsein ML, Boyd SK, Christiansen BA, Guldberg RE, Jepsen KJ, and Müller R. Guidelines for assessment of bone microstructure in rodents using micro–computed tomography. Journal of Bone and Mineral Research 2010;25:1468–1486.

41. Freeman JJ, Wopenka B, Silva MJ, and Pasteris JD. Raman spectroscopic detection of changes in bioapatite in mouse femora as a function of age

and in vitro fluoride treatment. Calcified Tissue International 2001;68:156–162.

42. Carden A and Morris MD. Application of vibrational spectroscopy to the study of mineralized tissues (review). Journal of Biomedical Optics 2000;5:259–268.

43. Turunen MJ, Saarakkala S, Rieppo L, Helminen HJ, Jurvelin JS, and Isaksson H. Comparison between infrared and Raman spectroscopic analysis of maturing rabbit cortical bone. Applied Spectroscopy 2011;65:595–603.

44. Oliver WC and Pharr GM. Improved technique for determining hardness and elastic modulus using load and displacement sensing indentation experiments. Journal of Materials Research 1992;7:1564–1583.

45. Rho JY, Tsui TY, and Pharr GM. Elastic properties of human cortical and trabecular lamellar bone measured by nanoindentation. Biomaterials 1997;18:1325–1330.

46. Rho JY, Zioupos P, Currey JD, and Pharr GM. Variations in the individual thick lamellar properties within osteons by nanoindentation. Bone 1999;25:295–300.

47. Burket J, Gourion-Arsiquaud S, Havill LM, Baker SP, Boskey AL, and Meulen MCH Van der. Microstructure and nanomechanical properties in osteons relate to tissue and animal age. Journal of Biomechanics 2011;44:277–284.

48. R. DT and B. AH. The elastic and ultimate properties of compact bone tissue. Journal of Biomechanics 1975;8:393 –405.

49. Zysset PK, Edward Guo X, Edward Hoffler C, Moore KE, and Goldstein SA. Elastic modulus and hardness of cortical and trabecular bone lamellae measured by nanoindentation in the human femur. Journal of Biomechanics 1999;32:1005–1012.

50. Rho JY, Roy ME, Tsui TY, and Pharr GM. Elastic properties of microstructural components of human bone tissue as measured by nanoindentation. Journal of Biomedical Materials Research 1999;45:48–54.

51. Rho JY, Zioupos P, Currey JD, and Pharr GM. Microstructural elasticity and regional heterogeneity in human femoral bone of various ages examined by nano-indentation. Journal of Biomechanics 2002;35:189–198.

52. Goodwin KJ and Sharkey NA. Material properties of interstitial lamellae reflect local strain environments. Journal of Orthopaedic Research 2002;20:600–606.

53. Hoffler CE, Guo XE, Zysset PK, and Goldstein SA. An application of nanoindentation technique to measure bone tissue lamellae properties. Journal of Biomechanical Engineering 2005;127:1046.

54. Gupta HS, Stachewicz U, Wagermaier W, Roschger P, Wagner HD, and Fratzl P. Mechanical modulation at the lamellar level in osteonal bone. Journal of Materials Research 2006;21:1913–1921.

55. Miller LM, Little W, Schirmer A, Sheik F, Busa B, and Judex S. Accretion of bone quantity and quality in the developing mouse skeleton. Journal of Bone and Mineral Research 2007;22:1037–1045.

56. Busa B, Miller L, Rubin C, Qin YX, and Judex S. Rapid establishment of chemical and mechanical properties during lamellar bone formation. Calcified Tissue International 2005;77:386–394.

57. Donnelly E, Boskey AL, Baker SP, and Meulen MCH Van der. Effects of tissue age on bone tissue material composition and nanomechanical properties in the rat cortex. Journal of Biomedical Materials Research Part A 2010;92:1048–1056.

58. McCalden RW and McGeough JA. Age-Related Changes in the Compressive Strength of Cancellous Bone. The Relative Importance of Changes in Density and Trabecular Architecture and Court–Brown, C. M. The Journal of Bone & Joint Surgery 1997;79:421–7.

59. Rice JC, Cowin SC, and Bowman JA. On the dependence of the elasticity and strength of cancellous bone on apparent density. Journal of Biomechanics 1988;21:155–168.

60. Bailey AJ, Sims TJ, Ebbesen EN, Mansell JP, Thomsen JS, and Mosekilde L. Age-related changes in the biochemical properties of human cancellous bone collagen: relationship to bone strength. Calcified Tissue International 1999;65:203–210.

61. Mosekilde L, Mosekilde L, and Danielsen CC. Biomechanical competence of vertebral trabecular bone in relation to ash density and age in normal individuals. Bone 1987;8:79–85.

62. Zioupos P and Currey JD. Changes in the stiffness, strength, and toughness of human cortical bone with age. Bone 1998;22:57–66.

63. Zioupos P, Currey JD, and Hamer AJ. The role of collagen in the declining mechanical properties of aging human cortical bone. Journal of Biomedical Materials Research 1999;45:108–116.

64. Wall JC, Chatterji SK, and Jeffery JW. Age-related changes in the density and tensile strength of human femoral cortical bone. Calcified Tissue International 1979;27:105–108.

65. Gourion-Arsiquaud S, Faibish D, Myers E, Spevak L, Compston J, Hodsman A, Shane E, Recker RR, Boskey ER, and Boskey AL. Use of FTIR spectroscopic imaging to identify parameters associated with fragility fracture. Journal of Bone and Mineral Research 2009;24:1565–1571.

66. Gourion-Arsiquaud S, Lukashova L, Power J, Loveridge N, Reeve J, and Boskey AL. Fourier transformed infra-red imaging of femoral neck bone: Reduced heterogeneity of mineral-to-matrix and carbonate-to-phosphate and more variable crystallinity in treatment-naïve fracture cases compared to fracture-free controls. Journal of Bone and Mineral Research 2012.

67. Boivin GY, Chavassieux PM, Santora AC, Yates J, and Meunier PJ. Alendronate increases bone strength by increasing the mean degree of mineralization of bone tissue in osteoporotic women. Bone 2000;27:687–694.

68. Boskey AL, DiCarlo E, Paschalis E, West P, and Mendelsohn R. Comparison of mineral quality and quantity in iliac crest biopsies from high-and low-turnover osteoporosis: an FT-IR microspectroscopic investigation. Osteoporosis International 2005;16:2031–2038.

69. McCreadie BR, Morris MD, Chen T, Sudhaker Rao D, Finney WF, Widjaja E, and Goldstein SA. Bone tissue compositional differences in women with and without osteoporotic fracture. Bone 2006;39:1190–1195.

70. Fratzl-Zelman N, Roschger P, Gourrier A, Weber M, Misof BM, Loveridge N, Reeve J, Klaushofer K, and Fratzl P. Combination of nanoindentation and quantitative backscattered electron imaging revealed altered bone ma-

terial properties associated with femoral neck fragility. Calcified Tissue International 2009;85:335–343.

71. Wang X, Sudhaker Rao D, Ajdelsztajn L, Ciarelli TE, Lavernia EJ, and Fyhrie DP. Human iliac crest cancellous bone elastic modulus and hardness differ with bone formation rate per bone surface but not by existence of prevalent vertebral fracture. Journal of Biomedical Materials Research Part B: Applied Biomaterials 2008;85:68–77.

72. Davis JW, Ross PD, and Wasnich RD. Evidence for both generalized and regional low bone mass among elderly women. Journal of Bone and Mineral Research 1994;9:305–309.

73. Burchardt H. The biology of bone graft repair. Clinical Orthopaedics and Related Research 1983:28.

74. Sun L, Fan Y, Li D, Zhao F, Xie T, Yang X, and Gu Z. Evaluation of the mechanical properties of rat bone under simulated microgravity using nanoindentation. Acta Biomaterialia 2009;5:3506–3511.

75. Camacho NP, Hou L, Toledano TR, Ilg WA, Brayton CF, Raggio CL, Root L, and Boskey AL. The material basis for reduced mechanical properties in oim mice bones. Journal of Bone and Mineral Research 1999;14:264–272.

76. Silva MJ, Brodt MD, and Ettner SL. Long Bones From the Senescence Accelerated Mouse SAMP6 Have Increased Size But Reduced Whole-bone Strength and Resistance to Fracture. Journal of Bone and Mineral Research 2002;17:1597–1603.

77. Nakamura T, Kurokawa T, and Orimo H. Increased mechanical strength of the vitamin D-replete rat femur by the treatment with a large dose of 24R, 25 (OH) 2D3. Bone 1989;10:117–123.

78. Kim G, Boskey AL, Baker SP, and Meulen MCH van der. Improved prediction of rat cortical bone mechanical behavior using composite beam theory to integrate tissue level properties. Journal of Biomechanics 2012.

79. Donnelly E, Chen DX, Boskey AL, Baker SP, and Meulen MCH van der. Contribution of mineral to bone structural behavior and tissue mechanical properties. Calcified Tissue International 2010:1–11.

CHAPTER 2

IMPROVED PREDICTION OF RAT CORTICAL BONE MECHANICAL BEHAVIOR USING COMPOSITE BEAM THEORY TO INTEGRATE TISSUE-LEVEL PROPERTIES

[1]

2.1 Introduction

Whole bone mineralization and quantity predict whole bone mechanical behavior for healthy bone [1–3]; however, skeletal pathologies such as osteoporosis alter those relationships. Dual energy x-ray absorptiometry (DXA) is currently the clinical standard for assessing osteoporotic fracture risk but is not a perfect predictor of fracture [4]. Fracture risk evaluation can be improved by considering age and previous fracture status as evidenced by FRAX [5–7]. Areal bone mineral density (aBMD) assessed by DXA reflects both bone volume and density. Osteoporosis therapies disproportionately alter aBMD and fracture risk. Fluoride treatments were ineffective at reducing fracture risk despite 8-16% increases in aBMD [8, 9], whereas antiresorptive treatments reduced fracture risk by 30-50% despite only increasing aBMD by 8-10% [10, 11].

The disconnect between BMD and whole bone mechanical performance in diseased bone has prompted research aimed at revealing the role of tissue-level composition. Like other load bearing structures, whole bone mechanical be-

[1]Reprinted from Journal of Biomechanics, Vol. 45, Kim, Grace, Adele L. Boskey, Shefford P. Baker, and Marjolein CH van der Meulen, Improved prediction of rat cortical bone mechanical behavior using composite beam theory to integrate tissue level properties, pp. 27842790 (2012).

havior depends on geometry, volume, and tissue-level properties. The application of nanoindentation and vibrational spectroscopy techniques such as Raman and Fourier transform infra-red spectroscopy to bone allow the investigation of mechanical properties and composition of individual microstructural features while avoiding pores and cellular lacunae visible on the surface. Concurrent investigations of tissue material properties from nanoindentation and tissue-level composition with whole bone mechanical behavior revealed inconsistent relationships between micro- and macroscale properties [12–15]. Both the presence and absence of correlations have been reported between whole bone and tissue-level mechanical properties, indicating that the extrapolation of tissue-level properties to whole bone mechanical behavior is not straightforward. The aforementioned studies averaged tissue-level data points into a single value to represent the material properties of the entire bone to correlate with whole bone mechanical behavior. Averaging highly resolved tissue-level properties simplifies bone into a homogeneous material and diminishes the advantage of the local tissue-level measurements provided by nanoindentation and vibrational microspectroscopy. To take into account mineralization heterogeneity, studies have used composite beam theory to generate density-weighted moments of inertia or bending stiffnesses that take spatial variations in mineralization into account [16–18]. These models used apparent level relationships between Youngs modulus and mineralization, and the use of tissue-level relationships may improve the predictive capability of these models.

The current study used tissue-level relationships between mineralization and material properties to calculate density-weighted section moduli to predict whole bone mechanical behavior. This method preserves the spatial distribution and heterogeneity of tissue properties while using intrinsic tissue-level relation-

ships instead of apparent level relationships to calculate density-weighted section moduli. Relationships between mineralization and mechanical properties at the whole bone and tissue-level length scales were characterized in rats with impaired mineralization and reduced whole bone mechanical behavior through vitamin D deficiency. Whole bone composition and geometry were quantified using micro-computed tomography (microCT) prior to whole bone mechanical testing in three point bending. Contralateral limbs were used for tissue-level analyses. Tissue-level mechanical properties were measured using nanoindentation and tissue composition was measured using Raman microspectroscopy. Density-weighted section moduli calculated from tissue-level measurements were compared with section moduli calculated using one previously reported apparent level relationship, averaged tissue-level properties, and whole bone measures of composition and geometry on their ability to predict whole bone mechanical properties.

2.2 Methods

Bone mineralization was reduced using a previously established vitamin D deficiency treatment in growing rats [19]. Three week old male Sprague-Dawley rats (Charles River, Wilmington, MA) were divided into three groups: Control, and two reduced mineralization groups, NC1 and NC3 (n = 20/group) and given their respective diets and water ad libitum for the 10 wk experimental duration. Intraperitoneal injections of tetracycline and demeclocycline were administered 28 d and 14 d before euthanasia. These fluorochrome labels demarcated 3 tissue age zones, 0-14 d, 15-28 d, and 29 d+. After 10 wk, animals were euthanized by CO_2 asphyxiation. Vitamin D deficiency was confirmed by an

enzyme-linked immunoassay for 1,25-OH D (Immunodiagnostic Systems Inc, Scottsdale, AZ) (Control n = 12, NC1 n = 11, NC3 n = 16). All procedures were approved by Cornell Universitys Institutional Animal Care and Use Committee (IACUC).

All animals started their respective diets at weaning, 3 weeks after birth. Controls were fed normal rat chow replete in vitamin D_3 (2000 IU/kg) and 0.47% Ca for the 10 wk experimental duration (Harlan Teklad, TD. 08364, Indianapolis, IN). To generate a range of altered mineralization, NC1 was fed 0IU/kg Ca and 0IU/kg D_3 chow during week 8, and chow with 0.47% Ca and 0IU/kg vitamin D_3 all other weeks and NC3 was fed 0IU/kg Ca and 0IU/kg D_3 chow during weeks 7, 8 and 9, and chow with 0.47% Ca and 0IU/kg vitamin D_3 all other weeks. Animals were housed in 12 h/12 h light-dark cycles with UV radiation free lights during the 10 wk experimental duration. Intraperitoneal injections of tetracycline (15 mg/kg) were administered 28 d before euthanasia, and demeclocycline (20 mg/kg) 14 d before euthanasia. Blood was collected by cardiac puncture immediately after euthanasia to confirm vitamin D deficiency by an enzyme-linked immunoassay for 1,25-OH D (Immunodiagnostic Systems Inc, Scottsdale, AZ).

2.2.1 Whole Bone Testing

Left femurs (n = 20/group) were collected for whole bone compositional and geometric measures and mechanical testing. Femurs were scanned in saline using microCT with 25 μm isotropic voxel size (eXplore CT 120, GE Healthcare, Waukesha, WI). Femurs were cleaned of soft tissue and stored in saline soaked

gauze at −20°C prior to use. Femurs were thawed and scanned in saline using microCT with 25 μm isotropic voxel size. All bones were scanned at 80 kV, 32 mA, 100 msec exposure with 1 image every 0.5° for 360°. Mineral density was calibrated according to the manufacturer using a calibration phantom with SB3 which has a mineral density of 1073 mg/cc. A global threshold equivalent to 43 mgHA/cc was used for all microCT scans to include newly formed and less mineralized bone. A global threshold equivalent to 43 mgHA/cc was used [20]. Tissue mineral density (TMD) and content (TMC) were calculated for a 3 mm thick volume of interest (VOI) from the midshaft of the femurs (MicroView 2.2, GE Healthcare, Waukesha, WI). The VOI consisted of 120 slices. The cortical cross-sectional areas (A_c) was calculated for each slice then averaged, resulting in a single value for each sample (in-house MATLAB code, The Mathworks Inc, Natick, NA).

After scanning, femurs were failed in three point bending in the anterior-posterior direction (858 Mini Bionix, MTS, Eden Prairie, MN). Outcomes from the load-displacement data included the failure moment (M_F), bending stiffness (EI), effective modulus (EI/I_{un}), and post-yield displacement (D_{py}). A constant load rate of 0.05 mm/sec, a span width (w) of 18 mm, and no preload was applied for all samples. Load and crosshead displacement were sampled at 10Hz during testing. The bending stiffness (EI) was calculated as $kw^3/48$, where k is the slope of the linear portion of the load displacement curve. The effective modulus was calculated as EI/I_{un}, whereI_{un} was the unweighted geometric moment of inertia calculated from microCT scans. The failure moment (M_F) was calculated as $P_F w/4$ where P_F was the failure load. The post-yield displacement (D_{py}) was calculated as the differences between the yield and failure displacements.

2.2.2 tissue-level Measurements

A subset of the right femurs was processed for tissue-level analyses (n = 4-5/group, 14 total). Femurs were dehydrated in ethanol and embedded in polymethymethacrylate. A 3 mm thick transverse section of cortical bone from the midshaft of each sample was fixed to an atomic force microscope stub and polished anhydrously [21]. For each sample, 5 indentations spaced at least 7 μm apart were made in the middle of the zones parallel to the labels and at the periosteal edge (Triboindenter, Hysitron, Minneapolis, MN). Four different tissue age zones were tested: periosteal zone, 0-14 d, 15-28 d, and 29 d+. Indents were created using a 500 μN trapezoidal load function. The indentation modulus (E_i) and hardness (H) were calculated from the unloading portion of the 500 μN load-displacement curve [22]. Digital white light and fluorescence images of the sample surfaces were taken using an optical microscope and overlaid so fiduciary markers could be used to identify tissue age zones based on the fluorochrome labels. Samples were tested dry. Indentations were made using a scanning nanoindenter with a Berkovich tip. A 20 x 20 μm scan was performed prior to indentation to ensure indents were not placed on pores or lacunae on the surface. Indentations were localized to the anterior-medial quadrant of the femur since this quadrant had the best separation of fluorochrome labels. Indents were created using a trapezoidal load function with a peak load of 500 μN, load/unload rate of ± 50 μN/s and 10 s hold times. After the 500 μN indent, a 1000 μN indent was placed at the same location, creating fiduciary markers visible using the optical microscope used for Raman microspectroscopy.

Residual indents were indentified using the white light optical microscope attached to the Raman microscope. The laser spot (2 μm diameter) was cen-

tered over each residual indent and corresponding Raman spectra between 800 and 1800 cm^{-1} were collected (inVia, Renishaw, Gloucestershire, UK). Tissue mineralization (mineral:matrix) and B-type carbonate substitution (carbonate:phosphate) were calculated [23, 24]. Raman spectra between 800 and 1800 cm^{-1} were collected by averaging 3 accumulations, each with 10 s exposures and cosmic ray removal (inVia, Renishaw, Gloucestershire, UK). The Raman microscope was equipped with a 785 nm laser and a 50X, 0.75 NA objective resulting in a 2 μm diameter spot size. Background subtraction and smoothing (WiRE V2.0, Renishaw; in-house MATLAB code) were performed before peak analyses. Tissue mineralization was calculated as the peak height ratio of the phosphate $\nu 1$ (965 cm^{-1}) and CH_2 wag (1450 cm^{-1}) peaks. B-type carbonate substitution was calculated from the peak height ratio of carbonate $\nu 1$ (1070 cm^{-1}) and phosphate $\nu 1$ peaks.

2.2.3 Composite Beam Model

To predict whole bone mechanical behavior, composite beam theory was used to calculate density-weighted moments of inertia in addition to the commonly used geometric (unweighted) moment of inertia [25]. Similar to the cortical area measurements, the moment of inertia was calculated for each slice then averaged, resulting in a single value for each sample. An unweighted moment of inertia about the medial-lateral axis (I_{ML}) with respect to the centroid (X) was calculated (in-house MATLAB code) assuming a homogeneous bone tissue:

$$X = \frac{\sum_{j=1}^{n} x_j A_j}{\sum_{j=1}^{n} A_j} \tag{2.1}$$

$$I_{ML} = \sum_{j=1}^{n} A_j x_j^2 - X^2 \sum_{j=1}^{n} A_j \tag{2.2}$$

where the summation is over the total pixel count (n). For each pixel containing bone, x_j is the distance from the center of the j-th pixel to the y-axis and A_j is the area of the j-th pixel. Three density-weighted moments ($I_{lin,a}$, $I_{lin,b}$, $I_{lin,exp}$) of inertia were calculated (in-house MATLAB code) with respect to the mass-weighted centroid (X_w):

$$X_w = \frac{\sum_{j=1}^{n} x_j v_j A_j}{\sum_{j=1}^{n} v_j A_j} \tag{2.3}$$

$$I_{weighted} = \sum_{j=1}^{n} v_j A_j x_j^2 - X_w^2 \sum_{j=1}^{n} v_j A j \tag{2.4}$$

where v was the attenuation weighted value calculated for each pixel assuming the modulus was proportional to the attenuation value, either linearly according to our tissue-level data from the anterior-medial quadrant (Equation 2.5) or exponentially according to an apparent level relationship (Equation 2.6).

$$v_j = m\frac{HU_j}{TH} + b \tag{2.5}$$

$$v_j = (\frac{HU_j}{TH})^a \tag{2.6}$$

HU_j is the x-ray attenuation of the j-th pixel and TH is the global threshold value both in Hounsfield units, m is the slope, b is the intercept, and a is the exponential coefficient.

Two linear equations based on the tissue-level data from this study were used to calculate density-weighted moments of inertia. The equation of the best fit linear regression between indentation modulus and mineral:matrix ratio was $y = 2.4x + 11$ (Figure 2.3a) consequently $m = 2.4$ and $b = 11$ in Equation (2.5). Substituting Equation (2.5) into Equations (2.3) and (2.4) resulted in a lin-

early weighted centroid and moment of inertia ($I_{lin,a}$). The best fit linear regression overestimated the modulus of mineral:matrix ratios below 2. The intercept of the regression line represents the indentation modulus of tissue containing no mineral. Demineralized collagen fibrils have been shown to have a Youngs modulus of 20 MPa, which is less than 1% of the best fit intercept, 11 GPa [26]. To better represent the modulus of unmineralized tissue, a second linear regression with the intercept fixed at 0 was used to calculate another density-weighted moment of inertia. The equation of this line was $y = 4x$, with $m = 4$ and $b = 0$. Substituting Equation (2.5) into Equations (2.3) and (2.4) resulted in a second linearly weighted centroid and moment of inertia ($I_{lin,b}$). Respective section moduli ($Z_{lin,a}$,$Z_{lin,b}$) using the moments of inertia were calculated by dividing the respective moments of inertia by the maximum anterior-posterior distances from the density-weighted centroids.

The exponential relationship we used was based a previously established relationship between ash fraction and Youngs modulus from bovine cortical bone beams where $a = 3.91$ in Equation (2.6) [27] . Substitution of Equation (2.6) into Equations (2.3) and (2.4) resulted in an exponentially-weighted centroid and moment of inertia (I_{exp}). The section modulus (Z_{exp}) was calculated by dividing the moment of inertia (I_{exp}) by the maximum anterior-posterior distance from the density-weighted centroid. The sensitivity of our results to the exponential coefficient chosen was investigated by looking at a range of exponential coefficients.

2.2.4 Statistical Analyses

For all statistical tests, p-values less than 0.05 were considered significant. Results presented are significant unless stated otherwise. A one-way analysis of variance with Tukey-Kramer post-hoc was used to indentify differences in whole bone outcome measures between all groups (JMP 8.0, SAS Institute). Linear regressions determined the correlations between both whole bone composition and mechanical behavior, and whole bone geometric measures and mechanical behavior. Significant differences between correlation coefficients (r) for the corresponding coefficients of determination (r^2) from linear regressions were identfied using Z tests with a Fisher r to Z transformation. For tissue-level outcomes, a two-way ANOVA was performed with tissue age zone and treatment group as main effects to determine differences in E_i, H, mineral:matrix ratio, and carbonate:phosphate ratio. An analysis of covariance on E_i with diet group as the factor and tissue-level compositional measures as the covariates was performed.

2.3 Results

2.3.1 Whole Bone Properties

Serum levels of 1,25-OH D were reduced in both vitamin D deficient groups compared with Controls (36.9 ± 2.17 nmol/L), 60% and 64%, respectively. Serum levels of 1,25-OH D in the NC1 and NC3 groups were not different from each other. Final body masses were reduced by 18% and 19% compared with

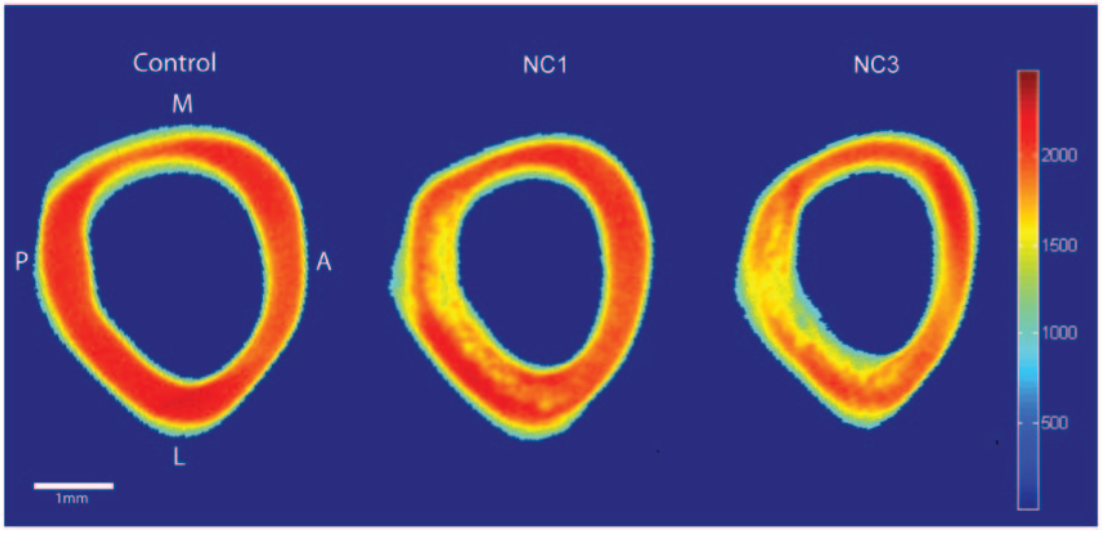

Figure 2.1: Representative microCT images of Control, NC1, and NC3 right femur cross sections. Colors represent differences in attenuation (Houndsfield Units). Vitamin D deficiency reduced mineralization of the cortical bone particularly in the posterior half of the femurs.

Controls in the NC1 and NC3 groups, respectively.

From the whole bone analyses, vitamin D deficiency reduced whole bone mechanical performance, and mineralization and geometric parameters as measured by microCT compared with Controls (Table 2.1, Figure 2.1). TMC was reduced by 20% and 27% in NC1 and NC3 compared with Controls, respectively. TMD was reduced by 8% and 12% in NC1 and NC3 compared with Controls. TMC was 8.6% lower and TMD was 4.2% lower in the NC3 group compared with NC1. Cortical area was reduced by 13% and 17% in NC1 and NC3 compared with Controls. Failure moment was reduced by 26% and 33% in NC1 and NC3 compared with Controls. The bending stiffness was reduced by 32% and 38% in NC1 and NC3 compared with Controls. The effective modulus was 20% lower in the NC3 group compared with Controls. The post-yield

displacement was not different with vitamin D deficiency. No differences were observed between NC1 and NC3 treatments in geometric measures or whole bone mechanical behavior.

Table 2.1: Mean measures of whole bone composition, geometry and mechanical behavior. Values shown as mean (standard deviation). *Significantly different from Control; + significantly different from NC1 treatment group.

	Control	NC1		NC3	
			Difference vs. Control (%)		Difference vs. Control (%)
Final Body Mass (g)	506 (39)	416 (39)	-18*	408 (39)	-19*
Tissue Mineral Content (mg)	23.2 (1.6)	18.6 (2.2)*	-20*	17.0 (1.5)+	-27*+
Tissue Mineral Density (mg/cc)	937 (23)	864 (37)*	-8*	825 (41)+	-12*+
Cortical Area (mm^2)	8.4 (0.5)	7.3 (0.7)*	-13*	7.0 (0.6)*	-17*
Moment of Inertia (mm^4)	17.5 (2.7)	14.3 (2.6)*	-18*	13.6 (2.8)*	-22*
Moment of Inertia Lin. A (mm^4)	165 (33)	127 (29)*	-23*	120 (26)*	-27*
Moment of Inertia Lin. B (mm^4)	90.1 (13.8)	68.0 (13.0)*	-25*	61.7 (12.0)*	-32*
Moment of Inertia Exp. (mm^4)	449 (78)	273 (68)*	-39*	218 (49)*+	-52*+
Section Modulus (mm^3)	5.3 (0.8)	4.4 (0.7)*	-17*	4.2 (0.7)*	-20*
Section Modulus Lin. A (mm^3)	85.4 (12)	69.6 (11)*	-19*	66.0 (10)*	-23*
Section Modulus Lin. B (mm^3)	26.9 (3.9)	20.9 (3.7)*	-22*	19.3 (3.0)*	-28*
Section Modulus Exp. (mm^3)	131 (23)	81.5 (21)*	-38*	68.5 (14)*+	-48*+
Failure Moment (Nmm)	695 (94)	517 (72)*	-26*	469 (73)*	-33*
Bending Stiffness (Nmm^2)	18100 (3600)	12400 (2800)*	-32*	11200 (2400)*	-38*
Post Yield Displacement (mm)	0.12 (0.15)	0.13 (0.14)	+8	0.14 (0.16)	+17
Effective Modulus (N/mm^2)	1870 (570)	1560 (360)	-17	1500 (430)	-20*

2.3.2 tissue-level Properties

From the two-way ANOVA with diet group and tissue age zone, the indentation modulus in all groups was lower at the periosteal surface compared to the 0-29 d+ tissue zones. Additionally, in the NC1 group, the indentation modulus of 0-14 d tissue was 49% lower than the 14-29 d+ tissue (Figure 2.2a). Hardness results followed similar trends to the indentation modulus (Figure 2.2b). For all groups, the hardness was lower at the periosteal surface compared to the 0-29 d+ tissue zones. The NC1 group had a 45% lower hardness in the 0-14 d tissue than 14-29 d+ tissue. The mineral:matrix ratio increased with increasing tissue age for all diet groups (Figure 2.2c). Vitamin D deficiency decreased the mineral:matrix ratio compared to Control animals in the intracortical tissue (0-14, 15-28 and 29 d+), but not at the periosteal edge. In the 0-14 d tissue the Control mineral:matrix ratio was higher than NC1 and NC3. In 15-28 d tissue the Control and NC1 mineral:matrix ratios were higher than NC3. In the 29 d+ tissue the Control mineral:matrix ratio was higher than both NC1 and NC3. Vitamin D deficiency delayed the increase in B-type carbonate substitution across the cortex (Figure 2.2d). Control animals had a significantly higher carbonate:phosphate ratio in the three older tissue age zones than at the periosteum. For NC1, the carbonate:phosphate ratio significantly increased after 15 d. The carbonate:phosphate ratio did not increase with tissue age for the NC3 group; intracortical tissue maintained similar levels to the youngest tissue.

From the analysis of covariance, diet group did not affect the relationship between mineral:matrix ratio and indentation modulus, thus indentation modulus and mineral:matrix ratio data from all groups were fit using a single linear model (r^2 = 0.54, p ¡ 0.001) (Figure 2.3a). The relationship between the indenta-

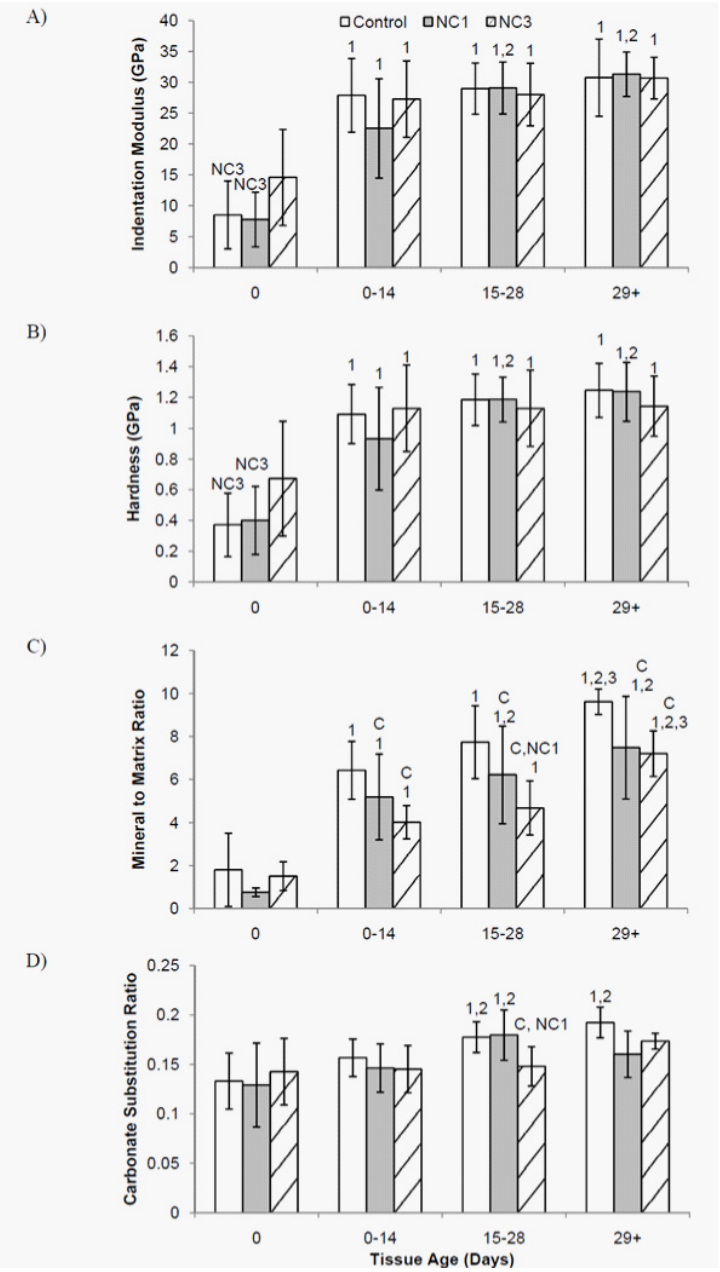

Figure 2.2: Mean A) indentation modulus, B) hardness, C) mineral:matrix ratio and D) carbonate substitution by diet group versus tissue age zone. Significantly different from Control (C), NC1 (NC1), NC3 (NC3) within a single tissue age zone. Significantly different from 0 day old tissue (1), 0-14 day old tissue (2), and 15-28 day old tissue (3) within the same group. Error bars indicate standard deviation.

tion modulus and carbonate substitution varied by diet group. Although tissue-level mechanical properties and the carbonate:phosphate ratio correlated in the Control and NC1 groups, no correlation existed in the NC3 group (Figure 2.3b).

2.3.3 Relating tissue-level and Whole Bone Properties

For the samples used for tissue-level analyses (n=14), linear regressions between whole bone mechanical behavior of the contralateral limbs and average intracortical tissue-level properties were examined (average of the oldest 3 tissue age zones). None of the averaged tissue-level properties were significant predictors for the effective modulus, bending stiffness, or failure moment.

Whole bone geometric and compositional measures from microCT were used to predict EI and M_F (Table 2.2). From the geometric and compositional data from microCT, the best predictor for EI was TMD (r^2 =0.56) and for M_F was TMC (r^2=0.78). M_F was better predicted than EI by every predictor. The linearly weighted moment of inertia ($I_{lin,a}$) increased the coefficient of determination for failure moment to r^2 = 0.57 compared with the geometric moment of inertia (r^2 = 0.36). $I_{lin,b}$ and $Z_{lin,b}$ increased coefficients of determination for whole bone mechanical behavior compared to the respective values calculated using the linear equation with the non zero intercept ($I_{lin,a}$,$Z_{lin,a}$). The exponentially weighted moment of inertia (I_{exp}) predicted 75% of the variability of the failure moment. The exponentially weighted section modulus (Z_{exp}) predicted 80% of the variability of the failure moment (Figure 2.4b). The exponentially weighted section modulus had significantly greater explanatory power for the failure mo-

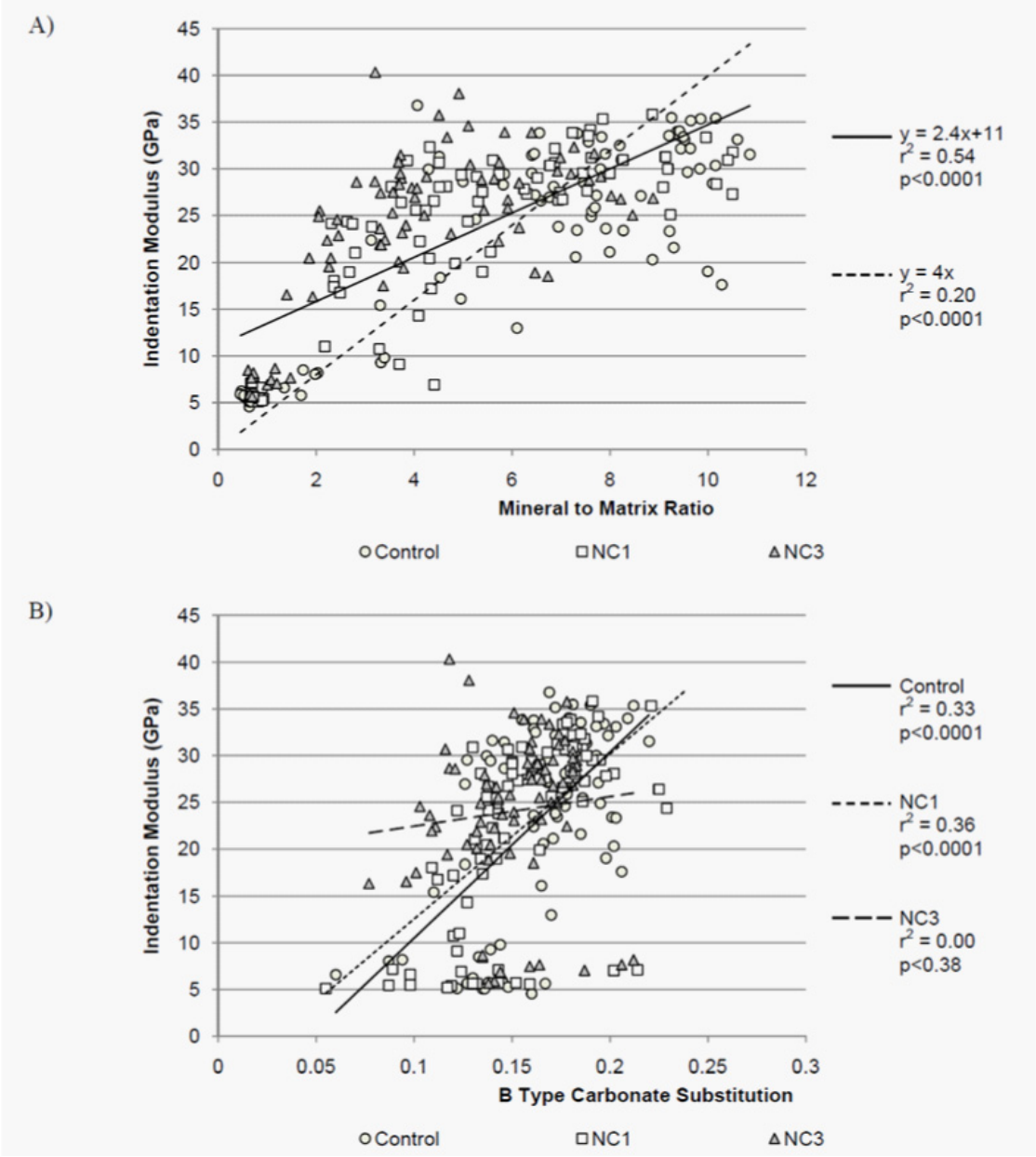

Figure 2.3: A) Linear regressions for mineral:matrix versus indentation modulus, solid line for y=2.4x+11 and a dashed line for y=4x. B) Analysis of covariance with B-type carbonate substitution as the covariate and diet group as the factor.

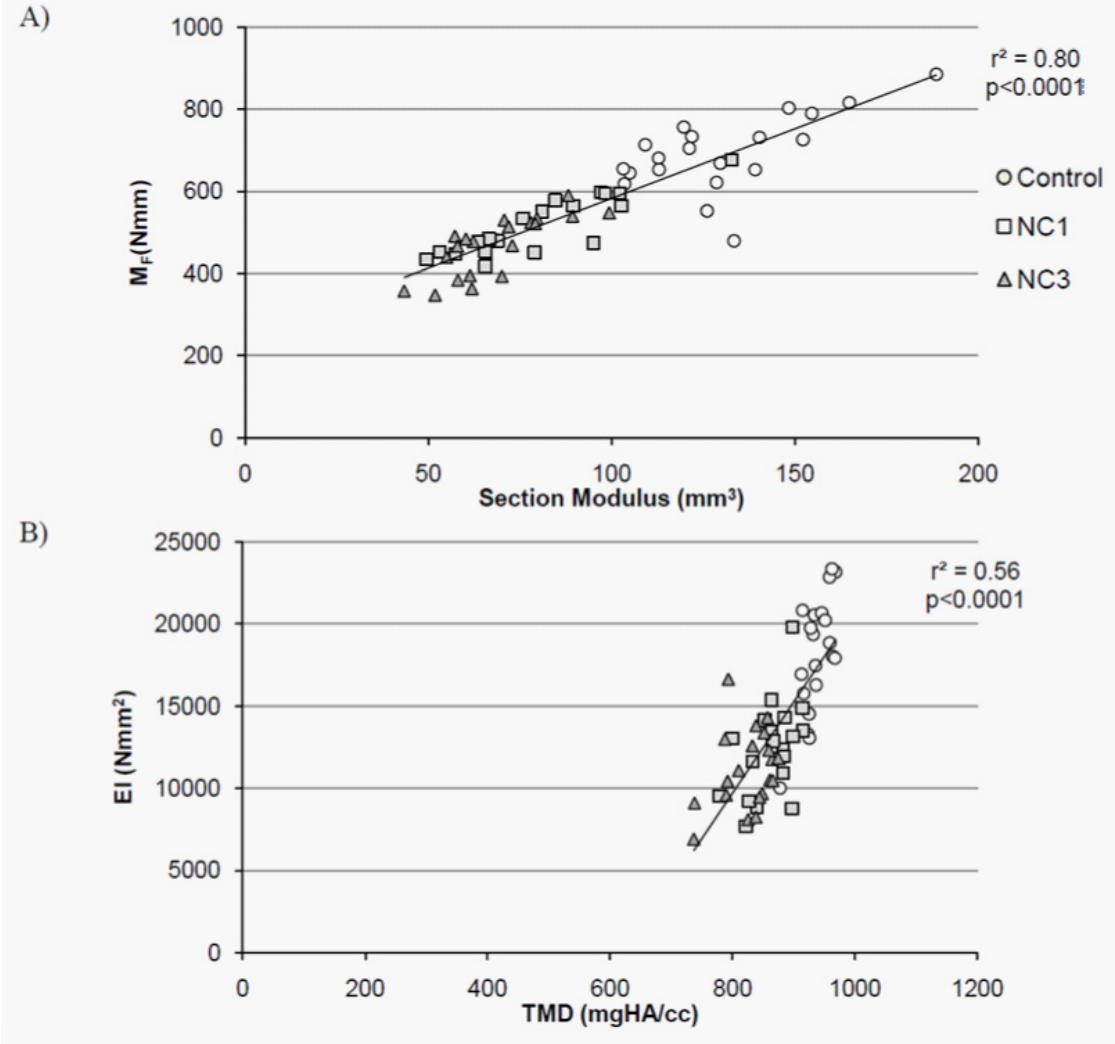

Figure 2.4: A) The best predictor for failure moment (MF) was the exponentially weighted section modulus. B) The best predictor for bending stiffness (EI) was tissue mineral density (TMD).

ment than all variables except TMC, exponentially weighted moment of inertia, and the linearly weighted section modulus with 0 intercept. For bending stiffness, the exponentially weighted section modulus had significantly greater explanatory power than all variables except TMC, TMD, and the exponentially weighted moment of inertia (Table 2.2).

Table 2.2: Coefficients of determination (r^2) for whole bone mechanical behavior, failure moment (M_F) and bending stiffness (EI). *Significantly different r^2 from the exponentially weighted section modulus for the failure moment. # Significantly different r^2 from the exponentially weighted section modulus for the bending stiffness.

		M_F	EI
Average material properties	Tissue mineral content	0.78	0.50
	Tissue mineral density	0.65*	0.56
Geometric properties	Cortical area	0.63*	0.32#
	Moment of inertia	0.36*	0.09#
	Section Modulus	0.47*	0.16#
Spatially varying material properties	Moment of inertia (linearly weighted, $I_{lin,a}$)	0.49*	0.15#
	Section modulus (linearly weighted, $Z_{lin,a}$)	0.54*	0.21#
	Moment of inertia (linearly weighted, $I_{lin,b}$)	0.57*	0.23#
	Section modulus (linearly weighted, $Z_{lin,b}$)	0.66	0.29#
	Moment of inertia (exponentially weighted, I_{exp})	0.75	0.43
	Section modulus (exponentially weighted, Z_{exp})	0.80	0.49

2.4 Discussion

Vitamin D deficiency in growing rats reduced measures of whole bone mechanical behavior, mineralization, and geometry similar to previous studies [12, 28, 29]. Reductions in whole bone mineralization, as indicated by reduced TMD, were paralleled by reductions in tissue-level mineral:matrix ratios with vitamin D deficiency. The spatial distribution and heterogeneity of tissue properties were preserved by using intrinsic tissue-level relationships instead of apparent level relationships to calculate density-weighted section moduli. Density-weighted section moduli calculated from tissue-level data better predicted variability in whole bone mechanical behavior than averaged tissue-level properties and unweighted measures of whole bone geometry; however, the density-weighted section moduli from apparent level data further improved the predictions.

To investigate the sensitivity of the results to the specific coefficients used in Equations (2.5) and (2.6), different intercepts and exponential coefficients were examined. For the linear equation, the predictive capability of the weighted section modulus was affected by the intercept, but not the slope. The intercept of the regression line represents the indentation modulus of tissue with no mineral, which should be much lower than bone. Hence the increased explanatory power using the equation with a 0 intercept was not surprising. In fact the relationship between mineral:matrix ratio and indentation modulus appears bimodal with a larger slope between mineral:matrix ratio of 0-4, then a smaller slope beyond a mineral:matrix ratio of 4 (Figure 2.3a). The bimodal response would be vital during rapid growth as the prompt establishment of mechanical competence would be necessary for the bone to withstand everyday loads

during primary mineralization [30, 31]. Secondary mineralization would then follow with a slow but steady accrual of mineralization and increased mechanical properties.

To examine the effect of the exponential coefficient on the prediction of whole bone mechanical behavior, weighted section moduli were calculated using a range of exponential coefficients. Between exponential coefficient values of 3 and 9, the coefficient of determination of the exponentially weighted section modulus changed less than 1%. The initial value of 3.91 selected for this experiment was within 1% of the best coefficient of determination for this data set. An underlying assumption of our approach was that the relationship between Raman mineral content and indentation modulus was proportional to apparent density and Youngs modulus. Both TMD and mineral:matrix ratio from Raman spectroscopy are measures of mineralization, not true gravimetric densities. Vitamin D deficiency primarily affects mineralization leaving the matrix intact [12, 28, 29]. If the amount of collagen and non-collagenous proteins is similar between groups, the mineral:matrix ratio should indicate relative increases in mineral in a given volume of tissue. Additionally a correlation between Raman mineral:matrix and TMD has been confirmed in growing rabbits, and a similar relationship would expected in rats [32]. Assuming a constant Poissons ratio (ν) across all samples, Youngs modulus is proportional to the indentation modulus scaled by $(1 - \nu^2)$. Thus the proportionality of the indentation modulus and the mineral:matrix ratio to TMD and Youngs modulus is plausible.

A limitation of the study is that tissue-level measurements were taken in a single quadrant of the cortex, thus a single regression equation for the mineral:matrix ratio and indentation modulus was used throughout the cortex.

Quadrant-specific differences in tissue properties naturally occur in the cortex and could have obscured diet-induced changes in the indentation modulus [33]. Additional tissue-level data from other quadrants of the femur could validate the use of a single expression or provide location specific tissue property relationships to improve the predictive capability of density-weighted section moduli.

Two different experimental groups were included to create a range of both bone mineralization and mechanical properties. However, whole bone mechanical behavior of the NC1 and NC3 groups was similar despite differences in mineralization density. Although M_F and EI were not different between NC1 and NC3, the values were spread across a range ensuring the regressions were not influenced by highly leveraged data. Similarly at the tissue length scale, tissue-level mechanical properties were unchanged despite differences in local tissue mineralization. The lack of differences in indentation modulus with dietary intervention could indicate that large changes in mineralization are needed to affect indentation modulus and is in accord with a previous study that affected mineralization in rats with a more severe diet [12].

Our approach to predicting mechanical behavior could be further improved by using higher resolution microCT scans. The current study used scans with 25μm voxel size that cannot resolve cellular lacunae, small pores and blood vessels. A higher resolution scan that resolves these architectural features could improve the accuracy of the model and prediction of whole bone mechanical behavior. Additionally the coefficient of determination of 0.54 between indentation modulus and mineral:matrix ratio indicates additional determinants of the indentation modulus remain. Previous studies have shown that the indentation

modulus correlates with other compositional measures such as collagen alignment and carbonate substitution[30, 34]. In the future, including compositional parameters in addition to mineralization could provide a more robust and accurate model to predict whole bone mechanical behavior. Density-weighted section moduli are not as complex as microCT-based finite element models (FEA), but could provide a faster and more economic evaluation of whole bone mechanical behavior. MicroCT-based finite element models can predict 70-98% of the variability in the failure load based on apparent properties, but require the use of super computers or hours of computational time [35, 36]. The density-weighted section moduli calculated using composite beam theory predicted 80% of the variability in failure moment and are less computationally intensive. Improvements in the methodology used to calculate density-weighted section moduli could make this approach equivalent to microCT-based FEA models in terms of predictive capability but more time and cost efficient.

The hierarchical organization of the skeleton produces an amazingly efficient load bearing structure while simultaneously making analysis and modeling challenging. Previously, microCT images in conjunction with composite beam theory and apparent level relationships between elastic modulus and mineralization improved predictions of whole bone mechanical behavior [16–18, 37]. This study is the first to use nanoindentation derived material properties from contralateral limbs of the same animal with composite beam theory to minimize assumptions about tissue heterogeneity and microarchitecture when predicting whole bone mechanical behavior. Although the apparent level derived relationships had more predictive power than the tissue-level data derived linear relationships, the composite beam model in this paper is an improved method to extrapolate tissue-level data to macro-scale mechanical behavior in a miner-

alization defect model.

References

1. Currey JD. The mechanical consequences of variation in the mineral content of bone. Journal of Biomechanics 1969;2:1–11.

2. Currey JD. Effects of differences in mineralization on the mechanical properties of bone. Philosophical Transactions of the Royal Society of London. B, Biological Sciences 1984;304:509–518.

3. Currey JD. The effect of porosity and mineral content on the Young's modulus of elasticity of compact bone. Journal of Biomechanics 1988;21:131 – 139.

4. Aspray TJ, Prentice A, Cole TJ, Sawo Y, Reeve J, and Francis RM. Low bone mineral content is common but osteoporotic fractures are rare in elderly rural Gambian women. Journal of Bone and Mineral Research 1996;11:1019–1025.

5. Kanis JA. Diagnosis of osteoporosis and assessment of fracture risk. Lancet (London, England) 2002;359:1929–1936.

6. Kanis JA, Johnell O, Odén A, Johansson H, and McCloskey E. FRAX and the assessment of fracture probability in men and women from the UK. Osteoporosis International 2008;19:385–397.

7. Watts NB and Diab DL. A backbone for FRAX? Journal of Bone and Mineral Research 2011;26:458–459.

8. Haguenauer D, Welch V, Shea B, Tugwell P, Adachi JD, and Wells G. Fluoride for the treatment of postmenopausal osteoporotic fractures: a meta-analysis. Osteoporosis International 2000;11:727–738.

9. Meunier PJ, Sebert JL, Reginster JY, Briancon D, Appelboom T, Netter P, Loeb G, Rouillon A, Barry S, and Evreux JC. Fluoride salts are no better at preventing new vertebral fractures than calcium-vitamin D in postmenopausal osteoporosis: the FAVOStudy. Osteoporosis International 1998;8:4–12.

10. Cummings SR, Karpf DB, Harris F, Genant HK, Ensrud K, LaCroix AZ, and Black DM. Improvement in spine bone density and reduction in risk of vertebral fractures during treatment with antiresorptive drugs. The American Journal of Medicine 2002;112:281–289.

11. Ettinger B, Black DM, Mitlak BH, Knickerbocker RK, Nickelsen T, Genant HK, Christiansen C, Delmas PD, Zanchetta JR, and Stakkestad J. Reduction of vertebral fracture risk in postmenopausal women with osteoporosis treated with raloxifene. The Journal of the American Medical Association 1999;282:637–645.

12. Donnelly E, Boskey AL, Baker SP, and Meulen MCH Van der. Effects of tissue age on bone tissue material composition and nanomechanical properties in the rat cortex. Journal of Biomedical Materials Research Part A 2010;92:1048–1056.

13. Rho JY, Zioupos P, Currey JD, and Pharr GM. Microstructural elasticity and regional heterogeneity in human femoral bone of various ages examined by nano-indentation. Journal of Biomechanics 2002;35:189–198.

14. Silva MJ, Brodt MD, Fan Z, and Rho JY. Nanoindentation and whole-bone bending estimates of material properties in bones from the senescence accelerated mouse SAMP6. Journal of Biomechanics 2004;37:1639–1646.

15. Sun L, Fan Y, Li D, Zhao F, Xie T, Yang X, and Gu Z. Evaluation of the mechanical properties of rat bone under simulated microgravity using nanoindentation. Acta Biomaterialia 2009;5:3506–3511.

16. Bhatavadekar NB, Daegling DJ, and Rapoff AJ. Application of an image-based weighted measure of skeletal bending stiffness to great ape mandibles. American Journal of Physical Anthropology 2006;131:243–251.

17. Corcoran TA, Sandier RB, Myers ER, Lebowitz HH, and Hayes WC. Calculation of cross-sectional geometry of bone from CT images with application in postmenopausal women. Journal of Computer Assisted Tomography 1994;18:626–633.

18. Hong J, Cabe GD, Tedrow JR, Hipp JA, and Snyder BD. Failure of trabecular bone with simulated lytic defects can be predicted non-invasively by structural analysis. Journal of Orthopaedic Research 2006;22:479–486.

19. Sonnenberg J, Pansini AR, and Christakos S. Vitamin D-Dependent Rat Renal Calcium-Binding Protein: Development of a Radioimmu no assay, Tissue Distribution, and Immunologic Identification. Endocrinology 1984;115:640–648.

20. Fritton JC, Myers ER, Wright TM, and Meulen MCH van der. Loading induces site-specific increases in mineral content assessed by microcomputed tomography of the mouse tibia. Bone 2005;36:1030–1038.

21. Donnelly E, Baker SP, Boskey AL, and Meulen MCH van der. Effects of surface roughness and maximum load on the mechanical properties of cancellous bone measured by nanoindentation. Journal of Biomedical Materials Research Part A 2006;77:426–435.

22. Oliver WC and Pharr GM. Improved technique for determining hardness and elastic modulus using load and displacement sensing indentation experiments. Journal of Materials Research 1992;7:1564–1583.

23. Draper ERC, Morris MD, Camacho NP, Matousek P, Towrie M, Parker AW, and Goodship AE. Novel Assessment of Bone Using Time-Resolved Transcutaneous Raman Spectroscopy. Journal of Bone and Mineral Research 2005;20:1968–1972.

24. Timlin JA, Carden A, Morris MD, Rajachar RM, and Kohn DH. Raman spectroscopic imaging markers for fatigue-related microdamage in bovine bone. Analytical Chemistry 2000;72:2229–2236.

25. Bartel DL, Davy DT, and Keaveny TM. Orthopaedic Biomechanics. Pearson/Prentice Hall, 2006.

26. Balooch M, Habelitz S, Kinney JH, Marshall SJ, and Marshall GW. Mechanical properties of mineralized collagen fibrils as influenced by demineralization. Journal of Structural Biology 2008;162:404–410.

27. Schaffler MB and Burr DB. Stiffness of compact bone: Effects of porosity and density. Journal of Biomechanics 1988;21:13 –16.

28. Baylink D, Stauffer M, Wergedal J, and Rich C. Formation, mineralization, and resorption of bone in vitamin Ddeficient rats. Journal of Clinical Investigation 1970;49:1122.

29. Einhorn TA, Bonnarens F, and Burstein AH. The contributions of dietary protein and mineral to the healing of experimental fractures. A biomechanical study. The Journal of Bone and Joint Surgery 1986;68:1389.

30. Busa B, Miller L, Rubin C, Qin YX, and Judex S. Rapid establishment of chemical and mechanical properties during lamellar bone formation. Calcified Tissue International 2005;77:386–394.

31. Wergedal JE and Baylink DJ. Electron microprobe measurements of bone mineralization rate in vivo. American Journal of Physiology–Legacy Content 1974;226:345–352.

32. Turunen MJ, Saarakkala S, Rieppo L, Helminen HJ, Jurvelin JS, and Isaksson H. Comparison between infrared and Raman spectroscopic analysis of maturing rabbit cortical bone. Applied Spectroscopy 2011;65:595–603.

33. Akkus O, Adar F, and Schaffler MB. Age-related changes in physicochemical properties of mineral crystals are related to impaired mechanical function of cortical bone. Bone 2004;34:443–453.

34. Donnelly E, Williams RM, Downs SA, Dickinson ME, Baker SP, and Meulen MCH van der. Quasistatic and dynamic nanomechanical properties of cancellous bone tissue relate to collagen content and organization. Journal of Materials Research 2006;2:3.

35. Imai K, Ohnishi I, Yamamoto S, and Nakamura K. In vivo assessment of lumbar vertebral strength in elderly women using computed tomography-based nonlinear finite element model. Spine 2008;33:27–32.

36. Pistoia W, Van Rietbergen B, Lochmüller EM, Lill CA, Eckstein F, and Rüegsegger P. Estimation of distal radius failure load with micro-finite element analysis models based on three-dimensional peripheral quantitative computed tomography images. Bone 2002;30:842–848.

37. Cory E, Nazarian A, Entezari V, Vartanians V, Müller R, and Snyder BD. Compressive axial mechanical properties of rat bone as functions of bone

volume fraction, apparent density and micro-ct based mineral density. Journal of Biomechanics 2010;43:953–960.

CHAPTER 3

EFFECTS OF MINERAL CRYSTALLINITY ON TISSUE-LEVEL AND WHOLE BONE MECHANICAL BEHAVIOR

3.1 Introduction

Whole bone mechanical behavior depends on bone mass, geometry and material properties. Due to the hierarchical nature of bone, defining the material properties of bone tissue depends on the length scale at which testing is performed, leading to the distinction between apparent level and intrinsic mechanical properties of bone tissue [1, 2]. Studies utilizing whole bone or microbeam testing calculate apparent level mechanical properties that do not take into account tissue microstructure and heterogeneity. To measure intrinsic mechanical properties the test volume must be small enough to avoid the effects of tissue heterogeneities and discontinuities due to microstructural features. Nanoindentation, a depth sensing indentation technique, is able to sample volumes of tissue that lie within a single microstructural feature, and thus able to measure differences in the mechanical properties of distinct tissue features that have also been shown to have differences in tissue-level composition [3–6].

The relationship between composition and intrinsic mechanical properties is of interest because age and disease related changes in apparent mechanical behavior are accompanied by compositional changes of bone that can be measured at both the whole bone and tissue-level [7–9]. Aging increases tissue mineralization and crystallinity while decreasing whole bone strength and stiffness [9–14]. In diseases such as osteomalacia bone mineral density and whole bone stiffness are decreased [15, 16]. Because of the compositional changes that accompany

changes in apparent level mechanical behavior, the composition-mechanical behavior relationship has also been investigated at the tissue-level. Mineralization and carbonate substitution, two compositional metrics associated with the mineral phase of bone have been correlated with changes in tissue-level mechanical properties as measured by nanoindentation [17–19]. Mineralization and carbonate substitution were only able to predict 33-55% of the variability in tissue-level mechanical properties indicating other compositional parameters may also affect the mechanical properties.

Crystallinity is a quantity pertaining to the mineral phase of bone that is influenced by the crystallite size, lattice strain and stress, and crystal perfection. The importance of crystallinity on intrinsic material properties has been suggested through the use of computational molecular models and the examination of diseases that disrupt the mineral phase of bone [20–22]. Changes in crystallinity due to aging and osteoporosis are concomitant with other compositional changes making it difficult to isolate the effects of crystallinity. Fluoride treatment, both in vivo and in vitro, provides a method to alter crystallinity and mechanical behavior of bone in a controlled manner. Changes to whole bone strength and stiffness and increases in ductility have been observed with fluoride treatment [23–26]. These studies only examined whole bone mechanical behavior and estimated apparent level material properties from whole bone tests and the affect of crystallinity on tissue-level properties has not been studied.

The goal of the current study was to understand the effects of crystallinity on tissue-level material properties and whole bone mechanical behavior in an in vivo model. A combination of compositional and mechanical testing methodologies at both the whole bone and tissue-level length scales were used to as-

sess mechanical behavior and composition. Changes in the crystallinity of the mineral phase could disrupt interfaces between collagen and mineral crystals changing the material level properties the tissue and ultimately altering whole bone mechanical behavior [20, 21]. We hypothesized that the changes in crystallinity through in vivo fluoride supplementation would reduce measures of whole bone mechanical behavior and alter tissue-level material properties independent of changes in whole bone geometry and mineralization.

3.2 Methods

62 male Sprague-Dawley rats (Charles River, Wilmington, MA) were divided into 3 groups at 3 wks of age and started on their respective treatments. The Control group was given unfluoridated tap water for the duration of the 10 week experiment (n = 20). The F100 and F150 groups were given 100 ppm and 150 ppm fluoride, respectively, in their drinking water as NaF (Sigma-Aldrich, St. Louis, MO) for the duration of the 10 week experiment (n = 21/group). Fluorochrome injections were given at 28 d, 14 d, and 4 d before euthanasia to distinguish 4 tissue age zones, 0-4 d, 5-14 d, 15-28 d, and 29 d+. All procedures were approved by Cornell Universitys Institutional Animal Care and Use Committee (IACUC). Serum collected from a subset of animals (n = 10/group) at euthanasia was used to validate increased serum fluoride levels using a fluoride ion selective electrode [27]. To every 950 μL of serum, 50 μL of TISAB III (Sigma-Aldrich, St. Louis, MO) was added and vortexed. The fluoride electrode was calibrated using known dilutions of 100, 10, 1, 0.1, 0.01 ppm fluoride solutions. The voltage was allowed to stabilize for 4 minutes then recorded. Samples were measured in a similar fashion. Left and right femurs were removed and stored

in saline soaked gauze at -20 degC until use.

3.2.1 Whole bone testing

All soft tissue was removed from right femurs. Femurs were scanned using microCT with a 25 μm isotropic voxel size (eXplore CT 120, GE Healthcare, Waukesha, WI). All bones were scanned at 80 kV, 32 mA, 100 msec exposure with 1 image every 0.5 for 360. Mineral density was calibrated according to the manufacturer using a calibration phantom with SB3 which has a mineral density of 1073 mg/cc. Femur lengths were measured from microCT scans. Tissue mineral density, tissue mineral content, cortical area, the moment of inertia about the medial-lateral axis were calculated for a 3 mm thick volume of interest from the midshaft of the femurs (MicroView 2.2, GE Healthcare, Waukesha, WI). Right femurs were then tested to failure in 3 point bending (858 Mini Bionix, MTS, Eden Prairie, MN) with a fixed span width of 17 mm and a load rate of 0.05 mm/sec in the anterior-posterior direction. Failure moment, bending stiffness, and displacement at failure were calculated using the span width and the load and displacement data from each test.

X-ray Diffraction

After whole bone mechanical testing, a subset of the broken femurs was segments were used to measure whole bone crystallinity using x-ray diffraction (XRD) (n=10/group). Diaphyseal regions of the broken femurs were isolated, cleaned, defatted in a solution of methanol:chloroform, lyophilized, and cryogenically milled. XRD spectra of powdered samples were measured from 24°

2θ to 38° 2θ in step-scan mode, with a step size of 0.02° 2θ (Scintag Theta-Theta X-ray Diffractometer). X-ray diffraction peaks at 25.8° 2θ (Miller index 002) and between 31° and 34° 2θ (Miller indices 211, 112, 300, 202) were analyzed to quantify changes in crystallinity along the c-axis and perpendicular to the c-axis respectively [28].β_{002} was the standard deviation of the peak representing the 002 index. For the 4 peaks in the 31-35 2 θ region, all peaks were assumed to be Gaussian with the same standard deviation, β_{perp}. β_{perp} was iteratively determined.

3.2.2 tissue-level Properties

Left femurs were used for tissue-level analyses (n = 5/group). Soft tissue was removed and femurs were dehydrated in ascending concentrations of ethanol then embedded in polymethylmethacrylate. 3 mm thick sections from the mid-diaphysis were removed and polished anhydrously [6]. For each sample, 5 indentations were made with a Berkovich tip in the middle of the zones defined by the tetracycline labels (Triboindenter, Hysitron, Minneapolis, MN). Indents were created using a two-trapezoidal load function with peak loads of 500 and 1000 μN (load rate± 50μN, 10s hold time). The indentation modulus (E_i) and hardness (H) were calculated from the 500μN load-displacement curve [29].

The 1000 μN load indentations created fiduciary marks so that Raman spectroscopic measurements could be co-localized. Raman spectra were collected at the nanoindentation sites using an optical microscope (inVia, Renishaw, Gloucestershire, UK) equipped with a 785 nm laser and 50 x, 0.75 NA objective. The resulting spot size was 2 μm. At each location 3 acquisitions each with 10 s

exposures were averaged. Spectra were background subtracted and smoothed (WiRE V2.0, Renishaw; in-house Matlab code, The Mathworks). Tissue mineralization was examined using the peak height ratio of the phosphate ν_1 (1650 cm^{-1}) and CH_2 wag peak (1450 cm^{-1}). Mineral crystallinity was examined based on the full width half at half the maximum (FWHM) and peak position of the phosphate ν_1 peak (960 cm^{-1}) [23]. Spectra with large backgrounds due to autofluorescence of the tissue were removed.

3.2.3 Statistical Methods

A one-way analysis of variance with Tukey-Kramer post-hoc was used to identify differences in whole bone outcome measures between all groups (JMP 9.0.2, SAS Institute). For tissue-level outcomes, a two-way ANOVA was performed with tissue age zone and treatment group as main effects to determine differences in E_i, H, mineral:matrix ratio, and FWHM of the phosphate peak. Linear regressions determined the correlations between both whole bone composition and mechanical behavior, and whole bone geometric measures and mechanical behavior.

3.3 Results

Ten weeks of fluoride supplementation increased serum fluoride levels and did not alter cortical bone geometry or average whole bone mineralization as measured by microCT (Figure 3.1). Specifically, the cross sectional area, moment of inertia and tissue mineral density did not change in the mid-diaphysis. Overall

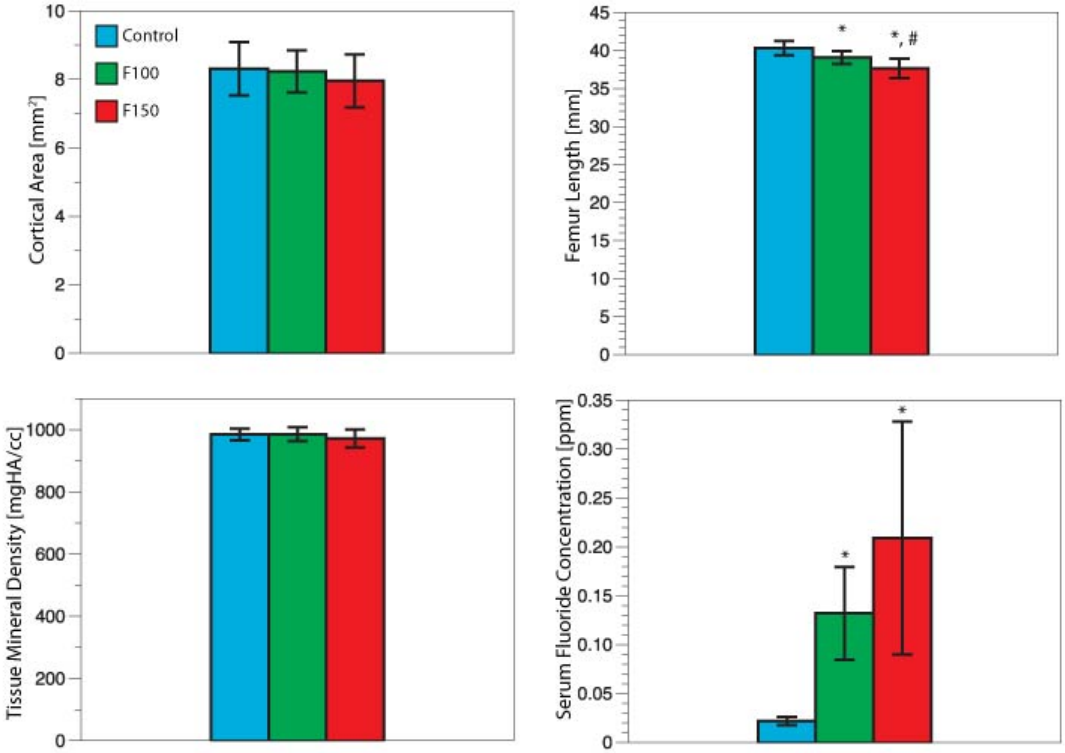

Figure 3.1: Cortical area of the mid-diaphysis of the femur, femur length, and tissue mineral density as measured from microCT. Mean ± standard deviation. ∗ different from Control. # different from F100.

femur length decreased with fluoride treatment. The F100 and F150 groups had 3% and 6% shorter femurs than controls. Fluoride supplementation reduced whole bone mechanical behavior as measured by the bending stiffness and failure moment (Figure 3.2). The bending stiffness (EI) was reduced 19% and 38% in the F100 and F150 groups respectively. The failure moment was reduced by 17% and 29% in the F100 and F150 groups, respectively. Fluoride treatment also increased the deformation at failure by 44% and 78% in the F100 and F150 groups compared to Controls. In vivo fluoride supplementation increased bone mineral crystallinity in a crystallographic direction specific manner (Figure 3.3). Crystallinity along the c-axis of the hydroxyapatite crystals did not change with

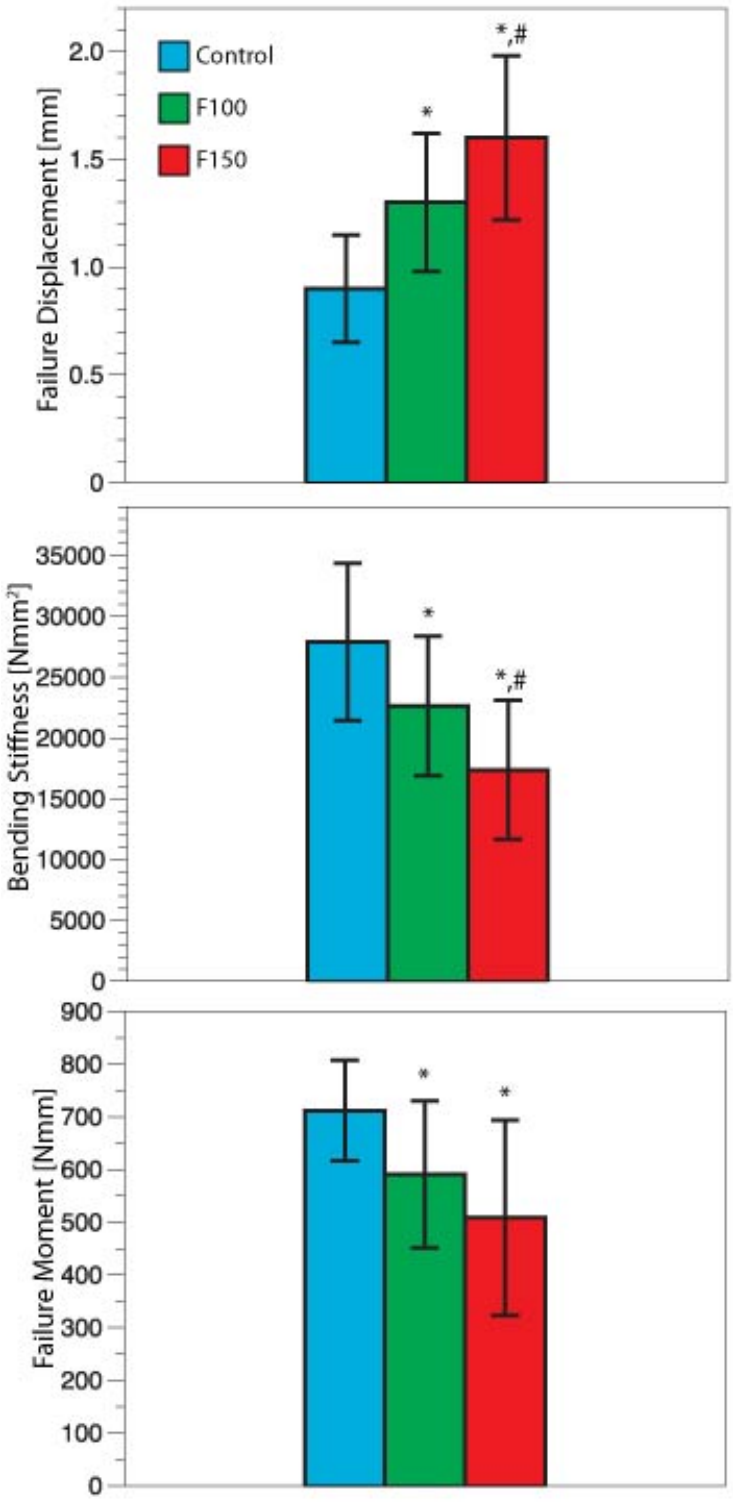

Figure 3.2: Results of whole bone bending tests. Displacement at failure increased with fluoride treatment while the bending stiffness and failure moments decreased. Mean ± standard deviation. $*$ different from Control, # different from F100, $p \leq 0.05$.

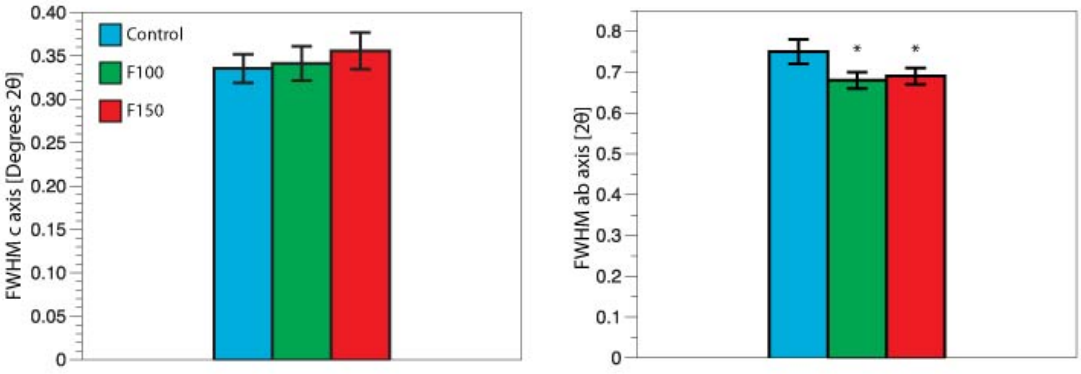

Figure 3.3: FWHM of peaks from XRD indicative of crystallinity along the c axis and ab axis. Mean ± standard deviation. ∗ different from Control, # different from F100, $p \leq 0.05$.

fluoride treatment as measured by XRD. However, the crystallinity perpendicular to the c-axis increased 8%-9% with fluoride treatment.

3.3.1 Tissue-level results

Tissue-level material properties, the indentation modulus and hardness, followed similar trends across the cortex with tissue age (Figure 3.4). Fluoride status was a significant factor for both the indentation modulus and hardness. The F100 group had larger indentation modulus and hardness than the Control and F150 groups, the Control and F150 group values were not different. Tissue age zone was also a significant factor for both the indentation modulus and hardness. Both parameters increased with increasing tissue age. Effects of tissue age zone did not change with treatment. Both experimental group and tissue age zones were significant factors for tissue-level mineralization (Figure 3.5). The mineral:matrix ratio increased with increasing tissue age, and the F100 group had a higher mineral:matrix ratio than the Control and F150 groups. Ad-

ditionally, the effect of fluoride treatment differed by tissue age zone for the mineral:matrix ratio. In the 15-28 d tissue, the mineralization of the F100 group was higher than that of the Control group. The FWHM of the phosphate peak from Raman spectroscopy did not change with fluoride treatment. FWHM decreased with tissue age: the in the intracortical tissue (4-29d+) was more crystalline compared to the youngest tissue (0-4d). The peak position of the phosphate ν_1 peak increased in both fluoride treated groups compared with Controls.

3.3.2 Predicting whole bone mechanical behavior

Whole bone mechanical behavior outcomes were predicted using measures of whole bone geometry, mineralization, and crystallinity (Figure 3.6). Averaged tissue-level parameters were not significant predictors of the bending stiffness or the failure moment. For the subset of femurs used for XRD, the best predictor for the failure moment and bending stiffness was femur length, predicting 35% and 32% of the variability in each outcome measure, respectively. XRD crystallinity measurements with femur length improved the prediction for the failure moment (r^2 = 0.49) however it did not improve the prediction for the bending stiffness.

3.4 Discussion

Measures of whole bone mechanical behavior, bending stiffness and failure moment, were reduced in fluoride treated rats. Similar to previous studies the whole bone bending stiffness and failure moment were reduced while the de-

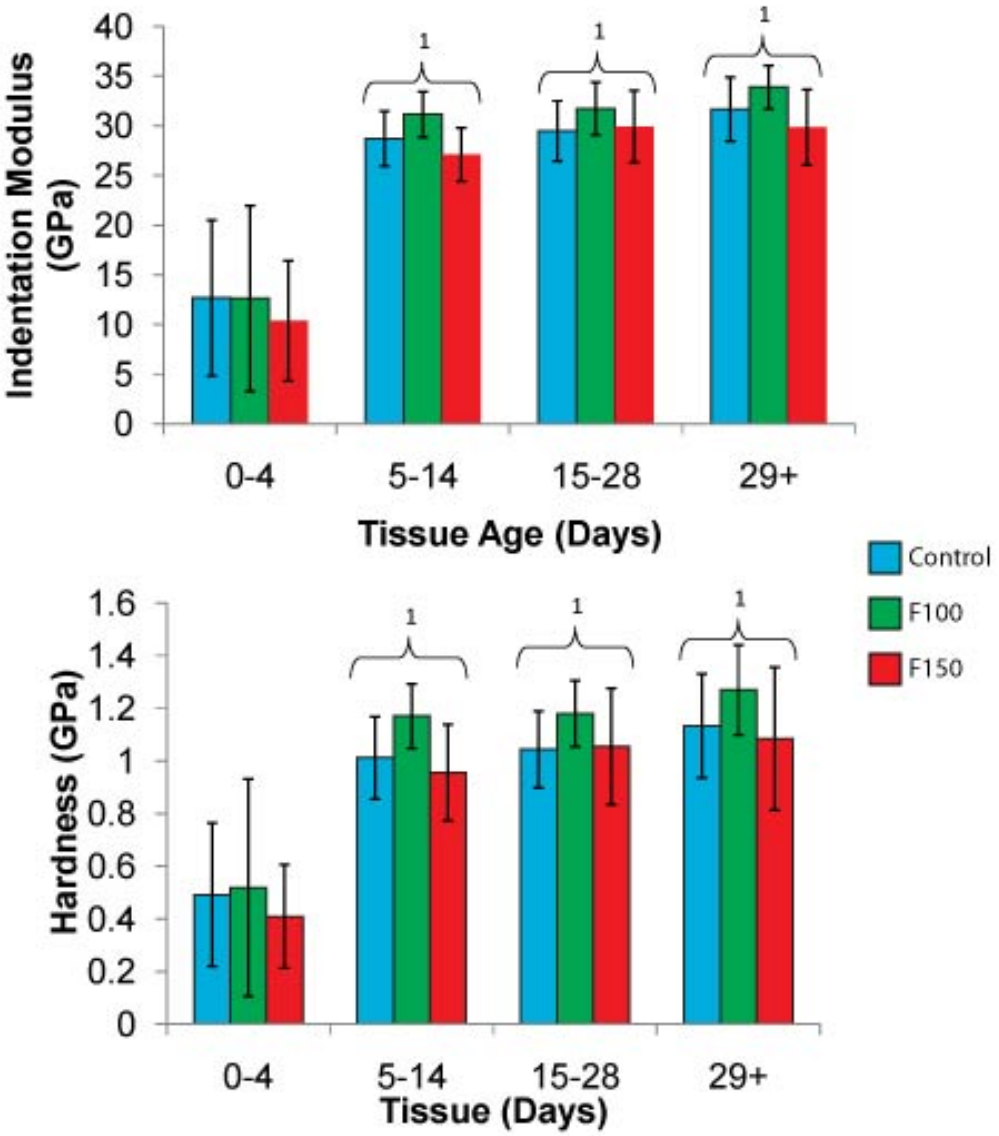

Figure 3.4: Indentation modulus and hardness as a function of tissue age in days. Indentation modulus and hardness depended on tissue age but not fluoride treatment. Mean ± standard deviation. 1 indicates different from 0-4 day tissue $p \leq 0.05$.

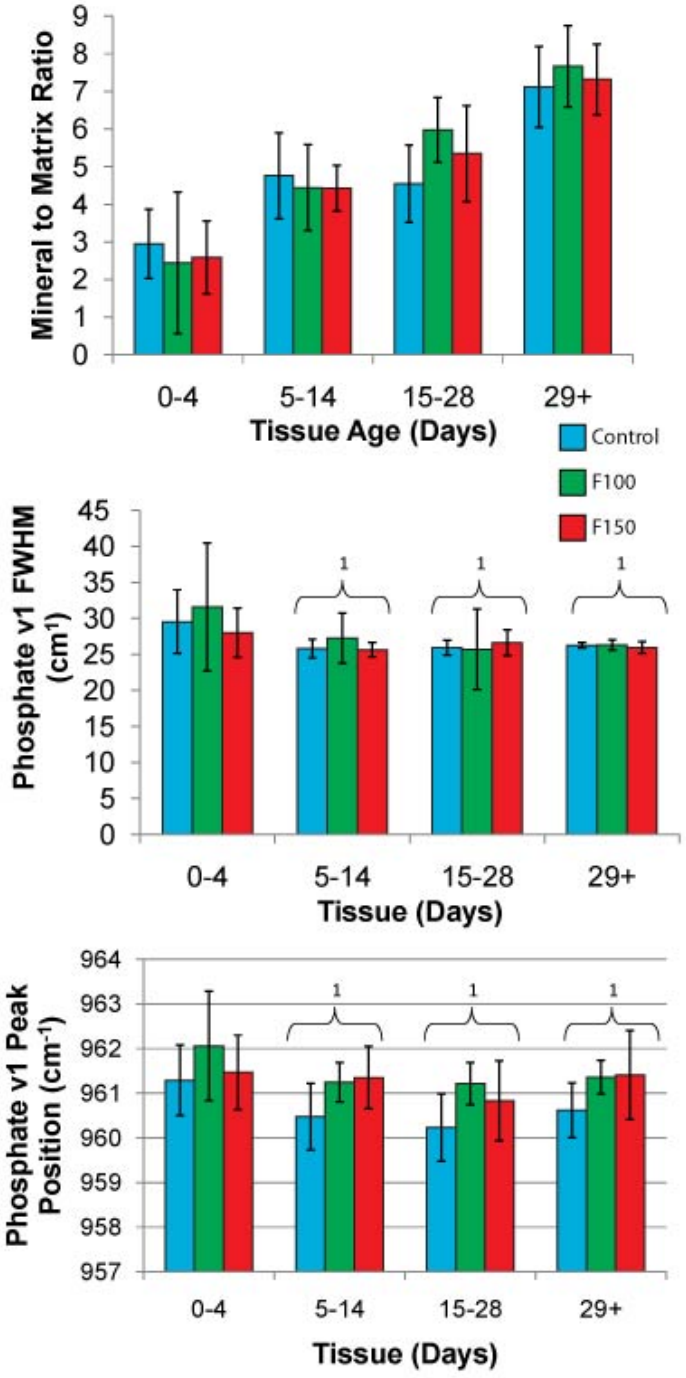

Figure 3.5: Mineral to matrix ratio, FWHM and peak position of the phosphate 1 peak as a function of age. All Raman parameters were different in the youngest tissue (0-4 d) compared to the intracortical tissue. The mineral:matrix ratio was larger in the F100 group compared to Control and F150. There were no group dependent differences in the FWHM. The peak position shifted to higher wave numbers with fluoride treatment. 1: different from 0-4 d, 2: different from 5-14 d, 3: different from 15-28 d, $p \leq 0.05$.

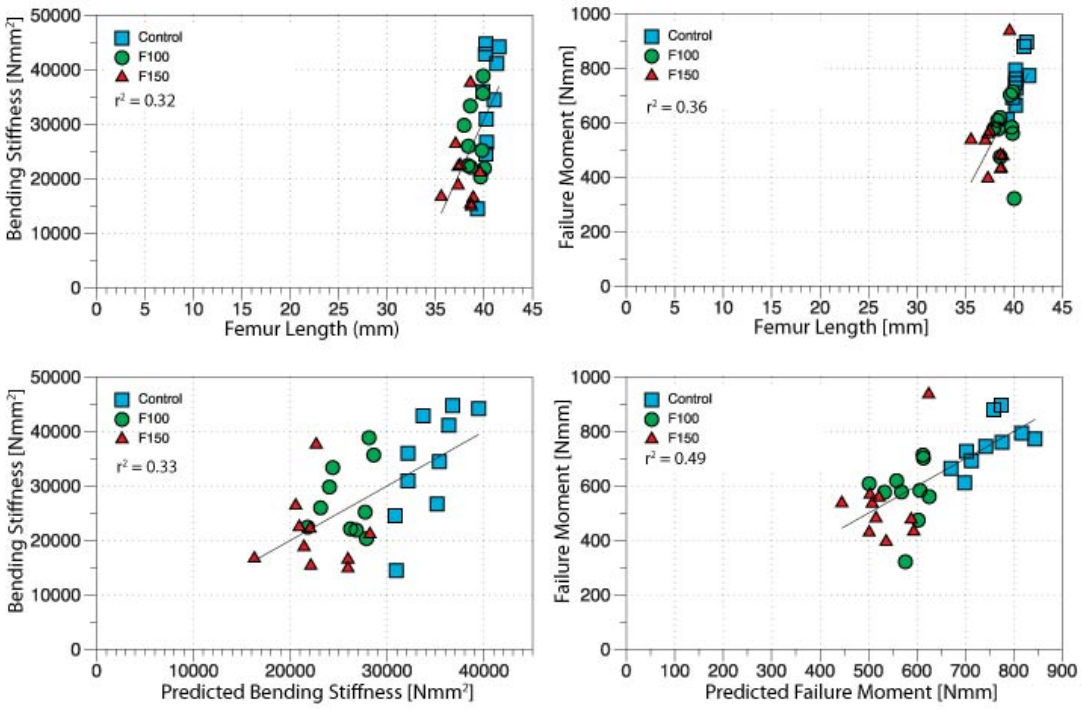

Figure 3.6: Linear regression for the bending stiffness and failure moment using femur length. Multiple regressions for bending stiffness and failure moment using femur length and ab axis crystallinity as predictors.

formation to failure increased [23, 24, 26]. The best predictor for the failure moment and bending stiffness was femur length. Femur length was reduced proportional to fluoride treatment and was likely indicative of overall fluoride status. In the current study, despite comparable cross-sectional areas and whole bone mineralization, local tissue material properties were not significant predictors of whole bone mechanical behavior, suggesting the relationship between nanoscale and whole bone mechanical behavior was dominated by the response of microstructural features or not captured by nanoindentation measures.

Whole bone mineralization as measured by TMD and tissue-level mineralization measurements had similar trends, the F100 group was more mineralized

than the Control and F150 groups. However, the differences in TMD did not reach significance. The intermediate dose of fluoride (100 ppm) increased the mineral:matrix ratio compared to animas given 150 ppm or 0 ppm fluoride. The indentation modulus and hardness also increased in the F100 group in accord with previously established correlations between material properties and mineralization [17–19]. Clear dose and duration dependent effects of fluoride are evident, as lower doses or shorter exposure times do not change mechanical behavior [30–32]. The non-monotonic change in material properties with fluoride could be attributed to the dose sensitivity of fluoride induced effects.

Similar non-monotonic dose-dependent changes in the hardness of cortical bone from fluoride treated rats has been found previously, but whole bone mechanical behavior was not concurrently examined [33]. The hardness of the 30 ppm group increased while those of the 90 ppm and 120 ppm groups were not different with respect to the Control group. The only other study to examine tissue-level material properties from fluoride treated animals measured the elastic moduli of fluoride treated rabbit cortical bone using acoustic velocity measurements [34]. No changes in elastic moduli from acoustic velocity measurements were detected despite changes in whole bone stiffness and strength. Architectural features of the tissue that lie between the length scales of nanoindentation and whole bone testing and could have been affected by crystallinity changes and contributed to changes in whole bone mechanical behavior. Interfibrillar strain has been shown to facilitate the majority of macroscopic tissue strain [35], and changes in crystallinity could have altered the interfibrillar binding with extra fibrillar matrix perturbing the elastic response of the matrix.

Raman spectroscopy has been used in vitro previously to examine changes in

fluoride induced crystallinity changes. Both a decrease in the FWHM and shift of the phosphate ν_1 peak were found after in vitro exposure of mouse cortical bone to a fluoride solution for 12 hours [23]. The exact mechanisms by which fluoride is incorporated into bone tissue are not well understood; however evidence suggests both a biologically mediated process as well as a physiochemical process [36–40]. Thus the effects on crystal size, lattice strain, or lattice substitutions could differ between in vivo and in vitro fluoridation. Changes in any one aspect of crystallinity could manifest themselves as different spectroscopic changes.

The ductility of cortical bone increased 44-78% in fluoride treated animals. In this study fluoride supplementation was expected to alter the mineral phase of the bone. Post-yield behavior and toughness have been primarily related to the collagenous component of bone [41, 42]. Mouse models with altered collagen matrices such as the oim/oim and SAMP6 mice, have different collagen abnormalities but in both models, the whole bone failure strain decreased [43, 44]. The strain to failure of tension tests of demineralized bones from both strains of mice were not different from controls suggesting the mineral component or the interface between the mineral and collagen compromised thus and altered the mechanical behavior of undemineralized bones. From molecular dynamics simulation, changes in crystallite size alter the bonding with collagen molecules, and ultimately the tensile modulus [20]. Changes to either the mineral or collagen could disturb the interaction between mineral particles and collagen or the extra-fibrillar matrix which may be key elements of whole bone mechanical behavior.

Fluoride reduced bending stiffness and failure moment without altering cor-

tical geometry or mineralization suggesting the differences in whole bone behavior were due to fluoride induced changes in tissue mechanical properties. Surprisingly there were no differences in indentation modulus or hardness with fluoride treatment. The lack of correlations between whole bone and tissue-level mechanical behavior could be attributed to differences in sample preparation. The effects of fluoride treatment on nanoindentation measures could have been masked by the required sample dehydration and embedding process. To reduce surface roughness effects on nanoindentation measurements, samples must be dehydrated and embedded [45], while for whole bone bending samples are not chemically treated and constantly hydrated with phosphate buffered saline. Sample dehydration alone affects both the elastic and plastic response of bone tissue. Dehydration increases the indentation modulus and hardness as measured by nanoindentation [46–48]. For cortical beam samples, dehydration increases strength and decreases the displacement at failure [49, 50]. Dehydration clearly affects both the elastic and plastic response of bone tissue and could have obscured fluoride induced differences in indentation modulus and hardness.

Additionally, the lack of correlations between whole bone and tissue-level mechanical properties could be due to the difference in stress states caused by nanoindentation and three point bending. For a whole bone loaded in three point bending with a positive moment, failure starts at the lower periosteal surface because the tensile stresses exceed the ultimate tensile strength of bone before the ultimate compressive strength is exceeded. The tensile stress initiates a crack on the lower periosteal surface that propagates through the cortex. Based on the elastic contact of a sphere and a plane surface, the stress in the direction of loading is a compressive stress that is larger than the in-plane compressive stresses [51]. Because the stress is not hydrostatic for nanoindentation, the ma-

terial beneath the indenter tip is under compressive and shear stresses. The impact of differing stress states on bone tissue have been demonstrated by the presence of different forms of microdamage associated with tensile and compressive stresses [52, 53]. Plastic deformation mechanisms for nanoindentation and three point bending are likely not the same and could be affected differently by the compositional changes induced by fluoride supplementation.

A limitation of using fluoride supplementation is that fluoride related changes in bone composition and mechanical behavior vary across species, dose, and exposure duration [38]. At larger doses detrimental systemic effects have been observed in addition to changes to bone mechanical behavior such as in cases of fluoride toxicity [54]. Due to the multifaceted action of fluoride, both reductions in mineralization due to increased mineralization lag times and increased in mineralization have been documented [55]. Therefore comparisons with other studies using different animals, or vastly different doses and experimental duration must be made with caution. Fluoride treatment in growing rats reduced measures of whole bone mechanical behavior independent of changes in cross-sectional geometry or mineralization of the cortex. Contrary to our hypothesis, the reduction of the bending stiffness and failure moment were not accompanied by similar changes to the intrinsic mechanical properties as measured by nanoindentation. The indents, which sampled volumes of tissue approximately 1 μm^3, were smaller than most microstructural features, suggesting that the behavior of interfaces between microstructural components may influence whole bone mechanical behavior and failure more than the individual microstructural constituents. Although a correlation between material properties and whole bone mechanical behavior in fluoride treated animals was not found in this study, examination of intermediate length scales could delineate a mech-

anism through which fluoride induced changes in crystallinity affect material properties and ultimately whole bone mechanical behavior.

References

1. Silva MJ, Brodt MD, Fan Z, and Rho JY. Nanoindentation and whole-bone bending estimates of material properties in bones from the senescence accelerated mouse SAMP6. Journal of Biomechanics 2004;37:1639–1646.

2. Akhter MP, Fan Z, and Rho JY. Bone intrinsic material properties in three inbred mouse strains. Calcified Tissue International 2004;75:416–420.

3. Rho JY, Tsui TY, and Pharr GM. Elastic properties of human cortical and trabecular lamellar bone measured by nanoindentation. Biomaterials 1997;18:1325–1330.

4. Rho JY, Zioupos P, Currey JD, and Pharr GM. Variations in the individual thick lamellar properties within osteons by nanoindentation. Bone 1999;25:295–300.

5. Rho JY, Zioupos P, Currey JD, and Pharr GM. Microstructural elasticity and regional heterogeneity in human femoral bone of various ages examined by nano-indentation. Journal of Biomechanics 2002;35:189–198.

6. Donnelly E, Williams RM, Downs SA, Dickinson ME, Baker SP, and Meulen MCH van der. Quasistatic and dynamic nanomechanical properties of cancellous bone tissue relate to collagen content and organization. Journal of Materials Research 2006;21:2106–2117.

7. Mosekilde L, Mosekilde L, and Danielsen CC. Biomechanical competence of vertebral trabecular bone in relation to ash density and age in normal individuals. Bone 1987;8:79–85.

8. Mosekilde LI and Mosekilde LE. Iliac crest trabecular bone volume as predictor for vertebral compressive strength, ash density and trabecular bone volume in normal individuals. Bone 1988;9:195–199.

9. Weaver JK and Chalmers J. Cancellous Bone: Its Strength and Changes with Aging and an Evaluation of Some Methods for Measuring Its Mineral Content I. Age Changes in Cancellous Bone. The Journal of Bone and Joint Surgery 1966;48:289–299.

10. Gourion-Arsiquaud S, Lukashova L, Power J, Loveridge N, Reeve J, and Boskey AL. Fourier transformed infra-red imaging of femoral neck bone: Reduced heterogeneity of mineral-to-matrix and carbonate-to-phosphate and more variable crystallinity in treatment-naïve fracture cases compared to fracture-free controls. Journal of Bone and Mineral Research 2012.

11. Zioupos P and Currey JD. Changes in the stiffness, strength, and toughness of human cortical bone with age. Bone 1998;22:57–66.

12. Grynpas M. Age and disease-related changes in the mineral of bone. Calcified Tissue International 1993;53:57–64.

13. Bonar LC, Roufosse AH, Sabine WK, Grynpas MD, and Glimcher MJ. X-ray diffraction studies of the crystallinity of bone mineral in newly synthesized and density fractionated bone. Calcified Tissue International 1983;35:202–209.

14. Currey JD, Brear K, and Zioupos P. The effects of ageing and changes in mineral content in degrading the toughness of human femora. Journal of Biomechanics 1996;29:257–260.

15. Turner CH. Biomechanics of bone: determinants of skeletal fragility and bone quality. Osteoporosis International 2002;13:97–104.

16. Faibish D, Gomes A, Boivin G, Binderman I, and Boskey AL. Infrared imaging of calcified tissue in bone biopsies from adults with osteomalacia. Bone 2005;36:6–12.

17. Donnelly E, Boskey AL, Baker SP, and Meulen MCH Van der. Effects of tissue age on bone tissue material composition and nanomechanical properties in the rat cortex. Journal of Biomedical Materials Research Part A 2010;92:1048–1056.

18. Busa B, Miller L, Rubin C, Qin YX, and Judex S. Rapid establishment of chemical and mechanical properties during lamellar bone formation. Calcified Tissue International 2005;77:386–394.

19. Miller LM, Little W, Schirmer A, Sheik F, Busa B, and Judex S. Accretion of bone quantity and quality in the developing mouse skeleton. Journal of Bone and Mineral Research 2007;22:1037–1045.

20. Qin Z, Gautieri A, Nair AK, Inbar H, and Buehler MJ. Thickness of Hydroxyapatite Nanocrystal Controls Mechanical Properties of the Collagen–Hydroxyapatite Interface. Langmuir 2012;28:1982–1992.

21. Landis WJ. The strength of a calcified tissue depends in part on the molecular structure and organization of its constituent mineral crystals in their organic matrix. Bone 1995;16:533–544.

22. Landis WJ. Tomographic imaging of collagen-mineral interaction: Implications for osteogenesis imperfecta. Connective Tissue Research 1995;31:287–290.

23. Freeman JJ, Wopenka B, Silva MJ, and Pasteris JD. Raman spectroscopic detection of changes in bioapatite in mouse femora as a function of age and in vitro fluoride treatment. Calcified Tissue International 2001;68:156–162.

24. Turner CH, Akhter M, and Heaney RP. The effects of fluoridated water on bone strength. Journal of Orthopaedic Research 1992;10:581–587.

25. Turner CH, Dunipace AJ, and Einhorn TA. On fluoride and bone strength. Calcified Tissue International 1993;53:289–290.

26. Turner CH, Hasegawa K, Zhang W, Wilson M, Li Y, and Dunipace AJ. Fluoride reduces bone strength in older rats. Journal of Dental Research 1995;74:1475–1481.

27. Fry BW and Taves DR. Serum fluoride analysis with the fluoride electrode. Journal of Laboratory and Clinical Medicine 1970;75:1020–1025.

28. Posner AS, Eanes ED, Harper RA, and Zipkin I. X-ray diffraction analysis of the effect of fluoride on human bone apatite. Archives of Oral Biology 1963;8:549–570.

29. Oliver WC and Pharr GM. Improved technique for determining hardness and elastic modulus using load and displacement sensing indentation experiments. Journal of Materials Research 1992;7:1564–1583.

30. Saville PD. Water fluoridation: effect on bone fragility and skeletal calcium content in the rat. The Journal of Nutrition 1967;91:353–357.

31. Einhorn TA, Wakley GK, Linkhart S, Rush EB, Maloney S, Faierman E, and Baylink DJ. Incorporation of sodium fluoride into cortical bone does not impair the mechanical properties of the appendicular skeleton in rats. Calcified Tissue International 1992;51:127–131.

32. Riggins RS, Zeman F, and Moon D. The effects of sodium fluoride on bone breaking strength. Calcified Tissue International 1974;14:283–289.

33. Yamamoto K, Wergedal JE, and Baylink DJ. Increased bone microhardness in fluoride treated rats. Calcified Tissue International 1974;15:45–54.

34. Turner CH, Takano Y, and Hirano T. Reductions in bone strength after fluoride treatment are not reflected in tissue-level acoustic measurements. Bone 1996;19:603–607.

35. Gupta HS, Seto J, Wagermaier W, Zaslansky P, Boesecke P, and Fratzl P. Cooperative deformation of mineral and collagen in bone at the nanoscale. Proceedings of the National Academy of Sciences 2006;103:17741–17746.

36. Zipkin I and McClure FJ. Deposition of Fluorine in the Bones and Teeth of the Growing Rat Four Figures. The Journal of Nutrition 1952;47:611–620.

37. Baud CA and Bang S. Fluoride and bone mineral substance. Fluoride in medicine. Hans Huber, Bern 1970:27–36.

38. Grynpas MD. Fluoride effects on bone crystals. Journal of Bone and Mineral Research 1990;5:S169–S175.

39. Farley JR, Wergedal JE, and Baylink DJ. Fluoride directly stimulates proliferation and alkaline phosphatase activity of bone-forming cells. Science 1983;222:330.

40. Wergedal JE, Lau KHW, and Baylink DJ. Fluoride and bovine bone extract influence cell proliferation and phosphatase activities in human bone cell cultures. Clinical Orthopaedics and Related Research 1988;233:274–282.

41. Wang X, Bank RA, TeKoppele JM, Hubbard GB, Althanasiou KA, and Agrawal C. Effect of collagen denaturation on the toughness of bone. Clinical Orthopaedics and Related Research 2000;371:228.

42. Burstein AH, Zika JM, Heiple KG, and Klein L. Contribution of collagen and mineral to the elastic-plastic properties of bone. The Journal of Bone and Joint Surgery 1975;57:956.

43. Miller E, Delos D, Baldini T, Wright TM, and Pleshko Camacho N. Abnormal mineral-matrix interactions are a significant contributor to fragility in oim/oim bone. Calcified Tissue International 2007;81:206–214.

44. Silva MJ, Brodt MD, Wopenka B, Thomopoulos S, Williams D, Wassen MHM, Ko M, Kusano N, and Bank RA. Decreased collagen organization and content are associated with reduced strength of demineralized and intact bone in the SAMP6 mouse. Journal of Bone and Mineral Research 2005;21:78–88.

45. Donnelly E, Baker SP, Boskey AL, and Meulen MCH van der. Effects of surface roughness and maximum load on the mechanical properties of cancellous bone measured by nanoindentation. Journal of Biomedical Materials Research Part A 2006;77:426–435.

46. Rho JY and Pharr GM. Effects of drying on the mechanical properties of bovine femur measured by nanoindentation. Journal of Materials Science: Materials in Medicine 1999;10:485–488.

47. Hengsberger S, Kulik A, and Zysset PH. Nanoindentation discriminates the elastic properties of individual human bone lamellae under dry and physiological conditions. Bone 2002;30:178–184.

48. Bushby AJ, Ferguson VL, and Boyde A. Nanoindentation of bone: Comparison of specimens tested in liquid and embedded in polymethylmethacrylate. Journal of Materials Research 2004;19:249–259.

49. Nyman J, Roy A, Shen X, Acuna R, Tyler J, and Wang X. The influence of water removal on the strength and toughness of cortical bone. Journal of Biomechanics 2006;39:931–938.

50. Sedlin E and Hirsch C. Factors affecting the determination of the physical properties of femoral cortical bone. Acta Orthopaedica 1966;37:29–48.

51. Mechanical engineering design. In: McGraw-Hill, 1963. Chap. 2-9.

52. Boyce TM, Fyhrie DP, Glotkowski MC, Radin EL, and Schaffler MB. Damage type and strain mode associations in human compact bone bending fatigue. Journal of Orthopaedic Research 1998;16:322–329.

53. Diab T and Vashishth D. Morphology, localization and accumulation of in vivo microdamage in human cortical bone. Bone 2007;40:612–618.

54. Krishnamachari KA. Skeletal fluorosis in humans: a review of recent progress in the understanding of the disease. Progress in Food & Nutrition Science 1986;10:279.

55. Boivin G, Chavassieux P, Chapuy MC, Baud CA, and Meunier PJ. Skeletal fluorosis: histomorphometric analysis of bone changes and bone fluoride content in 29 patients. Bone 1989;10:89–99.

CHAPTER 4

REDUCED TISSUE-LEVEL STIFFNESS AND MINERALIZATION IN OSTEOPOROTIC CANCELLOUS BONE

4.1 Introduction

The skeleton is a dynamic organ with temporal and spatial variations in composition, microarchitecture, and bone mass. In the healthy skeleton, variations in microarchitecture and tissue-level properties contribute to toughness and efficient load bearing ability [1]. Metabolic bone diseases such as osteoporosis can negatively alter bone composition and architecture. Changes due to osteoporosis are of particular interest because more than 2 million fragility fractures occur in men and women annually [2]. Osteoporosis was initially characterized as a disease of reduced bone mass. However, osteoporosis is now known to not only reduce bone mass, but also change trabecular architecture, and alter bone tissue composition, ultimately making the bone more susceptible to fracture [3–5].

Areal bone mineral density (aBMD) as measured by dual-energy x-ray absorptiometry (DXA) is commonly used to assess fracture risk but has limited ability to predict fractures [6, 7]. The disconnect between fracture risk and aBMD suggests that changes at the material level, in addition to the reduction in bone mass could contribute to the increased fragility of primarily cancellous skeletal sites. A variety of compositional changes in cancellous bone have been reported previously associated with fragility-related fractures and osteoporosis. Cancellous bone biopsies from donors with previous fragility fractures had different ratios of nonreducible/reducible collagen cross-links compared with samples from donors without fractures [8] and decreased mineralization

and carbonate substitution heterogeneity [5]. Reduced bone mineralization [9], and increased carbonate substitution and crystallinity have also been associated with osteoporosis [10, 11]. The previously mentioned studies provided key information about compositional changes in bone tissue; however, none examined tissue-level mechanical properties, or the relationship between composition and material properties. In healthy and vitamin D deficient rodents, tissue composition has been related to changes in tissue-level mechanical properties [12–16]; however, a limited number of studies have looked at osteoporotic cancellous bone from humans [17, 18], a relevant application of clinical interest.

The goal of this study was to examine the effects of osteoporosis on cancellous bone composition and mechanical properties at the tissue-level length scale and correlate changes in mechanical properties with changes in tissue composition at a site prone to fracture clinically. DXA scans of the L1-L4 vertebrae were performed on spine segments from female cadavers ranging from age 58 to 92 years to determine osteoporotic status based on T-scores. Cores of trabecular bone from the T12 vertebrae were prepared for tissue-level analyses. Compositional parameters (mineral:matrix ratio, crystallinity, and B-type carbonate substitution) were measured using Raman microspectroscopy. Mechanical parameters (indentation modulus and hardness) were measured on the same cores using nanoindentation. Compositional and mechanical parameters were compared and correlated as a function of T-score.

4.2 Materials and Methods

Spine segments were obtained from 11 female donors aged from 58 to 92 years. The areal bone mineral density (aBMD) was determined from DXA scans of the L1-L4 vertebrae (n = 10) (Delphi QDR 4500A or QDR 4500W, Hologic Inc., Bedford, MA). Based on the aBMD for each sample, the associated T-score was computed [19]. The Osteoporotic group had 6 samples, all of which had T-scores of -2.5 or below. Four samples with T-scores greater than -2.5 were in the Not Osteoporotic group. The T-score for one sample could not be calculated due to a missing L1 vertebrae, this sample was still used for tissue-level measurements. After scanning, a cylindrical core (diameter = 8.25 mm) was drilled from the centrum of each T12 vertebra (n = 11). The cores were dehydrated in a series of increasing ethanol concentrations and embedded in polymethylmethacrylate (PMMA). A 3-mm thick longitudinal section was removed from the central region of each core with a diamond sectioning saw and glued onto an atomic force microscope (AFM) stub. The samples were polished anhydrously on silicon carbide polishing paper lubricated with ethylene glycol and aluminum oxide-ethylene glycol slurries until the RMS surface roughness measured by AFM (Dimension 3100 Ambient AFM, Veeco, Plainview, NY) was less than 10 nm for a 5 μm by 5 μm region [20].

For each sample, three longitudinally oriented trabeculae were chosen for both nanoindentation and Raman microspectroscopy. A scanning nanoindenter (Triboindenter, Hysitron, Minneapolis, MN) with a Berkovich tip was used. Trabecular regions with ruffled edges were avoided to preclude sites of active remodeling. Using the surface imageing capabilities of the indenter, lines of indentations were made perpendicular to the longitudinal axis of each trabec-

ulae, starting and ending 20 μm from the edges. Indentations were made at 10 μm intervals while avoiding lacunae and pores visible on the surface. This sampling method resulted in 8 indentations per trabeculae. Two loading protocols yielded different indentation depths. In 4 samples, small indents were created using a single trapezoidal load function with a maximum load of 500 μN, load/unload rates of ± 50 μN/s, and a hold time of 10 s. The remaining 7 samples were loaded twice in succession with two trapezoidal load forms with peak loads of 500 and 1000 μN, both with load rates of ± 50 μN/s and 10 s hold times. For all indents, indentation modulus (E_i) and hardness (H) values were calculated from the unloading portion of the 500 μN indent using the Oliver-Pharr method [21]. Indentation modulus and hardness values were averaged, resulting in a single indentation modulus and hardness value for each sample.

Raman spectra from 800 cm^{-1} to 1800 cm^{-1} were collected using an optical microscope (inVia, Renishaw, Gloucestershire, UK) equipped with a 785-nm laser and a 50x, 0.75 N.A. objective. The resulting spot size was $\tilde{2}$ μm. The small indents were not visible with the microscope, so the laser was positioned at approximately the same location based on optical images of the samples. The large indents were visible with the microscope and used to position the laser such that the Raman spectra were collected from the exact same location as the indent. After the background fluorescence was subtracted (WiRE V2.0, Renishaw), the spectra were smoothed using a nine point moving average, and peak heights were identified using in-house code (Matlab V7.0, The Mathworks, Inc.). Tissue mineralization was examined using the mineral-to-matrix ratio (mineral:matrix) calculated from the phosphate ν_1 (965 cm^{-1}) and CH_2 wag (1450 cm^{-1}) peak heights, respectively [22, 23]. Crystallinity was measured based on the full width at half maximum value of the phosphate ν_1 peak, with broader peaks

represent lower crystallinity [24]. B-Type carbonate substitution was calculated from the peak height ratio of the carbonate ν_1 peak ($1065cm^{-1}$) to phosphate ν_1 peak [22, 23].

Relationships between mechanical properties, composition, and age were assessed using simple and multiple linear regressions (JMP, SAS, Cary, NC). Differences in compositional and mechanical parameters between the Osteoporotic and Not Osteoporotic groups were compared using a Welch's ANOVA to account for sample size differences.

4.3 Results

Samples were divided into two groups based on T-score, Osteoporotic and Not Osteoporotic, to compare differences in tissue-level properties with osteoporotic status (Figure 4.1). The average age of the osteoporotic group (79.7 ± 11 yrs) was higher than the Not Osteoporotic group (66.5 ± 8 yrs) (p = 0.064). The Osteoporotic group had a 14% lower indentation modulus (p = 0.029) and 21% lower mineral:matrix ratio (p = 0.046) than the Not Osteoporotic group. Hardness was not different between the two groups (p = 0.623).

Relationships between tissue-level composition and material properties were examined using simple and multiple linear regressions (Table 4.1). The indentation modulus increased with rising mineral:matrix ratio (r^2 = 0.47, p= 0.02) but hardness did not (Figure 4.2, Table 4.1). Though crystallinity and carbonate substitution were not significant predictors of either nanoindentation outcome individually, crystallinity in addition to the mineral:matrix ratio concurrently explained 56% of the variability in indentation modulus (R^2 = 0.56,

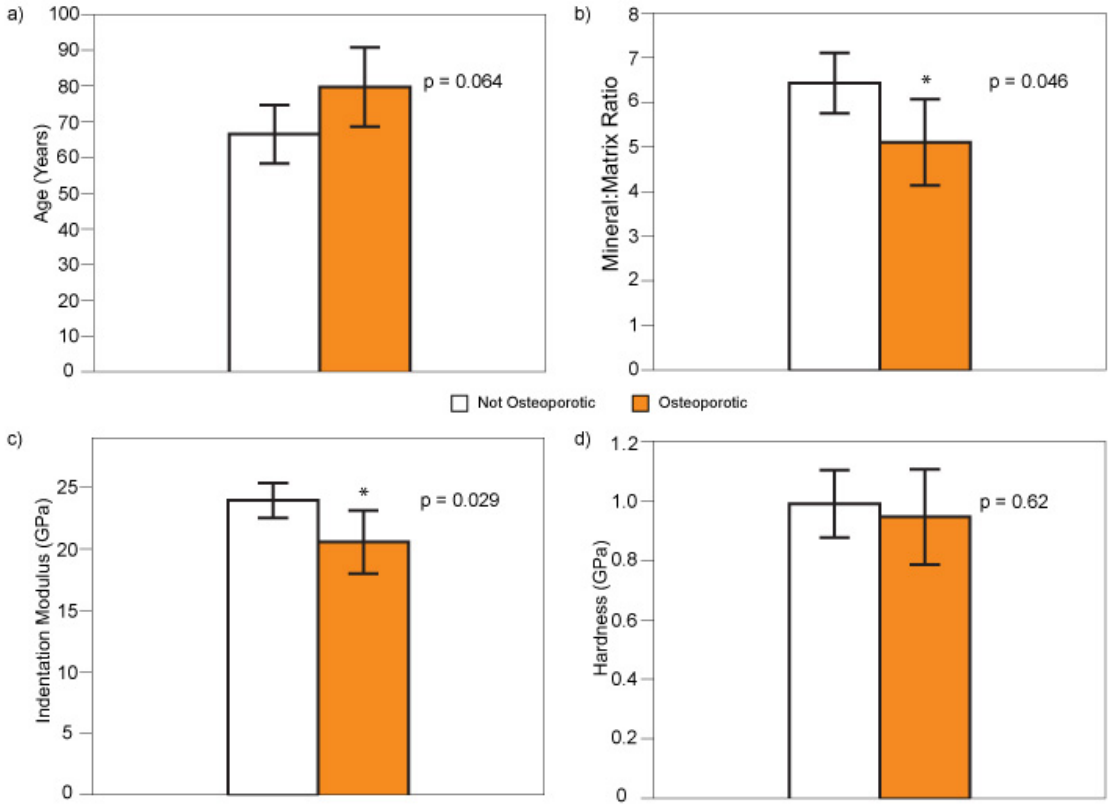

Figure 4.1: a) Age, b) mineral:matrix ratio, c) indentation modulus, d) hardness for the Not Osteoporotic and Osteoporotic groups. Data are presented as mean ± standard deviation. ∗ indicates different from Not Osteoporotic, $p \leq 0.05$

p = 0.02) (Table 4.2). Carbonate substitution in addition to the mineral:matrix ratio explained 38% of the variability in hardness but was still not significant (R^2 = 0.38, p = 0.06) (Table 4.2). Combining all three compositional metrics did not improve the prediction of indentation modulus compared with crystallinity and mineral:matrix ratio.

Changes in age and aBMD with tissue-level parameters were investigated using simple linear regressions. The only tissue-level measurement that varied with donor age was tissue mineralization as measured by Raman spectroscopy,

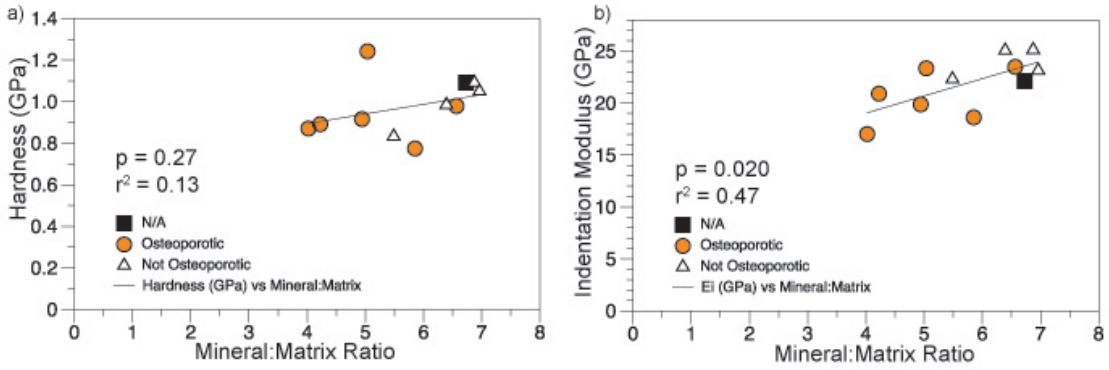

Figure 4.2: Linear regressions of a) indentation modulus and b) hardness with tissue mineralization. Changes in hardness were not associated with changes in the mineral:matrix ratio, the indentation modulus increased with increasing mineralization.

Table 4.1: Correlation coefficients, coefficients of determination, and p-values for multiple linear regressions of tissue-level properties and aBMD

Dependent Variable	Independent Variable	R^2	p
E_i	Mineral:Matrix, Crystallinity	0.56	0.015
H	Mineral:Matrix, Carbonate Substitution	0.38	0.062

Table 4.2: Adjusted coefficients of determination and associated p-values for simple linear regressions to predict tissue-level mechanical properties.

Predictor	Response	r	r^2	p
Mineral:Matrix	Age	-0.60	0.35	0.053
E_i (GPa)	BMD L1-L4	0.64	0.41	0.044
E_i (GPa)	Mineral:Matrix	0.69	0.47	0.020
H (GPa)	Mineral:Matrix	0.36	0.13	0.27
H (GPa)	E_i	0.63	0.40	0.036

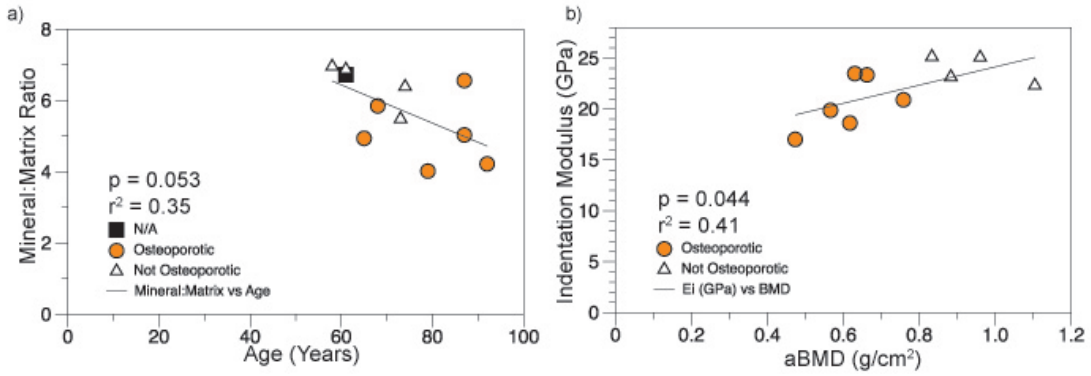

Figure 4.3: Linear regression of tissue-level mineralization as measured by Raman spectroscopy with age. Linear regression of the indentation modulus with mineralization as measured by DXA.

which decreased with age (r^2 = 0.35, p = 0.05) (Figure 4.3). Crystallinity, carbonate substitution, indentation modulus, and indentation hardness were not associated with age. Finally, relationships between tissue-level outcome measures and aBMD were investigated using simple linear regressions. The indentation modulus increased with rising aBMD (r^2 = 0.41, p=0.04) (Figure 4.3). No other tissue-level outcome measures varied with aBMD.

4.4 Discussion

The two goals of this study were to (1) investigate changes in tissue-level composition and mechanical properties with osteoporosis and (2) determine the relationship between composition and tissue-level mechanical properties in human cancellous bone from a clinically relevant fracture site. Osteoporotic status was based on T-scores from DXA scans, and tissue-level analyses were performed on samples from the same vertebrae as those scanned using DXA. The T12 vertebra was chosen for material property analysis, as osteoporotic verte-

bral fractures often occur in the lower thoracic and upper lumbar spine regions [25, 26]. The indentation modulus and mineral:matrix ratio of the Osteoporotic group were reduced compared to the Not Osteoporotic group. In relating compositional measures with mechanical properties, the mineral:matrix ratio best predicted both the indentation modulus and hardness, and the addition of other compositional measures, crystallinity and B-type carbonate substitution, improved the prediction for the indentation modulus and hardness, respectively.

In the current study, samples from osteoporotic individuals had lower tissue indentation modulus and reduced mineralization than samples from normal and osteopenic donors (T-scores larger than -2.5). Previous studies have reported nanoindentation outcomes to be insensitive to fragility fracture [17] and menopause [18]. However, these studies examined cancellous bone samples from the iliac crest, and osteoporosis was not confirmed in any of the donors post-menopause. Previously, carbonate substitution was found to be higher in cancellous bone from donors who had a fragility fracture compared to age-matched samples without fragility fractures [11], but the mechanical properties were not measured. Compositional changes would likely alter tissue-level mechanical properties as correlations between composition and mechanical properties have been previously demonstrated in rodent tissue [12, 13, 15, 27].

The change in material properties with osteoporosis found in the current study suggests the importance of anatomic location-specific changes in bone tissue due to osteoporosis. However results vary even for compositional variation across skeletal sites in healthy bone [28]. Though bone mineral density distributions may be similar, the composition of the organic matrix may not be uniform across skeletal sites [29, 30]. Cancellous bone mineralization mea-

surements from iliac crest samples were poor predictors of vertebral strength indicating that the composition of cancellous bone is location specific [31]. Furthermore, osteoporosis may cause region-specific compositional changes. The more sites with low bone mass an individual has, the larger their fracture risk becomes [32]. By the time a person experiences a fragility fracture, aBMD along with other compositional parameters may be altered in the majority of cancellous locations. Thus, sites not usually susceptible to fracture, such as the iliac crest, have measureable differences in composition.

One limitation of this study was that osteoporotic status was determined solely from aBMD as measured by DXA, which does not always predict fracture [33, 34]. In despite of this, aBMD is a clinically relevant and widely used criterion for diagnosing osteoporosis. Another limitation was that collagen cross-linking data was not computed from the Raman spectra due to overlapping peaks from the embedding medium. Collagen cross-linking has been related to the tissue-level mechanical properties of bone [35, 36] and osteoporosis alters cross-linking ratios [8, 37]. Choosing a different embedding medium or using FTIR instead of Raman spectroscopy would allow the assessment of collagen maturity through cross-linking ratios and could improve predictions for mechanical properties. Another limitation of this study was that a relatively small volume of tissue was examined for the tissue properties due to the time-intensive nature of data collection. To ensure that the sites selected for tissue-level analyses were representative of the majority of the tissue, care was taken to avoid trabeculae with scalloped surfaces indicative of active remodeling.

This study is the first to examine osteoporotic cancellous bone composition and mechanical properties from a site prone to osteoporotic fracture. The in-

dentation modulus was reduced in osteoporotic human cancellous bone from a lower thoracic vertebra. The reduced indentation modulus coincided with decreased mineralization and increased crystallinity and carbonate substitution. Whole bone strength depends on bone mass, architecture and material properties. Bone volume fraction, as measured by micro-computed tomography scans predicts 73-97% of the ultimate stress and Young's Modulus of vertebral cancellous bone [38–40]. Because material properties are independent of bone mass and architecture metrics, the differences in material properties between osteoporotic and non-osteoporotic bone tissue could contribute to the remaining 3-27% of the variability in apparent level strength and stiffness. Future work examining cancellous architecture and apparent level mechanical properties concurrently with tissue-level properties will provide a complete quantitative assessment of the influence of material properties on apparent level mechanical properties.

References

1. Tai K, Dao M, Suresh S, Palazoglu A, and Ortiz C. Nanoscale heterogeneity promotes energy dissipation in bone. Nature Materials 2007;6:454–462.

2. Burge R, Dawson-Hughes B, Solomon DH, Wong JB, King A, and Tosteson A. Incidence and Economic Burden of Osteoporosis-Related Fractures in the United States, 2005–2025. Journal of Bone and Mineral Research 2006;22:465–475.

3. Boutroy S, Bouxsein ML, Munoz F, and Delmas PD. In vivo assessment of trabecular bone microarchitecture by high-resolution peripheral quantitative computed tomography. Journal of Clinical Endocrinology & Metabolism 2005;90:6508–6515.

4. Legrand E, Chappard D, Pascaretti C, Duquenne M, Krebs S, Rohmer V, Basle MF, and Audran M. Trabecular bone microarchitecture, bone mineral density, and vertebral fractures in male osteoporosis. Journal of Bone and Mineral Research 2000;15:13–19.

5. Gourion-Arsiquaud S, Lukashova L, Power J, Loveridge N, Reeve J, and Boskey AL. Fourier transformed infra-red imaging of femoral neck bone: Reduced heterogeneity of mineral-to-matrix and carbonate-to-phosphate and more variable crystallinity in treatment-naïve fracture cases compared to fracture-free controls. Journal of Bone and Mineral Research 2012.

6. Marshall D, Johnell O, and Wedel H. Meta-analysis of how well measures of bone mineral density predict occurrence of osteoporotic fractures. British Medical Journal 1996;312:1254–1259.

7. Miller PD, Siris ES, Barrett-Connor E, Faulkner KG, Wehren LE, Abbott TA, Chen YT, Berger ML, Santora AC, and Sherwood LM. Prediction of fracture

risk in postmenopausal white women with peripheral bone densitometry: evidence from the National Osteoporosis Risk Assessment. Journal of Bone and Mineral Research 2002;17:2222–2230.

8. Gourion-Arsiquaud S, Faibish D, Myers E, Spevak L, Compston J, Hodsman A, Shane E, Recker RR, Boskey ER, and Boskey AL. Use of FTIR spectroscopic imaging to identify parameters associated with fragility fracture. Journal of Bone and Mineral Research 2009;24:1565–1571.

9. Boivin GY, Chavassieux PM, Santora AC, Yates J, and Meunier PJ. Alendronate increases bone strength by increasing the mean degree of mineralization of bone tissue in osteoporotic women. Bone 2000;27:687–694.

10. Boskey AL, DiCarlo E, Paschalis E, West P, and Mendelsohn R. Comparison of mineral quality and quantity in iliac crest biopsies from high-and low-turnover osteoporosis: an FT-IR microspectroscopic investigation. Osteoporosis International 2005;16:2031–2038.

11. McCreadie BR, Morris MD, Chen T, Sudhaker Rao D, Finney WF, Widjaja E, and Goldstein SA. Bone tissue compositional differences in women with and without osteoporotic fracture. Bone 2006;39:1190–1195.

12. Busa B, Miller L, Rubin C, Qin YX, and Judex S. Rapid establishment of chemical and mechanical properties during lamellar bone formation. Calcified Tissue International 2005;77:386–394.

13. Miller LM, Little W, Schirmer A, Sheik F, Busa B, and Judex S. Accretion of bone quantity and quality in the developing mouse skeleton. Journal of Bone and Mineral Research 2007;22:1037–1045.

14. Donnelly E, Chen DX, Boskey AL, Baker SP, and Meulen MCH van der. Contribution of mineral to bone structural behavior and tissue mechanical properties. Calcified Tissue International 2010:1–11.

15. Burket J, Gourion-Arsiquaud S, Havill LM, Baker SP, Boskey AL, and Meulen MCH Van der. Microstructure and nanomechanical properties in osteons relate to tissue and animal age. Journal of Biomechanics 2011;44:277–284.

16. Kim G, Boskey AL, Baker SP, and Meulen MCH van der. Improved prediction of rat cortical bone mechanical behavior using composite beam theory to integrate tissue level properties. Journal of Biomechanics 2012.

17. Wang X, Sudhaker Rao D, Ajdelsztajn L, Ciarelli TE, Lavernia EJ, and Fyhrie DP. Human iliac crest cancellous bone elastic modulus and hardness differ with bone formation rate per bone surface but not by existence of prevalent vertebral fracture. Journal of Biomedical Materials Research Part B: Applied Biomaterials 2008;85:68–77.

18. Polly BJ, Yuya PA, Akhter MP, Recker RR, and Turner JA. Intrinsic Material Properties of Trabecular Bone by Nanoindentation Testing of Biopsies Taken from Healthy Women Before and After Menopause. Calcified Tissue International 2012:1–8.

19. Kanis JA, Melton III LJ, Christiansen C, Johnston CC, and Khaltaev N. The diagnosis of osteoporosis. Journal of Bone and Mineral Research 1994;9:1137–1141.

20. Donnelly E, Williams RM, Downs SA, Dickinson ME, Baker SP, and Meulen MCH van der. Quasistatic and dynamic nanomechanical proper-

ties of cancellous bone tissue relate to collagen content and organization. Journal of Materials Research 2006;21:2106–2117.

21. Oliver WC and Pharr GM. Improved technique for determining hardness and elastic modulus using load and displacement sensing indentation experiments. Journal of Materials Research 1992;7:1564–1583.

22. Draper ERC, Morris MD, Camacho NP, Matousek P, Towrie M, Parker AW, and Goodship AE. Novel Assessment of Bone Using Time-Resolved Transcutaneous Raman Spectroscopy. Journal of Bone and Mineral Research 2005;20:1968–1972.

23. Timlin JA, Carden A, Morris MD, Bonadio JF, Hoffler CE, Kozloff KM, and Goldstein SA. Spatial distribution of phosphate species in mature and newly generated mammalian bone by hyperspectral Raman imaging. Journal of Biomedical Optics 1999;4:28–34.

24. Freeman JJ, Wopenka B, Silva MJ, and Pasteris JD. Raman spectroscopic detection of changes in bioapatite in mouse femora as a function of age and in vitro fluoride treatment. Calcified Tissue International 2001;68:156–162.

25. Johansson C, MellstrÖm D, Rosengren K, and Rundgren. A community-based population study of vertebral fractures in 85-year-old men and women. Age and Ageing 1994;23:388–392.

26. Black DM, Cummings SR, Stone K, Hudes E, Palermo L, and Steiger P. A new approach to defining normal vertebral dimensions. Journal of Bone and Mineral Research 1991;6:883–892.

27. Donnelly E, Boskey AL, Baker SP, and Meulen MCH Van der. Effects of tissue age on bone tissue material composition and nanomechanical prop-

erties in the rat cortex. Journal of Biomedical Materials Research Part A 2010;92:1048–1056.

28. Donnelly E, Meredith DS, Nguyen JT, and Boskey AL. Bone tissue composition varies across anatomic sites in the proximal femur and the iliac crest. Journal of Orthopaedic Research 2012.

29. Roschger P, Gupta H, Berzlanovich A, Ittner G, Dempster D, Fratzl P, Cosman F, Parisien M, Lindsay R, Nieves J, et al. Constant mineralization density distribution in cancellous human bone. Bone 2003;32:316–323.

30. Aerssens J, Boonen S, Joly J, and Dequeker J. Variations in trabecular bone composition with anatomical site and age: potential implications for bone quality assessment. Journal of Endocrinology 1997;155:411–421.

31. Chalmers J and Weaver JK. Cancellous Bone: Its Strength and Changes with Aging and an Evaluation of Some Methods for Measuring Its Mineral Content II. An evaluation of some methods for measuring osteoporosis. The Journal of Bone & Joint Surgery 1966;48:299–308.

32. Davis JW, Ross PD, and Wasnich RD. Evidence for both generalized and regional low bone mass among elderly women. Journal of Bone and Mineral Research 1994;9:305–309.

33. Cummings SR, Karpf DB, Harris F, Genant HK, Ensrud K, LaCroix AZ, and Black DM. Improvement in spine bone density and reduction in risk of vertebral fractures during treatment with antiresorptive drugs. The American Journal of Medicine 2002;112:281–289.

34. Riggs BL, Wahner HW, Dunn WL, Mazess RB, Offord KP, and Melton LJ. Differential changes in bone mineral density of the appendicular and axial

skeleton with aging: relationship to spinal osteoporosis. Journal of Clinical Investigation 1981;67:328.

35. Carden A, Rajachar RM, Morris MD, and Kohn DH. Ultrastructural changes accompanying the mechanical deformation of bone tissue: a Raman imaging study. Calcified Tissue International 2003;72:166–175.

36. Vashishth D, Gibson GJ, Khoury JI, Schaffler MB, Kimura J, and Fyhrie DP. Influence of nonenzymatic glycation on biomechanical properties of cortical bone. Bone 2001;28:195–201.

37. Saito M and Marumo K. Collagen cross-links as a determinant of bone quality: a possible explanation for bone fragility in aging, osteoporosis, and diabetes mellitus. Osteoporosis International 2010;21:195–214.

38. Nazarian A, Stechow D von, Zurakowski D, Müller R, and Snyder BD. Bone volume fraction explains the variation in strength and stiffness of cancellous bone affected by metastatic cancer and osteoporosis. Calcified Tissue International 2008;83:368–379.

39. Homminga J, Mccreadie BR, Weinans H, and Huiskes R. The dependence of the elastic properties of osteoporotic cancellous bone on volume fraction and fabric. Journal of Biomechanics 2003;36:1461–1467.

40. Morgan EF, Bayraktar HH, and Keaveny TM. Trabecular bone modulus–density relationships depend on anatomic site. Journal of Biomechanics 2003;36:897–904.

CHAPTER 5

SUMMARY AND FUTURE DIRECTIONS

5.1 Summary

Osteoporosis compromises the mechanical integrity of bone, leading to reduced bone strength and increased fracture risk. From an engineering standpoint, whole bone strength depends on the bone mass, geometry, and material properties of the bone tissue. In addition to the detrimental changes in bone mass and geometry, osteoporosis also alters bone composition [1–3]. Changes in tissue composition are thought to reflect changes in bone mechanical properties, however, few studies examining compositional changes with osteoporosis have simultaneously investigated mechanical properties. Furthermore, few studies that use nanoindentation relate tissue-level measures to whole bone mechanical behavior. Thus the objectives of this work were first to determine the effects of two specific compositional changes that are associated with aging and osteoporosis, mineralization and crystallinity, and second, examine osteoporosis related changes in tissue-level composition and mechanical properties of human cancellous bone.

To investigate individual compositional changes, two different in vivo models were used. First vitamin D deficiency in growing rats was used to reduce cortical bone tissue mineralization. Whole bone mechanical behavior as indicated by the failure moment and bending stiffness were lower in vitamin D deficient animals. Mineralization, cortical cross-sectional area, and moment of inertia as measured by microCT, were also reduced in the vitamin D deficient groups. For tissue-level measures, the indentation modulus and hardness,

as measured by nanoindentation, increased with tissue age and mineralization measured by Raman spectroscopy. Correlations between mechanical behavior and mineralization at the tissue and whole bone levels were present. However, average tissue-level mechanical properties did not correlate with whole bone mechanical behavior. To take into account the heterogeneity in mineralization throughout the cortex, this study used nanoindentation-derived material properties and composite beam theory to calculate a density weighted section modulus. The section moduli calculated using composite beam theory incorporate geometric and tissue-level properties and ultimately improved the predictions for measures of whole bone mechanical behavior compared to average mechanical properties. Although FEA predicts whole bone mechanical behavior very well (70-89% of the variability in failure load [4, 5]), the method proposed in this study that uses composite beam theory predicted 80% of the variability in failure moment while using far less computational power and time.

Altered crystallinity of bone tissue has been reported in diseases such as osteoporosis and osteogenesis imperfecta, both of which are known to reduce whole bone strength [1, 6]. To isolate the effects of crystallinity on whole bone mechanical behavior, growing rodents were given fluoride to increase mineral crystallinity with minimal changes to other compositional parameters. Crystallinity was measured by XRD and increased in fluoride-treated animals. Measures of whole bone mechanical behavior were lower in fluoride treated animals with no associated changes in cross-sectional geometry or mineralization based on microCT scans. The lack of correlation between cortical geometry and whole bone mechanical behavior suggested a difference in tissue-level mechanical properties were responsible for the reduced bending stiffness and failure moment of the fluoride treated animals. At the tissue-level, indentation modu-

lus and hardness from nanoindentation were not different with fluoride treatment, thus whole bone mechanical behavior and nanoindentation parameters were not correlated. The discrepancies between tissue-level and whole bone mechanical behavior could indicate that interfaces between microstructural features are contributors to whole bone mechanical behavior or that the mechanical behavior of bone is sensitive to the specific loading mode and stress state of the tissue.

The third portion of this research involved a more clinically oriented question. Previously, studies found tissue-level properties were not different in donors with fragility fractures or post menopause [7, 8]; however, tissue was examined from the iliac crest, a skeletal site not prone to osteoporotic fractures. Thus in the third study, tissue-level composition and mechanical properties of human vertebral cancellous from a fracture prone location bone were examined. Donors were divided into two groups, osteoporotic and not osteoporotic, based on T-scores from DXA scans. Samples with T-scores below -2.5 were considered osteoporotic and samples with T-scores greater than -2.5 were considered not osteoporotic. The indentation modulus was lower in samples from individuals with osteoporosis, and mineralization trended towards being lower compared with samples from normal/osteopenic individuals. Similar to previous studies examining tissue-level composition and mechanical properties, the tissue-level mechanical properties were correlated with spectroscopic measures of composition [9–11]. Although this study did not test apparent or whole bone level mechanical behavior, the reduced indentation modulus of osteoporotic samples could contribute to the well-documented increased fragility of cancellous bone in osteoporotic individuals.

The first two studies presented in this body of work used animal models to examine the effect of individual compositional changes that have been associated with osteoporosis and aging, mineralization and crystallinity. Reduced mineralization and increased crystallinity are fundamentally different changes to the mineral phase of bone tissue, but both profoundly reduced measures of whole bone mechanical behavior thus underlining the importance of composition when optimizing therapies for osteoporosis. Despite bone's hierarchical nature, the majority of studies investigating composition and mechanical behavior have only focused on a single length scale. The two animal studies simultaneously examined whole bone and tissue-level mechanical behavior of bone. In the case of altered mineralization, microCT scans and composite beam theory were used to take into account the effects of heterogeneous mineralization when predicting whole bone mechanical behavior.

To our knowledge the third study is the first to investigate tissue-level properties of osteoporotic cancellous bone from a fracture prone location. The indentation modulus was lower in the osteoporotic group and correlated with changes in mineralization and crystallinity. The differences in tissue-level mechanical behavior could contribute to the changes reported in apparent level strength and stiffness of osteoporotic cancellous bone independent of bone mass and trabecular architecture. Future studies that test length scales in between nanoindentation and whole bone could further clarify the role of microstructural features and interfaces on whole bone mechanical performance. Furthermore, the contribution of changes to the organic phase of bone tissue could be performed using similar experimental techniques in animal models.

5.2 Future Directions

There are several future directions based on results of the three studies presented within. The future directions can be divided roughly into three categories: additional characterization techniques, other perturbations to the mineral phase, and assessment of the contribution of collagen to tissue-level mechanical properties. Including the contribution of microstructure in conjunction with nanomechanical properties will improve the understanding of whole bone mechanical behavior. Carbonate substitution, another compositional change pertaining to the mineral can be altered in vitro by exposing tissue to carbon dioxide rich environments and studied using the same techniques used in the presented studies. Finally the influence of the collagen phase can be investigated using in vitro methods.

First, the source of differences between nanoindentation and apparent level derived mechanical properties need to be determined. Just as finite element analysis (FEA) was used to determine reasons for the discrepancies between apparent level and whole bone derived moduli [12], finite element analysis could elucidate sources of differences between nanoindentation and apparent level mechanical properties. Micron-length-scale resolution microCT scans of microbeam samples could be used to generate FEA models that can account for pores, lacunae, and blood vessels. However, this approach cannot account for changes in modulus due to sample dehydration and embedding required for high resolution nanoindentation.

Dehydration and embedding of cortical and cancellous bone samples are required to achieve adequately large contact depth to surface roughness ratios for

nanoindentation [13]. Dehydration alters whole bone mechanical properties, increasing the strength and decreasing toughness [14, 15]. Dehydration also increases the indentation modulus and hardness as measured by nanoindentation [16–18], but relative differences in properties between different microstructures are still distinguishable. Although the exact mechanisms through which hydration influences mechanical properties are not well understood, water has been found in key locations within bone matrix. Water occupies vacancies in the hydroxyapatite lattice and likely stabilizes the lattice, water molecules on the surface of mineral crystals likely affect interactions of the crystals with collagen and other proteins [19]. Thus removing the water from bone tissue likely changes the behavior of individual crystals and mineral-organic interfaces. Larger load transducers for nanoindenters or devices such as the BioDent can apply loads on the order of 10 N to the sample, more than 1000 times larger than the indentations used in the current set of studies [20]. Larger loads would create larger indents with larger contact depths, increasing the acceptable surface roughness thus negating the necessity for dehydrating and embedding samples. At the expense of spatial resolution, the bone tissue may be able to respond in a manner more representative of in vivo behavior.

The importance of the collagen-mineral and collagen-extrafibrillar matrix interfaces have also been suggested as an important contributor to the mechanical behavior of this natural composite material [6, 21]. Previously, the dependence of Young's modulus on crystal width was demonstrated using molecular dynamic modeling [22]. Mineral crystal size is one factor of mineral crystallinity in addition to crystal perfection and lattice strains. Molecular dynamic modeling could provide mechanistic answers to how individual aspects of crystallinity, lattice strain and substitutions, alter the elastic behavior of bone.

Another method of examining the mechanical behavior of bone tissue below the apparent level is by using wide and small angle x-ray scattering during uniaxial tension tests. Despite the relative unavailability of systems that can simultaneous monitor loading and wide and small angle x-ray scattering, the ability of these systems to provide insights about the multi-scale deformation of bone tissue cannot be ignored. Previously intrafibrillar and mineral strain were measured individually during uniaxial tension tests, the majority of tissue strain was accounted for by intrafibrillar strain rather than mineral strain emphasizing the importance of the interface between the mineral and extrafibrillar matrix [21]. This mechanical loading and x-ray scattering setup could provide insight regarding the effects of compositional changes on mineral-organic interfaces and corresponding effects on the elastic behavior of bone tissue in a hydrated environment. Although only normal bovine cortical bone has been examined using this technique, this experimental setup could also determine the effects of aging and diseases such as osteoporosis, osteogenesis imperfecta, and osteopetrosis, on mineral-organic interfaces.

Beyond additional experimental techniques, another physiologically relevant compositional perturbation to the mineral phase could be examined. Carbonate substitution increases with age [1, 2] and nanomechanical properties have been correlated with carbonate substitution [10] [11]. However because of concomitant changes in mineralization with tissue age, it is difficult to isolate the effect of carbonate substitution. Thus establishing the composition-mechanical behavior relationship for carbonate substitution would be insightful. Independently examining the effect of carbonate substitution on tissue mechanical properties experimentally could complement and validate computation modeling. Unlike mineralization and crystallinity, no simple dietary inter-

vention exists to alter primarily carbonate substitution in vivo. In vitro, synthetic hydroxyapatite can be exposed to a heated carbon dioxide environment [23], or soaked in an aqueous solution saturated with carbon dioxide [24] to alter carbonate substitution, however these methods also affect crystallinity. Presumably a similar process can alter the carbonate substitution of bone. Once altered, the same multiscale testing techniques presented in this thesis can be used to investigate tissue-level and whole bone effects of carbonate substitution.

The studies presented in this thesis focused only on changes to the mineral phase. However collagen is the second most abundant constituent of bone and collagen's role is evident at the apparent level, affecting bone strength and toughness [25, 26]. In vivo rodent models of osteogenesis imperfecta have altered collagen molecules and result in changes to the mechanical behavior bone [27, 28]. However because of the crucial role the collagen matrix has in mineralization, oim mice have associated changes to the mineral phase in addition to the collagen defects making it difficult to isolate the contributions of just the collagen.

Because of the coupling between collagen and the mineralization process, in vitro modifications of bone such as enzymatic digestion, heat denaturation, or gamma irradiation [25, 26, 29] could explore the contribution of the collagen on tissue mechanical properties in a more controlled environment. Once samples are modified using any of the mentioned in vitro methods, samples could be dehydrated and embedded for high spatial resolution nanoindentation, or simply polished and tested hydrated using larger loads as suggested above. Since collagen content does not affect the Young's modulus at the apparent level, the major differences would be expected in the hardness rather than the indentation

modulus.

References

1. Boskey AL, DiCarlo E, Paschalis E, West P, and Mendelsohn R. Comparison of mineral quality and quantity in iliac crest biopsies from high-and low-turnover osteoporosis: an FT-IR microspectroscopic investigation. Osteoporosis International 2005;16:2031–2038.

2. McCreadie BR, Morris MD, Chen T, Sudhaker Rao D, Finney WF, Widjaja E, and Goldstein SA. Bone tissue compositional differences in women with and without osteoporotic fracture. Bone 2006;39:1190–1195.

3. Gourion-Arsiquaud S, Lukashova L, Power J, Loveridge N, Reeve J, and Boskey AL. Fourier transformed infra-red imaging of femoral neck bone: Reduced heterogeneity of mineral-to-matrix and carbonate-to-phosphate and more variable crystallinity in treatment-naïve fracture cases compared to fracture-free controls. Journal of Bone and Mineral Research 2012.

4. Imai K, Ohnishi I, Yamamoto S, and Nakamura K. In vivo assessment of lumbar vertebral strength in elderly women using computed tomography-based nonlinear finite element model. Spine 2008;33:27–32.

5. Pistoia W, Van Rietbergen B, Lochmüller EM, Lill CA, Eckstein F, and Rüegsegger P. Estimation of distal radius failure load with micro-finite element analysis models based on three-dimensional peripheral quantitative computed tomography images. Bone 2002;30:842–848.

6. Landis WJ. The strength of a calcified tissue depends in part on the molecular structure and organization of its constituent mineral crystals in their organic matrix. Bone 1995;16:533–544.

7. Polly BJ, Yuya PA, Akhter MP, Recker RR, and Turner JA. Intrinsic Material Properties of Trabecular Bone by Nanoindentation Testing of Biopsies

Taken from Healthy Women Before and After Menopause. Calcified Tissue International 2012:1–8.

8. Wang X, Sudhaker Rao D, Ajdelsztajn L, Ciarelli TE, Lavernia EJ, and Fyhrie DP. Human iliac crest cancellous bone elastic modulus and hardness differ with bone formation rate per bone surface but not by existence of prevalent vertebral fracture. Journal of Biomedical Materials Research Part B: Applied Biomaterials 2008;85:68–77.

9. Miller LM, Little W, Schirmer A, Sheik F, Busa B, and Judex S. Accretion of bone quantity and quality in the developing mouse skeleton. Journal of Bone and Mineral Research 2007;22:1037–1045.

10. Busa B, Miller L, Rubin C, Qin YX, and Judex S. Rapid establishment of chemical and mechanical properties during lamellar bone formation. Calcified Tissue International 2005;77:386–394.

11. Donnelly E, Boskey AL, Baker SP, and Meulen MCH Van der. Effects of tissue age on bone tissue material composition and nanomechanical properties in the rat cortex. Journal of Biomedical Materials Research Part A 2010;92:1048–1056.

12. Lenthe GH van, Voide R, Boyd SK, and Müller R. Tissue modulus calculated from beam theory is biased by bone size and geometry: implications for the use of three-point bending tests to determine bone tissue modulus. Bone 2008;43:717–723.

13. Donnelly E, Baker SP, Boskey AL, and Meulen MCH van der. Effects of surface roughness and maximum load on the mechanical properties of cancellous bone measured by nanoindentation. Journal of Biomedical Materials Research Part A 2006;77:426–435.

14. Sedlin E and Hirsch C. Factors affecting the determination of the physical properties of femoral cortical bone. Acta Orthopaedica 1966;37:29–48.

15. Nyman J, Roy A, Shen X, Acuna R, Tyler J, and Wang X. The influence of water removal on the strength and toughness of cortical bone. Journal of Biomechanics 2006;39:931–938.

16. Rho JY and Pharr GM. Effects of drying on the mechanical properties of bovine femur measured by nanoindentation. Journal of Materials Science: Materials in Medicine 1999;10:485–488.

17. Hengsberger S, Kulik A, and Zysset PH. Nanoindentation discriminates the elastic properties of individual human bone lamellae under dry and physiological conditions. Bone 2002;30:178–184.

18. Bushby AJ, Ferguson VL, and Boyde A. Nanoindentation of bone: Comparison of specimens tested in liquid and embedded in polymethylmethacrylate. Journal of Materials Research 2004;19:249–259.

19. Wilson E, Awonusi A, Morris M, Kohn D, Tecklenburg M, and Beck L. Three structural roles for water in bone observed by solid-state NMR. Biophysical Journal 2006;90:3722–3731.

20. Diez-Perez A, Güerri R, Nogues X, Cáceres E, Peña MJ, Mellibovsky L, Randall C, Bridges D, Weaver JC, Proctor Alexander BDKKJRRO, and Hansma PK. Microindentation for in vivo measurement of bone tissue mechanical properties in humans. Journal of Bone and Mineral Research 2010;25:1877–1885.

21. Gupta HS, Seto J, Wagermaier W, Zaslansky P, Boesecke P, and Fratzl P. Cooperative deformation of mineral and collagen in bone at the nanoscale. Proceedings of the National Academy of Sciences 2006;103:17741–17746.

22. Qin Z, Gautieri A, Nair AK, Inbar H, and Buehler MJ. Thickness of Hydroxyapatite Nanocrystal Controls Mechanical Properties of the Collagen–Hydroxyapatite Interface. Langmuir 2012;28:1982–1992.

23. Gibson I and Bonfield W. Novel synthesis and characterization of an AB-type carbonate-substituted hydroxyapatite. Journal of Biomedical Materials Research 2001;59:697–708.

24. Nordström EG and Karlsson KH. Carbonate-doped hydroxyapatite. Journal of Materials Science: Materials in Medicine 1990;1:182–184.

25. Wang X, Bank RA, TeKoppele JM, Hubbard GB, Althanasiou KA, and Agrawal C. Effect of collagen denaturation on the toughness of bone. Clinical Orthopaedics and Related Research 2000;371:228.

26. Wang X, Bank RA, Tekoppele JM, and Agrawal C. The role of collagen in determining bone mechanical properties. Journal of Orthopaedic Research 2006;19:1021–1026.

27. Miller E, Delos D, Baldini T, Wright TM, and Pleshko Camacho N. Abnormal mineral-matrix interactions are a significant contributor to fragility in oim/oim bone. Calcified Tissue International 2007;81:206–214.

28. Camacho NP, Hou L, Toledano TR, Ilg WA, Brayton CF, Raggio CL, Root L, and Boskey AL. The material basis for reduced mechanical properties in oim mice bones. Journal of Bone and Mineral Research 1999;14:264–272.

29. Akkus O, Belaney RM, and Das P. Free radical scavenging alleviates the biomechanical impairment of gamma radiation sterilized bone tissue. Journal of Orthopaedic Research 2005;23:838–845.

CHAPTER 6

APPENDIX A: CHAPTER 2 DATA

Table 6.1: Whole bone mechanical testing (3 point bending) and microCT data for the femurs of rats used in the study in Chapter 2.

General Info					3pt bend output		MicroView	
Group	**Scan #**	**Scan part**	**Animal#**	**Femur Length**	**EI(Nmm^2)**	**Mfail**	**TMC (mg)**	**TMD (mg/cc)**
Diet 1	434	2	D1,1 NP	38.75	13043	453.0	16.19	799.89
Control	434	4	C1 P	41.06	10014	479.2	23.94	877.63
Control	435	1	C2 NP	39.64	20541	713.8	22.33	933.78
Diet 2	435	2	D2,2 P	37.08	12603	477.6	16.91	832.42
Control	435	4	C2 P	39.21	15761	618.2	22.26	916.21
Control	436	1	C3 NP	40.75	13307	731.5	23.00	923.03
Diet 1	436	2	D1,2 NP	40.22	12367	595.4	20.49	881.86
Diet 2	436	3	D2,2 NP	38.49	9596	363.6	15.98	789.73
Control	436	4	C4 NP	39.13	23170	705.3	23.96	968.43
Diet 1	437	1	D1,4 NP	36.83	8865	417.4	16.14	839.62
Diet 1	437	2	D1,5 NP	38.26	13494	484.4	16.35	863.55
Diet 2	437	3	D2,3 NP	37.56	11777	468.1	17.58	864.51
Diet 2	438	2	D2,5 NP	38.97	16642	539.6	19.02	793.11
Diet 1	438	3	D1,2 P	37.1	7687	435.3	14.93	821.47
Diet 1	438	4	D1,3 P	39.11	10942	Sample slip	20.05	882.45
Control	441	1	C6 P	40.33	22852	816.4	26.20	958.56
Diet 1	441	2	D1,6 NP	38.77	19810	564.9	20.24	898.12
Diet 2	441	3	D2,6 NP	37.45	12345	384.3	15.51	859.50
Control	441	4	C7 P	38.81	16941	655.1	20.09	912.83
Control	442	1	C7 NP	39.64	20230	668.6	21.94	951.25
Diet 1	442	2	D1,3 NP	39.62	11822	578.3	19.63	875.45
Diet 2	442	3	D2,1 NP	36.56	6915	358.0	14.94	736.58
Diet 2	442	4	D2,7 NP	39.44	13394	530.1	17.98	851.57
Diet 1	443	2	D1,4 P	39.36	11633	479.4	18.27	832.93
Diet 2	443	3	D2,3 P	37.71	11094	439.2	16.27	810.06
Diet 1	444	2	D1,5 P	36.48	9213	477.5	17.22	826.75
Diet 2	444	3	D2,5 P	39.87	13835	534.0	17.16	838.49
Control	444	4	C5 P	38.66	19753	653.1	21.59	927.76
Control	445	1	C6 NP	40.09	20663	621.9	23.49	945.69

Table 6.1 continued.

Diet 1	445	2	D1,6 P	39.77	14894	676.8	23.78	914.23
Diet 1	445	3	D1,7 P	38.52	13531	563.8	19.30	914.49
Diet 2	445	4	D2,7 P	38.17	10520	521.7	17.43	860.95
Control	446	1	C8 P	40.7	23359	803.6	24.41	962.64
Diet 1	446	2	D1,7 NP	38.65	8771	451.1	20.08	897.14
Diet 1	446	3	D1,8 P	39.13	13179	550.8	18.80	899.18
Diet 2	446	4	D2,8 NP	38.66	9471	590.2	19.96	844.11
Control	447	1	C9 P	41.27	17918	885.5	25.90	967.08
Diet 1	447	2	D1,8 NP	40.45	11966	473.9	20.72	884.59
Diet 2	447	3	D2,8 P	38.33	11850	513.9	17.03	874.66
Diet 2	447	4	D2,9 NP	37.22	14323	393.6	16.52	857.04
Control	448	1	C10 NP	39.56	16283	733.6	22.64	936.44
Diet 1	448	2	D1,9 NP	36.98	12900	447.5	15.92	866.15
Diet 2	448	3	D2,9 P	39.66	10493	547.9	19.91	865.67
Diet 2	448	4	D2,11 NP	34.32	13003	347.9	16.31	787.43
Control	449	1	C10 P	41.18	17465	726.2	24.23	935.47
Diet 1	449	2	D1,10 NP	37.58	14311	597.9	19.60	885.47
Diet 2	449	3	D2,10 NP	36.72	8111	466.4	15.37	825.34
Diet 2	449	4	D2,11 P	38.42	8257	524.2	18.26	838.04
Control	450	1	C11 NP	40.59	14535	681.1	21.84	924.90
Control	450	2	C11 P	38.33	19372	552.2	22.25	931.65
Diet 1	450	3	D1,11 NP	39.4	14171	595.3	19.91	852.86
Diet 1	450	4	D1,11 P	38.26	15364	533.7	18.64	863.39
Control	472	1	C1 NP	40.72	18027	790.0	25.66	963.72
Diet 2	472	2	D2,1 P	37.88	10448	491.0	16.20	791.87
Diet 1	472	3	D1,1 P	37.81	9519	452.4	16.36	778.94
Control	472	4	C5 NP	40.3	20833	756.8	22.43	914.31
Diet 2	473	1	D2,4 P	37.83	9693	395.1	14.83	848.28
Control	473	2	C3 P	39.29	18847	644.7	22.55	958.62
Diet 2	473	3	D2,4 NP	39.28	9111	484.0	17.30	737.83
Control	473	4	C4 P	39.95	13073	652.9	23.63	925.41

Table 6.2: Exponentially, linearly, and unweighted moments of inertia and section moduli from microCT scans for femurs of rats used in the study in Chapter 2.

		Moment of Inertia			Section Moduli		
Animal#	Area	Exponentially Weighted	Linearly Weighted	Unweighted	Exponentially Weighted	Linearly Weighted	Unweighted
C1 NP	9.03	305.45	58.64	11.10	5.48	28.96	154.66
C1 P	9.25	286.83	71.33	14.97	7.04	33.57	133.41
C10 NP	8.20	225.54	47.28	9.35	5.05	25.56	121.91
C10 P	8.78	304.49	61.94	12.07	6.11	31.36	152.24
C11 NP	8.01	225.67	48.07	9.60	4.99	24.97	112.84
C11 P	8.04	236.37	48.46	9.48	4.86	24.85	126.06
C2 NP	8.18	199.31	43.24	8.60	4.91	24.71	109.21
C2 P	8.24	191.50	41.22	8.24	4.39	21.98	103.51
C3 NP	8.52	277.19	58.69	11.81	5.98	29.72	140.35
C3 P	8.05	194.21	37.35	7.08	3.99	21.04	104.98
C4 NP	8.39	212.20	40.43	7.62	4.48	23.78	121.25
C4 P	8.74	302.72	61.82	12.05	5.60	28.75	139.18
C5 NP	8.32	239.40	50.75	10.01	4.94	25.06	119.70
C5 P	7.89	200.48	41.89	8.39	4.66	23.27	112.95
C6 NP	8.43	244.44	49.15	9.53	5.15	26.57	128.65
C6 P	9.20	321.50	61.32	11.65	5.97	31.45	164.87
C7 NP	7.96	246.36	48.93	9.45	5.04	26.10	129.66
C7 P	7.46	196.12	43.56	8.79	4.75	23.55	103.22
C8 P	8.67	289.31	55.98	10.64	5.39	28.35	148.36
C9 P	9.16	396.10	74.34	13.94	6.56	34.98	188.62
D1,1 NP	6.87	114.74	31.87	7.08	4.10	18.48	65.57
D1,1 P	7.18	99.61	32.69	7.64	4.43	18.95	53.13
D1,10 NP	7.51	186.97	44.03	9.00	4.80	23.48	97.12
D1,11 NP	7.92	191.49	51.90	11.02	5.58	26.28	98.20
D1,11 P	7.32	132.83	35.95	7.67	4.38	20.54	75.90
D1,2 NP	7.82	199.32	47.88	9.79	5.02	24.55	102.21
D1,2 P	6.12	82.95	24.47	5.42	3.23	14.61	49.52
D1,3 NP	7.74	148.17	36.77	7.65	4.31	20.72	84.67
D1,3 P	7.71	201.78	47.64	9.78	5.22	25.41	100.89

Table 6.2 continued.

D1,4 NP	6.58	111.46	29.65	6.38	3.65	16.94	65.57
D1,4 P	7.50	122.29	35.17	7.71	4.22	19.27	68.90
D1,5 NP	6.42	119.88	31.46	6.72	3.95	18.51	66.60
D1,5 P	7.12	111.31	31.33	6.83	3.79	17.41	63.61
D1,6 NP	7.71	184.70	41.75	8.47	4.70	23.19	102.61
D1,6 P	8.83	275.51	60.03	12.00	5.71	28.59	132.78
D1,7 NP	7.59	136.28	32.99	6.84	4.08	19.70	79.00
D1,7 P	7.16	156.74	34.55	6.99	4.00	19.74	89.57
D1,8 NP	8.01	209.27	50.97	10.56	5.21	25.17	95.12
D1,8 P	7.09	162.38	37.71	7.70	4.10	20.11	81.19
D1,9 NP	6.24	110.31	29.26	6.20	3.45	16.26	57.31
D2,1 NP	6.88	79.25	28.77	6.76	3.81	16.21	43.43
D2,1 P	6.94	103.10	35.02	8.06	4.48	19.45	57.28
D2,10 NP	6.32	102.89	31.82	6.93	3.85	17.68	57.97
D2,11 NP	7.03	86.89	27.52	6.18	3.58	15.95	51.87
D2,11 P	7.46	148.23	40.83	8.72	4.53	21.21	78.01
D2,2 NP	6.86	108.36	33.36	7.68	4.21	18.28	61.92
D2,2 P	6.89	104.34	30.20	6.52	3.84	17.76	62.29
D2,3 NP	6.90	122.14	30.63	6.41	3.66	17.50	72.92
D2,3 P	6.82	94.93	28.32	6.42	3.61	15.95	55.03
D2,4 NP	7.95	116.01	42.53	10.27	5.07	21.00	60.26
D2,4 P	5.98	102.84	26.38	5.67	3.24	15.08	61.40
D2,5 NP	8.20	174.25	50.63	11.75	5.80	25.00	89.36
D2,5 P	6.94	145.38	38.75	8.31	4.55	21.23	79.66
D2,6 NP	6.12	98.75	25.56	5.43	3.29	15.49	58.09
D2,7 NP	7.16	141.46	39.18	8.35	4.58	21.47	70.73
D2,7 P	6.87	138.63	34.92	7.34	4.13	19.67	79.22
D2,8 NP	8.08	165.41	45.56	9.66	5.02	23.67	88.22
D2,8 P	6.55	133.10	33.48	7.01	4.00	19.13	71.95
D2,9 NP	6.54	124.42	31.66	6.66	3.98	18.90	70.10
D2,9 P	7.80	193.78	48.08	10.08	5.17	24.66	99.37

Table 6.3: Means and standard deviations of tissue-level mechanical properties and composition by zone for each sample for Chapter 2.

Group	Animal	Zone	Mean Ei	Sdev Ei	Mean H	Sdev H	Mean PO:CH2	Sdev PO:CH2	Mean Carb	Sdev Carb
Control	C2	1	5.87	0.25	0.32	0.01	0.50	0.04	0.14	0.02
Control	C2	2	28.29	8.71	1.00	0.30	6.95	0.87	0.16	0.01
Control	C2	3	29.73	4.61	1.15	0.27	7.93	0.48	0.19	0.00
Control	C2	4	34.22	1.61	1.30	0.04	9.81	0.61	0.21	0.01
Control	C3	1	15.69	7.19	0.62	0.31	4.31	1.45	0.15	0.03
Control	C3	2	29.80	7.04	1.22	0.18	4.48	0.35	0.19	0.08
Control	C3	3	32.50	2.44	1.28	0.12	9.40	0.91	0.18	0.00
Control	C3	4	34.51	2.37	1.38	0.21	9.87	0.53	0.19	0.01
Control	C4	1	7.47	1.19	0.26	0.06	1.76	0.27	0.10	0.03
Control	C4	3	29.72	2.51	1.16	0.14	6.89	0.78	0.16	0.01
Control	C4	2	30.05	1.85	1.04	0.07	6.65	0.73	0.14	0.01
Control	C4	4	33.57	2.15	1.26	0.09	9.25	0.62	0.17	0.01
Control	C6	1	5.04	0.27	0.29	0.03	0.65	0.02	0.14	0.01
Control	C6	4	20.76	2.29	1.05	0.13	9.53	0.59	0.20	0.01
Control	C6	2	23.40	2.22	1.10	0.10	7.65	0.32	0.17	0.01
Control	C6	3	24.00	0.78	1.16	0.09	6.11	2.67	0.18	0.02
Mild	D11	1	5.47	0.21	0.27	0.02	0.82	0.10	0.10	0.04
Mild	D11	2	11.80	4.20	0.50	0.18	3.97	0.47	0.12	0.00
Mild	D11	4	32.04	3.79	1.21	0.24	9.51	0.69	0.18	0.01
Mild	D11	3	34.01	2.38	1.34	0.09	7.40	0.37	0.19	0.02
Mild	D12	1	6.66	0.81	0.40	0.09	0.77	0.12	0.15	0.05
Mild	D12	2	28.15	4.06	1.28	0.13	5.43	0.31	0.15	0.01
Mild	D12	3	28.79	2.44	1.18	0.09	4.62	0.68	0.18	0.04
Mild	D12	4	33.46	0.63	1.35	0.07	6.26	1.02	6.26	1.02
Mild	D13	1	5.98	0.69	0.31	0.04	0.70	0.02	0.13	0.03
Mild	D13	2	16.69	3.23	0.69	0.13	2.41	0.18	0.12	0.01
Mild	D13	3	23.44	3.13	1.02	0.08	4.34	0.31	0.16	0.02
Mild	D13	4	27.21	5.06	1.00	0.16	5.46	1.44	0.14	0.01
Mild	D14	1	15.19	5.39	0.71	0.35	0.60	0.18	0.60	0.18
Mild	D14	3	30.02	2.78	1.24	0.12	7.64	0.57	0.18	0.01

Table 6.3 continued.

Mild	D14	4	31.10	2.27	1.27	0.10	9.90	0.65	0.18	0.00
Mild	D14	2	31.98	1.60	1.21	0.11	6.20	1.18	0.16	0.02
Mild	D16	1	5.62	0.14	0.31	0.01	2.72	0.30	0.14	0.01
Mild	D16	2	24.00	1.44	0.98	0.16	6.87	0.48	0.16	0.01
Mild	D16	3	29.16	2.39	1.15	0.12	4.84	0.99	0.18	0.03
Mild	D16	4	32.81	1.42	1.35	0.11	6.69	0.39	0.15	0.01
Severe	D21	1	22.40	2.06	1.00	0.10	2.33	0.10	0.12	0.02
Severe	D21	2	27.07	2.74	1.07	0.15	3.65	0.21	0.16	0.01
Severe	D21	4	30.72	2.39	1.27	0.13	6.04	0.71	0.17	0.01
Severe	D21	3	32.89	5.16	1.33	0.25	3.33	0.38	0.14	0.02
Severe	D22	1	21.15	4.55	1.03	0.23	1.86	0.27	0.12	0.03
Severe	D22	3	28.77	2.46	1.15	0.15	5.25	0.75	0.14	0.02
Severe	D22	4	31.59	1.52	1.22	0.12	7.29	0.34	0.18	0.00
Severe	D22	2	36.25	1.98	1.54	0.12	5.12	0.75	0.16	0.02
Severe	D23	1	7.22	1.32	0.31	0.06	0.67	0.04	0.16	0.03
Severe	D23	2	20.53	1.92	0.85	0.08	3.49	0.22	0.12	0.01
Severe	D23	3	22.27	3.24	0.91	0.12	6.20	0.41	0.15	0.01
Severe	D23	4	27.64	1.54	0.93	0.10	8.28	0.41	0.17	0.01
Severe	D27	1	7.60	0.71	0.35	0.03	1.18	0.18	0.17	0.03
Severe	D27	2	25.28	1.99	1.06	0.06	3.83	0.34	0.15	0.03
Severe	D27	3	28.17	2.72	1.13	0.29	3.95	0.56	0.17	0.01
Severe	D27	4	32.83	5.05	1.17	0.23	6.62	0.55	0.15	0.01

CHAPTER 7

APPENDIX B: CHAPTER 3 DATA

Table 7.1: Whole bone mechanical testing (3 point bending) and microCT data for the left femurs of rats used in the study in Chapter 3.

			Bending Test Results			MicroCT Data			
Group	ID #	EI (Nmm^2)	Failure Moment (Nmm)	PY Disp (mm)	Failure Disp (mm)	TMD (mg/cc)	Ixx (mm^4)	Iyy (mm^4)	Cortical Area (mm^2)
Control	1	21759	728.70	0.762	1.66	996.67	24.62	12.78	3.63
Control	2	29439	690.82	0.15	0.88	975.16	14.13	9.07	3.53
Control	3	36436	752.10	0.025	0.62	983.90	19.97	10.86	3.55
Control	4	36705	732.96	0.168	0.68	993.67	15.66	9.01	3.99
Control	5	32969	858.11	0.343	0.96	975.19	19.08	10.63	4.08
Control	6	28527	821.94	0.165	0.78	954.19	21.59	13.69	6.02
Control	7	20959	639.50	0.114	0.97	1002.64	15.74	9.44	4.17
Control	8	13645	569.70	0.03	1.10	980.19	12.54	7.27	3.25
Control	9	26629	686.83	0	0.74	1006.38	16.00	8.36	2.41
Control	10	33636	745.11	0.173	0.83	958.52	15.79	9.48	0.89
Control	12	29289	753.44	0.124	0.82	956.37	14.99	8.99	1.14
Control	13	17141	545.36	0.214	1.10	958.53	10.29	6.41	5.13
Control	14	29069	827.38	0	0.85	985.50	20.82	11.77	5.84
Control	15	29823	583.21	0.248	0.97	973.22	18.57	9.90	5.31
Control	16	24213	599.68	0.055	0.79	1000.53	12.07	7.05	4.21
Control	17	39601	836.96	0.09	0.68	983.76	17.72	11.82	5.72
Control	18	28955	747.81	0.04	0.78	988.88	19.49	10.87	5.00
Control	19	23324	623.87	0.667	1.40	1001.11	20.67	9.79	4.86
Control	20	28525	816.59	0.219	0.93	1014.98	17.13	11.02	4.46
Control	21	27348	673.26	0.094	0.77	1007.42	13.80	8.32	4.75
F100	22	26805	603.57	0.345	0.94	961.06	18.45	10.55	3.89
F100	23	32874	732.52	0.12	0.74	965.12	23.68	13.64	3.63
F100	24	21268	571.45	0.236	1.00	997.35	16.49	11.79	3.05
F100	25	20279	563.37	0.304	1.27	980.12	18.22	9.83	3.99
F100	26	23812	596.37	0.428	1.32	971.12	18.36	13.16	4.59
F100	27	16891	680.09	0.24	1.30	992.30	14.75	7.58	2.69
F100	28	18037	629.83	0.846	1.65	990.47	11.96	8.03	3.58
F100	29	14533	586.08	0.662	1.78	1001.37	21.93	11.20	4.33
F100	30	18805	505.27	1.186	1.94	984.06	18.12	11.17	0.42
F100	31	28456	548.68	0.602	1.23	1015.99	21.95	13.13	1.36

Table 7.1 continued.

F100	32	25396	429.51	0.94	1.45	972.23	22.77	14.87	1.26
F100	33	14018	573.89	0.145	1.38	955.88	12.80	7.79	5.21
F100	34	25657	812.70	0.009	0.94	950.49	21.56	11.95	6.03
F100	35	27838	611.34	0.458	1.02	985.80	21.09	12.34	5.82
F100	36	34114	780.44	0.239	0.82	981.47	21.48	12.62	4.89
F100	37	23645	765.34	0.502	1.40	974.60	23.22	11.35	5.34
F100	38	19009	440.75	0.616	1.37	1030.27	15.62	9.94	4.52
F100	39	18453	394.12	0.778	1.50	981.16	15.58	9.20	4.55
F100	40	21615	230.63	1.005	1.67	1001.58	13.63	8.66	3.74
F100	41	15680	657.70	0.374	1.45	971.28	17.51	9.14	4.89
F100	42	27873	697.24	0.153	0.97	1037.52	15.53	9.38	4.41
F150	43	13711	309.30	0.663	1.66	933.97	17.61	9.38	3.56
F150	44	18504	468.45	0.433	1.30	976.95	15.26	8.45	3.20
F150	45	12215	410.12	0.713	2.00	966.74	15.54	9.71	4.42
F150	46	29114	467.30	0.592	1.11	997.54	15.74	9.01	3.88
F150	47	17541	462.46	1.13	2.00	957.84	16.30	9.98	3.61
F150	48	26688	926.32	0.594	1.45	972.85	20.71	12.22	3.87
F150	49	16041	928.07	0.648	1.50	1013.00	24.71	15.23	3.85
F150	50	21405	543.12	0.594	1.22	938.68	17.26	10.05	1.04
F150	51	12239	487.67	0.02	1.21	998.61	21.11	10.93	1.55
F150	52	13622	523.86	0.467	1.45	994.53	17.20	9.19	0.71
F150	53	10310	228.79	1.101	1.80	941.61	17.02	9.59	6.65
F150	54	18252	663.14	0.085	1.11	912.95	15.94	9.52	4.38
F150	55	14775	428.74	1.125	1.81	977.72	22.09	13.37	5.05
F150	56	23560	398.43	1.24	1.76	1033.52	13.09	7.70	3.99
F150	57	21718	449.34	0.627	1.33	981.16	20.39	11.83	4.16
F150	58	22149	522.24	1.599	2.24	954.98	19.79	11.33	5.04
F150	59	14723	427.30	1.15	2.13	976.80	19.94	11.04	4.78
F150	60	9733	223.25	1.24	2.19	962.18	14.60	7.26	4.15
F150	61	13640	541.60	0.409	1.53	992.93	11.81	7.15	4.30
F150	62	25085	765.27	0.215	0.98	989.94	20.13	10.40	4.09
F150	63	10112	503.43	0.588	1.89	934.23	17.45	9.41	4.94

Table 7.2: Means and standard deviations of tissue-level mechanical properties and composition by zone for each sample for Chapter 3.

Group	Sample	Zone	Average				Standard Deviations			
			Ei (GPa)	H(GPa)	Min:Mat	Carb	Ei (GPa)	H(GPa)	Min:Mat	Carb
100ppm	33	1	7.97	0.35	4.60	0.18	1.13	0.11	0.71	0.01
100ppm	33	2	30.88	1.16	5.56	0.20	2.36	0.10	0.41	0.02
100ppm	33	3	29.51	1.11	6.05	0.21	1.39	0.13	1.08	0.01
100ppm	33	4	32.89	1.18	6.65	0.20	2.96	0.25	0.82	0.01
100ppm	35	1	25.31	1.11	2.09	0.18	8.75	0.48	0.69	0.03
100ppm	35	2	32.72	1.18	3.99	0.22	1.45	0.08	0.30	0.01
100ppm	35	3	30.49	1.12	7.46	0.18	1.27	0.10	0.80	0.02
100ppm	35	4	34.42	1.32	8.10	0.20	1.20	0.18	0.48	0.01
100ppm	36	1	18.95	0.70	3.79	0.19	6.18	0.20	0.68	0.02
100ppm	36	2	32.74	1.29	7.47	0.21	1.50	0.09	0.79	0.01
100ppm	36	3	33.12	1.30	6.19	0.21	1.59	0.13	0.30	0.01
100ppm	36	4	33.02	1.30	7.80	0.20	2.83	0.17	0.55	0.01
100ppm	37	1	6.02	0.25	0.79	0.15	0.63	0.01	0.02	0.03
100ppm	37	2	29.85	1.13	5.16	0.17	2.65	0.14	0.96	0.01
100ppm	37	3	31.31	1.12	6.63	0.21	2.97	0.09	0.32	0.01
100ppm	37	4	35.38	1.34	9.09	0.21	0.88	0.16	0.56	0.00
100ppm	38	1	4.86	0.19	0.57	0.19	0.09	0.02	0.05	0.03
100ppm	38	2	29.48	1.09	3.03	0.25	1.71	0.15	0.24	0.03
100ppm	38	3	34.17	1.24	5.02	0.22	2.95	0.08	0.62	0.02
100ppm	38	4	33.76	1.21	6.68	0.23	2.13	0.06	0.42	0.01
150ppm	53	1	6.42	0.25	2.86	0.21	1.29	0.05	0.50	0.02
150ppm	53	2	29.17	1.05	3.80	0.24	2.11	0.13	0.60	0.02
150ppm	53	3	30.92	1.10	6.26	0.23	1.30	0.09	0.64	0.01
150ppm	53	4	32.08	1.12	7.77	0.21	1.56	0.10	0.24	0.01
150ppm	54	1	6.49	0.29	1.43	0.18	1.31	0.06	0.29	0.02
150ppm	54	2	27.73	0.74	5.03	0.20	1.47	0.05	0.34	0.02
150ppm	54	3	27.80	0.75	6.00	0.21	1.41	0.04	0.25	0.01
150ppm	54	4	27.84	0.76	6.24	0.20	0.99	0.05	1.42	0.01
150ppm	55	1	12.36	0.49	4.02	0.18	4.26	0.20	0.64	0.01
150ppm	55	2	28.43	1.16	4.60	0.21	2.04	0.13	0.52	0.02
150ppm	55	3	35.12	1.34	4.92	0.25	3.48	0.16	1.31	0.03
150ppm	55	4	34.96	1.44	7.83	0.20	3.90	0.17	0.45	0.01
150ppm	57	1	6.39	0.34	2.27	0.17	0.73	0.06	0.09	0.03
150ppm	57	2	23.59	0.96	4.36	0.21	2.63	0.16	0.52	0.02
150ppm	57	3	26.07	1.14	3.45	0.24	0.80	0.09	0.24	0.02
150ppm	57	4	26.53	1.22	6.95	0.23	1.29	0.15	0.47	0.01
150ppm	59	1	19.41	0.65	2.33	0.16	5.22	0.20	0.59	0.01
150ppm	59	2	26.61	0.87	4.31	0.21	1.35	0.05	0.47	0.02
150ppm	59	3	29.76	0.95	6.90	0.19	1.51	0.08	0.45	0.01
150ppm	59	4	27.91	0.89	7.79	0.20	1.91	0.13	0.55	0.01
Control	11	1	25.33	0.91	6.27	0.18	2.91	0.19	0.30	0.02
Control	11	2	26.75	0.98	5.84	0.20	1.73	0.20	0.64	0.01
Control	11	3	26.61	1.00	6.43	0.20	2.01	0.17	0.44	0.01

Table 7.2 continued.

Control	11	4	29.69	1.14	8.72	0.21	0.59	0.08	0.25	0.00
Control	12	1	5.99	0.22	2.05	0.16	0.48	0.02	0.46	0.02
Control	12	2	29.59	1.03	3.94	0.22	1.28	0.07	1.12	0.04
Control	12	3	31.21	1.10	3.32	0.22	1.24	0.17	0.53	0.02
Control	12	4	34.54	1.25	6.92	0.21	3.97	0.27	0.53	0.01
Control	15	1	8.09	0.41	3.05	0.17	0.63	0.03	0.20	0.01
Control	15	2	32.37	1.18	4.28	0.19	1.83	0.12	1.35	0.02
Control	15	3	31.83	1.13	4.01	0.29	3.54	0.12	0.20	0.04
Control	15	4	32.49	1.14	6.16	0.22	4.43	0.30	1.31	0.01
Control	17	1	6.49	0.29	2.49	0.17	1.05	0.03	0.66	0.02
Control	17	2	29.05	0.98	4.97	0.20	2.11	0.16	0.30	0.01
Control	17	3	27.72	0.95	5.60	0.21	2.82	0.16	0.58	0.01
Control	17	4	30.81	1.15	7.53	0.21	1.96	0.13	0.36	0.01
Control	18	1	16.17	0.58	4.18	0.26	2.82	0.16	0.36	0.04
Control	18	2	25.83	0.89	4.18	0.21	0.85	0.09	0.36	0.02
Control	18	3	30.00	1.04	5.23	0.24	2.01	0.05	0.38	0.02
Control	18	4	30.81	0.99	6.56	0.22	2.10	0.08	0.34	0.01

CHAPTER 8

APPENDIX C: CHAPTER 4 DATA

Table 8.1: Average tissue-level composition and mechanical properties by sample in addition to donor age, aBMD, and T-score.

Sample ID	Sample Average					BMD L1-L4	Tscore L1-L4	Age
	Carb Sub	FWHM	Min:Mat	Ei (GPa)	H (GPa)			
4	0.19	23.15	6.73	22.13	1.09	NA	NA	61
7	0.21	24.03	6.56	23.49	0.98	0.63	-3.8	87
9	0.17	21.94	5.04	23.35	1.24	0.66	-3.5	87
11	0.21	23.92	6.87	25.13	1.09	0.83	-1.9	61
15	0.18	23.33	4.22	20.91	0.89	0.76	-2.6	92
20	0.17	22.77	6.39	25.07	0.99	0.96	-0.8	74
24	0.19	27.24	6.96	23.15	1.05	0.88	-1.5	58
30	0.23	23.45	5.49	22.32	0.83	1.10	0.5	73
31	0.18	23.92	4.02	17.02	0.87	0.47	-5.2	79
36	0.23	25.01	5.85	18.63	0.77	0.62	-3.9	68
37	0.19	23.54	4.94	19.88	0.92	0.57	-4.4	65

CHAPTER 9

APPENDIX D: MATLAB CODE

9.1 Three Point Bending Analysis

Matlab m-file for analyzing three point bending load-displacement data in the form of text files.

```
%3 pt bend data
%By GKim 04/04/09 edited 06/05/2012 zeros the load based on the ...
    average of
%first few values not from the derivative. Just finds max load
%Makes a structure called "file" with the name of all txt files ...
    in the
%specified folder. "lengthfiles" will be the number of txt files...
     in the
%folder
w = 15%input('What was the span width in mm?  ');
pathname = input('Locate the folder where files are located ');
files = dir(fullfile(pathname,'*.txt'));
lengthfiles = size(files);
lengthfiles = lengthfiles(1,1);
for X=20%[1:lengthfiles]
    data=dlmread([pathname,'\',files(X).name],'\t',11,0); %reads...
         txt reads load-disp starting at row 11 and column 2 to ...
        skip headers and time

    disp = -1*data(:,1); %so graph is right side up
    load = -1*data(:,2); %yeah don't hurt your neck

      plot(disp,load);
     [xstart,ystart]=ginput(1);
     [xend,yend]=ginput(1);

     dispindex = find(disp>xstart);
     dispindexend = find(disp>xend);

     disp = disp(dispindex(1):dispindexend);
     load = load(dispindex(1):dispindexend);

    offsetload = load(1);
    load = load-offsetload;
    offsetdisp = disp(1);
    disp = disp-offsetdisp;


```

```
34      plot(disp,load);
35      axissize = [0,1.2,0,122]
36      axis(axissize)
37      title (files(X).name)
38
39     [x1,y1]=ginput(1);
40     [x2,y2]=ginput(1);
41
42     lin_start = x1;%input('Start of linear region?  ');
43      lin_end = x2;%input('End of linear region?  ');
44      lin_region_start = min(find(disp>lin_start));
45      lin_region_end = min(find(disp>lin_end));
46      %lin_region_start = min(find(disp>.4));
47      %lin_region_end = min(find(disp>.7));
48          dispL = disp(lin_region_start:lin_region_end);
49          loadL = load(lin_region_start:lin_region_end);
50          length_lin= length(dispL);
51
52          close
53      %Fits a line to the a linear portion of curve (dispL,loadL)...
           to get structural stiffness k
54      [curve,gof,output]= fit(dispL,loadL,'poly1');
55          rsquare = gof.rsquare;
56          coeff = coeffvalues(curve);
57          k = coeff(1,1);
58          b = coeff(1,2);
59          yfit = k.*dispL + b;
60
61          EI = k*(w^3)/48;
62
63          %finds the yield point which is defined at 10% reduction...
                of the secant
64      %stiffness (jepsen et al 1996 JOR 14(3):493-499
65      postyield_slope = k-.1*k;
66      postyield_intercept = loadL(1)-postyield_slope*dispL(1);
67      postyield_line = (postyield_slope*disp)+postyield_intercept;
68
69
70     %Finds the index of yield point
71     j= min(find(postyield_line>loadL(length_lin)));
72      while j < length(disp)-1
73          if load(j+1)<postyield_line(j+1)
74              index_yield = j;
75              j=length(disp);
76          else
77              j=j+1;
78          end
79      end
80      Dyield = disp(index_yield);%displacement at yield
81      LOADyield = load(index_yield);
82
83
```

```
84
85      plot(disp,load);
86     [xfail,yfail]=ginput(1);
87
88      A = find(disp≤xfail);
89      Aindex = length(A);
90      Dfail = disp(A(Aindex));
91      Loadfail = load(A(Aindex));
92
93      Dpost = Dfail-Dyield ;% reduced_secant displacement
94
95
96     plot(disp,load,dispL,loadL,dispL,yfit,disp,postyield_line,...
           Dyield,LOADyield,'r*',Dfail,Loadfail,'m*','linewidth',5)
97     axis(axissize)
98      title (files(X).name)
99     pause
100    Loadmax= max(load);
101
102
103
104         sfile=fopen([pathname,'\','20120628...
               _3pt_bend_fluoridehumeri.csv'],'a');
105         fprintf(sfile,'%s,',date); % today's date
106         fprintf(sfile,'%s,',files(X).name);  %reading name (...
               filename)
107
108           fprintf(sfile,'%.3f,',EI); %EI
109           fprintf(sfile,'%.3f,',Dpost);
110            fprintf(sfile,'%.3f,',Dfail);
111             fprintf(sfile,'%.3f,',Loadfail);
112              fprintf(sfile,'%.3f,',Loadmax);
113           fprintf(sfile,'\n'); % newline character
114
115         fclose(sfile);
116 end
```

9.2 Weighted Moment of Inertia from MicroCT Scans

Matlab m-files for calculating density weighted moments of inertia from microCT scans of diaphyseal cortical bone.

```
1 %file name: cortical.m
2 %This script takes all vff files in a folder and finds the ...
```

```
    weighted and
%unweighted moments of inertia and writes the values to a csv ...
    file.
%Directions
%1) Put all vffs you would like to analyze in a folder
%2) Put the following m files in the folder as well
%     a) cortical.m
%     b) readvff.m
%     c)threshold.m
%     d)centroid.m
%     e)MomentInertia.m
% 3) Change the resolution in 'cortical.m' to the correct value
% 4) Run 'cortical.m'
% 5) Output will be in the same folder as vffs and mfiles
pathname = input('Locate the folder where files are located ');
TH = input('Enter the desired threshold value  '); %for vitD HU ...
    equivalent to 0.43g/cc is 879
%res = input('input the resolution of the CT machine in mm ...
    please ');
%first = input('input the number of the 1st slice of the stack ...
    you want to average ');
%last = input('input the number of the last slice of the stack ...
    you want to average ');
res = 0.025;
files = dir(fullfile(pathname,'*.vff'));
lengthfiles = size(files);
lengthfiles = lengthfiles(1,1);
for w=[1:3]%[1:lengthfiles]%%%%%%%%%%%%
     fname= files(w).name;
     [fid,message]=fopen(fname,'r','b');
     tic
     [dArray,header]=readvff(fname);
     toc
     tic
     [Z] = threshold_change_20120605(dArray,TH);
     toc

ZU = 12+(Z/TH);
Zexp =(Z/TH);
Zlin =(Z/TH);
Z2 =(Z/TH);
Z3 =(Z/TH);

     tic
     [x_bar_exp,x_bar_lin,x_bar_u,x_bar_Z2,x_bar_Z3,...
        total_att_exp,total_att_lin,area,total_att_Z2,...
        total_att_Z3]=centroid_20120605(ZU,Zlin,Zexp,Z2,Z3,res)...
        ;
     toc


     tic
```

```
      [Iy_bar_exp,Iy_bar_lin,Iy_bar_u,Iy_bar_Z2,Iy_bar_Z3]= ...
         MomentInertia_20120605(ZU,Zlin,Zexp,Z2,Z3,res,x_bar_exp...
         ,x_bar_lin,x_bar_u,x_bar_Z2,x_bar_Z3,total_att_exp,...
         total_att_lin,area,total_att_Z2,total_att_Z3,TH);
      toc



      w
    %close figure 12
% Iy_bar_min= min(Iy_bar);
% Iy_bar_u_min= min(Iy_bar_u);
% area_min = min(area);
% total_att_min = min(total_att);
%  Iy_bar_exp_ave= mean(Iy_bar_exp);
%  Iy_bar_lin_ave= mean(Iy_bar_lin);
%  Iy_bar_u_ave= mean(Iy_bar_u);
%  x_bar_exp_ave= mean(x_bar_exp);
%  x_bar_lin_ave= mean(x_bar_lin);
%  x_bar_u_ave= mean(x_bar_u);
%  x_bar_Z2_ave= mean(x_bar_Z2);
%  x_bar_Z3_ave= mean(x_bar_Z3);
%total_att_ave = mean(total_att);
%Print information to a csv file
 sfile=fopen([pathname,'\','test2.csv'],'a');
      fprintf(sfile,'%s,',date); % today's date
      fprintf(sfile,'%s,',fname);  %reading name (filename)
%       fprintf(sfile,'%.3f,',area_min); %
%       fprintf(sfile,'%.3f,',total_att_min); %
%       fprintf(sfile,'%.3f,',Iy_bar_min); %
%       fprintf(sfile,'%.3f,',Iy_bar_u_min); %

      %fprintf(sfile,'%.3f,',total_att_ave); %
      fprintf(sfile,'%.3f,',Iy_bar_exp); %
      fprintf(sfile,'%.3f,',Iy_bar_lin);
      fprintf(sfile,'%.3f,',Iy_bar_u); %
       fprintf(sfile,'%.3f,',Iy_bar_Z2); %
       fprintf(sfile,'%.3f,',Iy_bar_Z3); %


%       fprintf(sfile,'%.3f,',x_bar_exp); %
%       fprintf(sfile,'%.3f,',x_bar_lin);
%       fprintf(sfile,'%.3f,',x_bar_u); %
%         fprintf(sfile,'%.3f,',x_bar_Z2); %
%           fprintf(sfile,'%.3f,',x_bar_Z3); %
      fprintf(sfile,'\n'); % newline character
      fclose(sfile);
end
```

```
function [dArray,header] = readvff(fname);
% function dArray = readvff(fname)
```

```
3  %
4  % reads EVS *.vff volume files (16 bit).
5  %
6  %   Author: Timothy Morgan
7  %   Created: 04/03/01
8  %     Modified: 08/06/02 by TGM
9  %          - added ability to read 2D vff images
10 %     Modified: 10/24/02 by TGM
11 %          - added try/catch for initializing dArray
12 %          - in catch, added cat of small integer arrays
13 %            to initialize dArray
14 %     Modified:  2/18/03 by MvdM
15 %          - added semicolons to prevent print to screen
16 %     Modified: 6/19/08 by KMS
17 %          - fixed code to recognize 'ncaa' in header
18 %          - added more comments
19 %
20 % Input: fname - name of input file (with extension)
21 %
22 % Output: dArray - 3D matlab array. Dimensions of array ...
       correspond to
23 % coordinate of each voxel. Values in array are corresponding CT...
       values in
24 % the Hounsfield scale (HU).
25 % open file (note 'b' for big-endian)
26 [fid,message] = fopen(fname,'r','b');
27 % find file info (size in bytes, for use later)
28 fInfo = dir(fname);
29 endHeader = 0;
30 lineNbr = 1;
31 while(endHeader == 0);
32     tline = fgetl(fid);
33     if strcmp(tline, 'ncaa');
34         tline = fgetl(fid);
35     end;
36     if(tline(end) == ';');
37     header{lineNbr} = tline;
38     lineNbr = lineNbr + 1;
39     else;
40     endHeader = 1;
41     end;
42 end;
43 % parse header info to determine size of data
44 knowSize = 0;
45 lineNbr = 1;
46 while(knowSize == 0);
47   tline = header{lineNbr};
48   if(strcmpi('size',tline(1:4)));
49     knowSize = 1;
50   else;
51     lineNbr = lineNbr + 1;
52   end ;
```

```
end;
% read dimensions of data from 'size=' line in header
equalsLoc = find(tline == '=');
temp = tline(equalsLoc+1:end-1); %extract dimensions (still has ...
    spaces)
dimSpaces = find(isspace(temp)); %location of spaces
nbrDims = (size(dimSpaces,2) + 1); %# of spaces + 1 = # of Dims
if(nbrDims == 3); %if 3D
  dim1 = str2num(temp(1:dimSpaces(1)-1));
  dim2 = str2num(temp(dimSpaces(1)+1:dimSpaces(2)-1));
  dim3 = str2num(temp(dimSpaces(2)+1:end));
elseif(nbrDims == 2); %if 2D
  dim1 = str2num(temp(1:dimSpaces(1)-1));
  dim2 = str2num(temp(dimSpaces(1)+1:end));
  dim3 = 1;
end;
% calculate offset (byte where CT data begins after header)
offset = (fInfo.bytes - 2*(dim1*dim2*dim3));
% skip to where data begins
fseek(fid,offset,-1);%set file position indicator. -1 signals ...
    beginning of file.
cwd = pwd; %pwd prints current working directory
cd(tempdir); %change directory to temporary directory
pack; %consolidate workspace memory
cd(cwd);  %change directory back
% initialize data array. Makes computing faster.
%try hints the computer that an error may occur
try; %direct try of zeros array
  dArray = int16(zeros(dim1,dim2,dim3));
catch; %if error does occur (dimensions too big)
  try;
    dim3_1 = round(dim3/4); %try 1/4 of dim 3, make an array 1/4...
        of the original size
    temp = int16(zeros(dim1,dim2,dim3_1));
    dArray = cat(3,temp,temp,temp,temp); %cat concatenates 4 ...
        input arrays into one 3D array
    clear temp;
  catch;
    disp('Not enough memory for array initialization'); %give ...
        up.
    return;
  end;
end;
% read data, one slice at a time
for slice = 1:dim3;
   [temp,count] = fread(fid,[dim1,dim2],'short');
   dArray(:,:,slice) = int16(temp);
end;
fclose(fid);
```

```
function [Z,ZU,Zlin,Zexp] = threshold_20110715(dArray,TH)
```

```
%Removes first slice and last 2 of imported vff because ...
    sometimes those are
%blank from exporting from microView
dim = size(dArray);
first = 2;
last = dim(3)-2;
z = dArray(:,:,first:last);
dims=size(z);
%Z-This makes the background values 0 and maintains the value of...
     anything
%above the designated threshold
for L = [1:dims(3)]
    for k = [1:dims(2)]
        for j = [1:dims(1)]
            if z(j,k,L)<TH
                Z(j,k,L)=0;
            else
                Z(j,k,L) = z(j,k,L);
            end
        end
    end
end
Z=double(Z);
%ZU-This makes values below the threshold 0 and above it 1. Used...
     in unweighted
%centroid, MOI ect
for L = [1:dims(3)]
    for k = [1:dims(2)]
        for j = [1:dims(1)]
            if z(j,k,L)<TH
                ZU(j,k,L)=0;
            else
                ZU(j,k,L) = 1;
            end
        end
    end
end
ZU=double(ZU);
%Zlin- was calculated in here because needed to calculate do a ...
    loop to only
%scale non-zero entries in Z matrix
for L = [1:dims(3)]
    for k = [1:dims(2)]
        for j = [1:dims(1)]
            if z(j,k,L)<TH
                Zlin(j,k,L)=0;
            else
                Zlin(j,k,L) = ((z(j,k,L)/TH)*2.4);
            end
        end
    end
end
```

```
Zlin=double(Zlin);
%Zexponential is calculated here
Zexp = (Z/TH).^(3.91);
```

```
 %function [x_bar,y_bar,total_att,x_bar_u,y_bar_u,area]=...
    centroid_20110715(Zlin,ZU,Zexp,res)
 function [x_bar_exp,x_bar_lin,x_bar_u,x_bar_Z2,x_bar_Z3,...
    total_att_exp,total_att_lin,area,total_att_Z2,total_att_Z3...
    ]=centroid_20120605(ZU,Zlin,Zexp,Z2,Z3,res)
%Finds the centroid of the object after it has been thresholded.
%If thresholded to assume a homogeneous material, it will not be...
    weighted
%because Z values will be 1 or 0.
%If thresholded retain heterogeneous material, centroid values ...
   will be
%weighted because Z values will be in HU
dA = res^2;
dim = size(ZU);
%dim = [5 5 5];
%Finds x coordinate of the the density weighted and unweighted ...
   centroid %%
for L = [1:dim(1,3)] % Goes through for each slice in Z and sets...
    up variables
    %Setting up variable names

    x_bara_exp_=0;
    x_bara_lin_=0;
    x_bara_u_=0;
     x_bara_Z2_=0;
      x_bara_Z3_=0;


%     y_bara_exp_=0;
%     y_bara_lin_=0;
%     y_bara_u_=0;

    total_att_exp_ = 0;
    total_att_lin_ = 0;
    area_=0;
    total_att_Z2_ = 0;
    total_att_Z3_ = 0;


    for kk = [1:dim(2)] % for each column
        for jj = [1:dim(1)] % for each to row
            if Zexp(jj,kk,L)>0

            %exp Relationship, Ei is modulus of each pixel but ...
               in this case
            %exponentially weighted attenuation modulus is ...
               surgate for
```

```
39              %modulus value of the pixel
40              %y_Bar = sum(y*ni*Ai)/sum(Ei*Ai) thus y_bara = sum(y...
                    *ni/Ai)
41              %total_att = sum(ni*Ai)
42              x_bara_exp_ = x_bara_exp_ + ((Zexp(jj,kk,L))*dA*((kk...
                    -.5)*res));
43            %  y_bara_exp_ = y_bara_exp_ + ((Zexp(jj,kk,L))*dA*((...
                   jj-.5)*res));
44
45              %total_mineral_ = total_mineral_+(Z(jj,kk,L)...
                    *(1073/2194000));% in g
46              total_att_exp_ = total_att_exp_ + Zexp(jj,kk,L)*dA;
47
48              %linear relationship, Ei is modulus of each pixel ...
                    but in this case
49              %linearly weighted attenuation modulus is surgate ...
                    for
50              %modulus value of the pixel
51              x_bara_lin_ = x_bara_lin_ + ((Zlin(jj,kk,L))*dA*((kk...
                    -.5)*res));
52          %    y_bara_lin_= y_bara_lin_ + ((Zlin(jj,kk,L))*dA*((jj...
                -.5)*res));
53              total_att_lin_ = total_att_lin_ + Zlin(jj,kk,L)*dA;
54              %Unweighted
55              x_bara_u_ = x_bara_u_ + (ZU(jj,kk,L)*dA*((kk-.5)*res...
                    ));%changed
56       %       y_bara_u_ = y_bara_u_ +(ZU(jj,kk,L)*dA*((jj-.5)*res...
             ));%changed
57              area_ = area_ + ZU(jj,kk,L)*dA;         %changed
58
59              %Z2
60              x_bara_Z2_ = x_bara_Z2_ + ((Z2(jj,kk,L))*dA*((kk-.5)...
                    *res));
61         %      y_bara_Z2_ = y_bara_Z2_ + ((Z2(jj,kk,L))*dA*((jj-.5...
              )*res));
62
63              %total_mineral_ = total_mineral_+(Z(jj,kk,L)...
                    *(1073/2194000));% in g
64              total_att_Z2_ = total_att_Z2_ + Z2(jj,kk,L)*dA;
65
66                %Z3
67              x_bara_Z3_ = x_bara_Z3_ + ((Z3(jj,kk,L))*dA*((kk-.5)...
                    *res));
68       %        y_bara_Z3_ = y_bara_Z3_ + ((Z3(jj,kk,L))*dA*((jj-.5...
            )*res));
69
70              %total_mineral_ = total_mineral_+(Z(jj,kk,L)...
                    *(1073/2194000));% in g
71              total_att_Z3_ = total_att_Z3_ + Z3(jj,kk,L)*dA;
72
73
74
```

```
75
76              end
77          end
78      end
79  x_bara_exp(L) = x_bara_exp_;
80  x_bara_lin(L) = x_bara_lin_;
81  x_bara_u(L)= x_bara_u_;
82  x_bara_Z2(L)= x_bara_Z2_;
83  x_bara_Z3(L)= x_bara_Z3_;
84  total_att_exp(L) = total_att_exp_;%units of res (length^2)
85  total_att_lin(L) = total_att_lin_;
86  area(L) = area_ ;
87  total_att_Z2(L) = total_att_Z2_;
88  total_att_Z3(L) = total_att_Z3_;
89  %  y_bara_exp(L) = y_bara_exp_;
90  %  y_bara_lin(L) = y_bara_lin_;
91  %  y_bara_u(L) = y_bara_u_;
92  %   y_bara_Z2(L) = y_bara_Z2_;
93  %    y_bara_Z3(L) = y_bara_Z3_;
94  end
95  x_bar_exp=x_bara_exp./total_att_exp; %units [HU*length]/[HU]=...
        length
96  x_bar_lin=x_bara_lin./total_att_lin;
97  x_bar_u = x_bara_u./area;
98  x_bar_Z2=x_bara_Z2./total_att_Z2;
99  x_bar_Z3=x_bara_Z3./total_att_Z3;
100 %  y_bar_exp=y_bara_exp./total_att_exp; %units [HU*length]/[HU]=...
        length
101 %  y_bar_lin=y_bara_lin./total_att_lin;
102 %  y_bar_u=y_bara_u./area;  %units [lenght^3]/[Area]=length
103 %   y_bar_Z2=y_bara_Z2./total_att_Z2;
104 %   y_bar_Z2=y_bara_Z2./total_att_Z2;
```

```
1  function [Iy_bar_exp,Iy_bar_lin,Iy_bar_u,Iy_bar_Z2,Iy_bar_Z3]= ...
       MomentInertia_20120605(ZU,Zlin,Zexp,Z2,Z3,res,x_bar_exp,...
       x_bar_lin,x_bar_u,x_bar_Z2,x_bar_Z3,total_att_exp,...
       total_att_lin,area,total_att_Z2,total_att_Z3,TH)
2  %calculates the moment of inertia based on using finite ...
       summation of pixels
3  %from a microct Vff file. When testing on known geometry (...
       rectangle) error
4  %due to different between integration and descrete area ...
       summation, error
5  %decreases as the the ?_area is a smaller percentage of the ...
       total area
6  dA = res^2;
7  dim=size(ZU);
8  %%%%%%%% Corcoran et al method for mass weighted %%%%%%%%%%
9  %%%%%%%%%%%%%%%% moment of inertia calculatios %%%%%%
10 for L = [1:dim(1,3)] % for every slice in Z
11 %Sets up variable names
```

```
% Ix_exp_ = 0;
% Ix_lin_ = 0;
% Ix_u_ = 0;
Iy_exp_ = 0;
Iy_lin_ = 0;
Iy_u_ = 0;
Iy_Z2_ = 0;
Iy_Z3_ = 0;
    for kk = [1:dim(1,2)]
        for jj = [1:dim(1,1)]
            if ZU(jj,kk,L)>0

                %exp relationship between att and E
                Iy_exp_ = Iy_exp_ + (((Zexp(jj,kk,L))*((kk-0.5)...
                    *res)^2)*dA);
          %       Ix_exp_ = Ix_exp_ + (((Zexp(jj,kk,L))*((jj-0.5...
              )*res)^2)*dA);
                %linear relationship between att and E
                Iy_lin_ = Iy_lin_ + (((Zlin(jj,kk,L))*((kk-0.5)...
                    *res)^2)*dA);
           %      Ix_lin_ = Ix_lin_ + (((Zlin(jj,kk,L))*((jj-0.5...
               )*res)^2)*dA);
                %Unweighted
                Iy_u_ = Iy_u_ + (((ZU(jj,kk,L))*((kk-0.5)*res)...
                    ^2)*dA); %Sum(scaling factor*y^2*area)
           %      Ix_u_ = Ix_u_ + (((ZU(jj,kk,L))*((jj-0.5)*res)...
              ^2)*dA); %units of this are the units of res^4

                %Z2
                Iy_Z2_ = Iy_Z2_ + (((Z2(jj,kk,L))*((kk-0.5)*res...
                    )^2)*dA); %Sum(scaling factor*y^2*area)

                %Z3
                Iy_Z3_ = Iy_Z3_ + (((Z3(jj,kk,L))*((kk-0.5)*res...
                    )^2)*dA); %Sum(scaling factor*y^2*area)
            end
        end
    end

% Ix_exp(L) = Ix_exp_;
% Ix_lin(L) = Ix_lin_;
% Ix_u(L) = Ix_u_;
Iy_exp(L) = Iy_exp_;
Iy_lin(L) = Iy_lin_;
Iy_u(L) = Iy_u_;
Iy_Z2(L) = Iy_Z2_;
Iy_Z3(L) = Iy_Z3_;
end
%Using parallel axis theorm to find moment of inertia about the ...
    centroid
%Ix_bar_u = Ix_u -(area.*(y_bar_u.^2));
Iy_bar_u = Iy_u -(area.*(x_bar_u.^2));
```

```
%Ixy_bar_u = Ixy_u_-(area.*y_bar_u.*x_bar_u);
%Ix_bar_exp = Ix_exp - (total_att_exp.*(y_bar_exp.^2)); %y_bar_*...
     is in units same as res
%Ix_bar_lin = Ix_lin - (total_att_lin.*(y_bar_lin.^2)); %...
    total_Att is in res^2
Iy_bar_exp = Iy_exp - (total_att_exp.*(x_bar_exp.^2));
Iy_bar_lin = Iy_lin - (total_att_lin.*(x_bar_lin.^2));
Iy_bar_Z2 = Iy_Z2 - (total_att_Z2.*(x_bar_Z2.^2));
Iy_bar_Z3 = Iy_Z3 - (total_att_Z3.*(x_bar_Z3.^2));
%%%%%%%%%%%%%%%%%%%%%%%%%
%Calculate averages%%%%
%Ix_bar_u = mean(Ix_bar_u);
Iy_bar_u = mean(Iy_bar_u);
%Ix_bar_exp = mean(Ix_bar_exp);
%Ix_bar_lin = mean(Ix_bar_lin);
Iy_bar_exp = mean(Iy_bar_exp);
Iy_bar_lin = mean(Iy_bar_lin);
Iy_bar_Z2 = mean(Iy_bar_Z2);
Iy_bar_Z3 = mean(Iy_bar_Z3);
```

9.3 Raman Spectra Analyzer

Matlab m-file that calculates peak height ratios for bone compositionl parameters.

```
%This script takes raman image txt files and gets out peak ...
    intensities of
%interest
%Instructions
%1)Make a folder and put in all data files in txt format along ...
    with the
     %following m-files:
     %Raman_Mapping_Analysis
     %RamanImageFileDivider
     %RamanBackgroundSub3rd
     %SpectralSmoother
     %RamaPeakFinder
%2) Change the file names in line 35 and 36 to what you would ...
    like
%3) You can change the length of the running average for the ...
    spectra
%smoother and the polynomial power for the background ...
    subtraction,
%currently set to 9pt moving average and 3rd order polynomial ...
    fit
```

```
%4)Run the Raman_Mapping_Auto_Output and enter in directory with... all data
%files when prompted to
%5) As file runs, plots of all the spectra with peak intensities... are
%displayed one by one, go to RamanPeakFinder to turn off ploting
pathname = input('Locate the folder where files are located ');
files = dir(fullfile(pathname,'*.txt'));
lengthfiles = size(files);
lengthfiles = lengthfiles(1,1);
for j=[1:lengthfiles]
     fname= files(j).name;
     data = importdata(fname);
     [outputs] = Raman_Mapping_Analysis(data)
     j
close all
%%%%%%%%% Print information to a csv file
%Separate file for data and files names associated with each ... data point.
dlmwrite('Raman_mapping_output.csv', outputs,'-append')
sfile=fopen([pathname,'\','Raman_mapping_names.csv'],'a');

dims = size(outputs);
for k=[1:dims(1)]
fprintf(sfile,'%s,',date); % today's date
fprintf(sfile,'%s,',fname);  %reading name (filename)
fprintf(sfile,'\n'); % newline character
end
fclose(sfile);
end
```

```
function [outputs] = Raman_Mapping_Analysis(data)
    warning off
%Divides up the long txt file with map data into individual ... spectra
    [spectra] = RamanImageFileDivider(data);
%Does background subtraction for each of the spectra.
%S is spectral data S(wavenumber,Intensity, spectranumber in map... )
%dim is the number of points in your mapping data
    dim = size(spectra);
for i = 1:dim(3)
    [S(:,:,i)] = RamanBackgroundSub3rd(spectra(:,:,i));
end
%Initializing matricies used in the loop below
SS = S;
XVAL = zeros(dim(3),7);
YVAL = zeros(dim(3),7);
MAP = zeros(dim(3),6);
%Finds the peaks of interest for each spectra
for w=[1:dim(3)]
```

```
19      %smooth the spectra. First entry is the number of points ...
            used for
20      % running average.SmoothS is a smoothed spectral intensity ...
            matrix
21      [SmoothS] = SpectralSmoother(9,S,w);
22
23      %Insert the SmoothS into SS matrix with map position and ...
            wavenumber
24      %info
25      SS(:,4,w)=SmoothS;
26
27      %Finds peaks of interest
28      %wavenumbers is vector with wave number of peaks of interest
29      %wavenumber of PO,CO,CH2,AM1,Resin,Ph,PO FWHM
30      %intensities are the raw intensity  values of peaks of ...
            interest
31      %intensities of PO,CO,CH2,AM1,Resin,Ph,PO FWHM
32      %Map  is x position, y position, po:ch2, po:amide1, co:po,...
            fwhm
33      [wavenumbers, intensities,MAP] = RamanPeakFinder(SS,w);
34  outputs(w,:)=[wavenumbers,intensities];
35  end
36  %Finds the distances between where each spectra was taken
37  % position = 0;
38  % for c = [1:w];
39  %     position(c)= sqrt(((MAP(c,1)-MAP(1,1))^2)+((MAP(c,2)-MAP...
        (1,2))^2));
40  % end
41  %plots phos:ch2 wag peaks at each position
42  %ZZ = meshgrid(MAP(:,4),MAP(:,2),MAP(:,1));
43  %surf(ZZ)
```

```
1   function [spectra] = RamanImageFileDivider(data)
2   %the format of the [spectra] matrix is the same as the original ...
        data.
3   %spectra(xposition map,yposition map, wave#, intensity)
4   %Raman Imaging file divider
5   %Divides Raman imaging file into individual spectra based on ...
        changes
6   %detected in the x,y coordinate data of each spectra which is ...
        held in
7   %columns 1 and 2 of data.
8   x = data(:,1);
9   y = data(:,2);
10  j = 2;
11  %sets the first value in split as 1
12  split(1)=1;
13  for i = 2:length(x)
14      if x(i)~=x(i-1) | y(i)~=y(i-1)
15          split(j) = i;
16          j = j+1;
```

```
    end
end
%Makes the last "split" value the length of the file
split(length(split)+1)=length(x);
m=2;
%Separates each spectra except for the last one into a 3d matrix
for k = 1:length(split)-2
    if k==1
        spectra(:,:,k) = data(1:split(2)-1,:);
    else
        spectra(:,:,m) = data(split(k):split(k+1)-1,:);
        m=m+1;
    end
end
%Puts the last spectra into the end of the 3D matrix
spectra(:,:,m) = data(split(length(split)-1):split(length(split)...
    ),:);
```

```
function [S] = RamanBackgroundSub3rd(spectra)
%Modified 06032010 by Grace
%This program automates background subtraction for Raman Spectra
%[S] is the same format at spectra, S(xposition map, yposition ...
    map,wave#,
%intensity)
%truncates data to be between wave numbers between 800 and 1800
ind = find ((spectra(:,3)<1800)& spectra(:,3)>800);
spectra = spectra(min(ind):max(ind),:);
%Take a spectra matrix and separate into wavenumber and ...
    intensity
%values (x and y)
x = spectra(:,3);
y = spectra(:,4);
%Fit a polynomial to the spectra in this case a 3th order
[curve,gof,output]= fit(x,y,'poly3');
gof
p1 = curve.p1;
p2 = curve.p2;
p3 = curve.p3;
p4 = curve.p4;
%F is a vector with the fit, each column is each fit iteration
for i = 1:length(x)
    F(i,1) = p1*x(i)^3 + p2*x(i)^2 + p3*x(i) + p4;
end
%Trunc takes the best fit curve and the actual data and for each...
     wave
% number finds the mininum value. Polynomial is fit again to ...
    trunc of the
% most previous iteration
for i = 1:length(F)
    if F(i,1)≤y(i)
        trunc(i,1)= F(i,1);
```

```
    else
        trunc(i,1)= y(i);
    end
end
%This section repeates the polynomial fit and and truncation ...
   until the
%sum of squared difference equals a user defined value, res
% is initialized as 1 to start the first iteration, it is
% redefined in the loop, loop continues while res is greater ...
   than 0.01,
% this indicates the fitted background is not changing much with...
    each
% iteration
res = 1;
j=1;
while res > .01
    [curve,gof,output]= fit(x,trunc(:,j),'poly3');
    p1 = curve.p1;
    p2 = curve.p2;
    p3 = curve.p3;
    p4 = curve.p4;

    j=j+1;
    for i = 1:length(x)
        F(i,j) = p1*x(i)^3 + p2*x(i)^2 + p3*x(i) + p4;
    end

    b = size(F);
    for i = 1:b(1)
        if F(i,j)≤y(i)
            trunc(i,j)= F(i,j);
        else
            trunc(i,j)= y(i);
        end
    end
    diff = F(i,j)-F(i,j-1);
    res = diff.^2;

   end
dim = size(F);
S(:,1) = spectra(:,1);
S(:,2) = spectra(:,2);
S(:,3) = spectra(:,3);
S(:,4) = spectra(:,4)-F(:,dim(2));
```

```
function [SmoothS] = SpectralSmoother(n,S,w)
%where (make n odd) n is the length of the running average ...
   desired
% S is the spectra to be smoothed
% w is the number of the spectra in the map
n=(n-1)/2;
```

```
%SS(:,:,w)=S(:,:,w);
for i = 1:length(S)
    if i < n+1
        SmoothS(i,1)=S(i,4,w);
    elseif i ≥ n+1 & i<length(S)-4
        SmoothS(i,1) = mean(S(i-n:i+n,4,w));
    else
        SmoothS(i,1)=S(i,4,w);
    end
end
%
% for i = 1:length(S)
%     if i < n+1
%         SS(i,4,w)=S(i,4,w);
%     elseif i ≥ n+1 & i<length(S)-4
%         SS(i,4,w) = mean(S(i-n:i+n,4,w));
%     else
%         SS(i,4,w)=S(i,4,w);
%     end
% end
```

```
function [wavenumbers,intensities,Map] = RamanPeakFinder(SS,w)
%added with jayme's fwhm code 20110404
%Searches between set wavelengths for peaks
xy=[950;970;1060;1080;1440;1465;1590;1700;800;820;995;1010];
%Finds FWHM of Phosphate peak
phos_index = find(SS(:,3,w)≥950 & SS(:,3,w)≤1010);
phosx = round(SS(phos_index(1):phos_index(end),3,w));
phosy = SS(phos_index(1):phos_index(end),4,w);
f = fittype('gauss2');
Options = fitoptions('gauss2');
Options.StartPoint = [1.74e+03 960 6.097 1.06e+03 969 7.714];
Options.Upper = [Inf 966 Inf Inf Inf Inf];
Options.Lower = [-Inf 958 0 -Inf -Inf 0];
phos_fit = fit(phosx,phosy,f,Options);
peakposition(1,1)= phos_fit.b1 %wavenumber of peak intensity of ...
    phosphate
xvalue(3,7) = peakposition(1,1)
xvalue(1,7)=phos_fit.b1
phos_max_index = find(phosx ==round(phos_fit.b1))
Q = isempty(phos_max_index);
if Q==1
    phos_max_index = find(phosx ==round(phos_fit.b1)-1);
end
R = isempty(phos_max_index);
if R==1
    phos_max_index = find(phosx ==round(phos_fit.b1)+1);
end

intensity(1,1) = phosy(phos_max_index)%max counts of phosphate ...
    peak
```

```
xvalue(2,7)=intensity(1,1)
peaksigma(1,1)= phos_fit.c1 %sigma of gauss fit of phosphate
FWHM = 2*sqrt(2*log(2))*phos_fit.c1 %fwhm of phosphate peak
clear Q
%Finds peak value for Phospahte band
clear phos
phos(:,1)=find(SS(:,3,w)>xy(1,1) & SS(:,3,w)<xy(2,1)); %finds ...
    wave numbers of the phosphate peak area in spectra
phosphate(1,1)=max(SS((phos(1,1):phos(end,1)),4,w)); % takes the...
     max y value from these x values
xvalue(1,1)=find(SS((phos(1,1):phos(end,1)),4,w)== phosphate...
    (1,1)); %finds the index of the maximum value
xvalue(2,1)=phos(xvalue(1,1),1);
xvalue(3,1)=SS(xvalue(2,1),3,w);
%Finds peak value for Carbonate band
clear carb
carb(:,1)=find(SS(:,3,w)>xy(3,1) & SS(:,3,w)<xy(4,1));
carbonate(1,1)=max(SS((carb(1,1):carb(end,1)),4,w));
xvalue(1,2)=find(SS((carb(1,1):carb(end,1)),4,w)== carbonate...
    (1,1));
xvalue(2,2)=carb(xvalue(1,2),1);
xvalue(3,2)=SS(xvalue(2,2),3,w);
%Finds the peak for the CH2 wag
clear CH
CH(:,1)=find(SS(:,3,w)>xy(5,1) & SS(:,3,w)<xy(6,1));
CH2(1,1)=max(SS((CH(1,1):CH(end,1)),4,w));
xvalue(1,3)=find(SS((CH(1,1):CH(end,1)),4,w)== CH2(1,1));
xvalue(2,3)=CH(xvalue(1,3),1);
xvalue(3,3)=SS(xvalue(2,3),3,w);
%Finds the peak for the Amide I wag
clear amide
amide(:,1)=find(SS(:,3,w)>xy(7,1) & SS(:,3,w)<xy(8,1));
Amide(1,1)=max(SS((amide(1,1):amide(end,1)),4,w));
xvalue(1,4)=find(SS((amide(1,1):amide(end,1)),4,w)== Amide(1,1))...
    ;
xvalue(2,4)=amide(xvalue(1,4),1);
xvalue(3,4)=SS(xvalue(2,4),3,w);
%Finds the peak for the Resin
clear Resin
resin(:,1)=find(SS(:,3,w)>xy(9,1) & SS(:,3,w)<xy(10,1));
Resin(1,1)=max(SS((resin(1,1):resin(end,1)),4,w));
xvalue(1,5)=find(SS((resin(1,1):resin(end,1)),4,w)== Resin(1,1))...
    ;
xvalue(2,5)=resin(xvalue(1,5),1);
xvalue(3,5)=SS(xvalue(2,5),3,w);
%Finds the peak for the Phenylalanine
clear Phenylalanine
phenylalanine=find(SS(:,3,w)>xy(11,1) & SS(:,3,w)<xy(12,1));
Phenylalanine(1,1)=max(SS((phenylalanine(1,1):phenylalanine(end...
    ,1)),4,w));
xvalue(1,6)=find(SS((phenylalanine(1,1):phenylalanine(end,1)),4,...
    w)== Phenylalanine(1,1));
```

```
xvalue(2,6)=phenylalanine(xvalue(1,6),1);
xvalue(3,6)=SS(xvalue(2,6),3,w);
%Plots the spectrum
figure('position',[100 100 1000 676])
plot(SS(:,3,w),SS(:,4,w),'r-')
yvals = [phosphate(1,1), carbonate(1,1), CH2(1,1), Amide(1,1), ...
    Resin(1,1),Phenylalanine(1,1),FWHM];
intensities = yvals;
ymax = max(yvals);
axis ([800, 1800, 0, ymax+20])
%title( files(w).name)
hold on
plot(xvalue(3,1),phosphate(1,1),'k*')
text1=num2str(xvalue(3,1));
text2=num2str(phosphate(1,1));
text(xvalue(3,1)+15,phosphate(1,1),sprintf(['(' text1 ',' text2 ...
    ')']))
plot(xvalue(3,2),carbonate(1,1),'b*')
text3=num2str(xvalue(3,2));
text4=num2str(carbonate(1,1));
text(xvalue(3,2)+15,carbonate(1,1),sprintf(['(' text3 ',' text4 ...
    ')']))
plot(xvalue(3,3),CH2(1,1),'g*')
text5=num2str(xvalue(3,3));
text6=num2str(CH2(1,1));
text(xvalue(3,3)+15,CH2(1,1),sprintf(['(' text5 ',' text6 ')']))
plot(xvalue(3,4),Amide(1,1),'g*')
text7=num2str(xvalue(3,4));
text8=num2str(Amide(1,1));
text(xvalue(3,4)+15,Amide(1,1),sprintf(['(' text7 ',' text8 ')'...
    ]))
plot(xvalue(3,5),Resin(1,1),'g*')
text9=num2str(xvalue(3,5));
text10=num2str(Resin(1,1));
text(xvalue(3,5)+15,Resin(1,1),sprintf(['(' text9 ',' text10 ')'...
    ]))
plot(xvalue(3,6),Phenylalanine(1,1),'g*')
text11=num2str(xvalue(3,6));
text12=num2str(Phenylalanine(1,1));
text(xvalue(3,6)+15,Phenylalanine(1,1),sprintf(['(' text11 ',' ...
    text12 ')']))
%plot(xvalue(3,7),FWHM, 'mx')
hold on

Map(1,1)= SS(1,1,w);
Map(1,2)= SS(1,2,w);
Map(1,3)= phosphate(1,1)/CH2(1,1);
Map(1,4)= phosphate(1,1)/Amide(1,1);
Map(1,5)= carbonate(1,1)/phosphate(1,1);
Map(1,6)=FWHM;
wavenumbers=[xvalue(3,:)];
pause 5
```

9.4 X-Ray Diffraction Spectra Analyzer

Matlab m-file that calculates the full width half maximum value of x-ray diffraction spectra.

```
pathname = input('Locate the folder where files are located ');
files = dir(fullfile(pathname,'*.txt'));
lengthfiles = size(files);
lengthfiles = lengthfiles(1,1);
%w = input('input the w number ');
for w=1%[1:lengthfiles]
    fname= files(w).name;
     %[fid,message]=fopen(fname,'r','b');
     %range = [117,1,701,2]

    DELIMITER = ' ';
    HEADERLINES = 117;
    dataimported = importdata([pathname,'\',files(w).name], ...
       DELIMITER, HEADERLINES);
    data = dataimported.data;

    % data=dlmread([pathname,'\',files(w).name],'',117,1);

     [output,output_002,bestfit_211] = xrd_20110530(data)
     w

%      close figure 1
%      close figure 2
%%%%%%%%% Print information to a csv file
dlmwrite('xrd_20110628.csv', output,'-append')
sfile=fopen([pathname,'\','xrd_20110628_filenames.csv'],'a');
dims = size(output);
for k=[1:dims(1)]
fprintf(sfile,'%s,',date); % today's date
fprintf(sfile,'%s,',fname);  %reading name (filename)
fprintf(sfile,'\n'); % newline character
end
dlmwrite('xrd_20110628_output_002.csv', output_002,'-append')
sfile=fopen([pathname,'\','xrd_20110628_output_002_filenames.csv...
    '],'a');
dims = size(output_002);
for k=[1:dims(1)]
fprintf(sfile,'%s,',date); % today's date
fprintf(sfile,'%s,',fname);  %reading name (filename)
fprintf(sfile,'\n'); % newline character
end
dlmwrite('xrd_20110628_bestfit.csv', bestfit_211,'-append')
sfile=fopen([pathname,'\','xrd_20110628_filenames_bestfit.csv'],...
    'a');
dims = size(bestfit_211);
```

```
for k=[1:dims(1)]
fprintf(sfile,'%s,',date); % today's date
fprintf(sfile,'%s,',fname);  %reading name (filename)
fprintf(sfile,'\n'); % newline character
end
sfclose('all');
 end
fclose('all')
```

```
function [output,output_002,bestfit_211]=xrd_20110530(data)
%Fits XRD data by method of Posner et al. (1963) Arch Oral Biol
%Fits gaussian curves of the form a1*exp(-((x-b1)/c1).^2) and
%gets the constants a,b,c
counts = data(:,2);
theta = data(:,1);
counts_smooth = smooth(counts);
%plot(theta,counts_smooth);
%linear interpolation to subtract background around 002 peak
%between 2theta values of 25 and 27
%Find index of where t is between 25 and 27
a = find(theta==25);
b = find(theta==27);
counts_002 = counts_smooth(a:b);
theta_002 = theta(a:b);
l = length(theta_002);
x1 = theta_002(1);%mean(c_t(1:10));
x2 = theta_002(l);%mean(c_t(91:101));
y1 = mean(counts_002(1:10));
y2 = mean(counts_002(l-10:l));
m = (y2-y1)/(x2-x1);
B = y1-(m*x1);
x = theta_002;
y = (m*x)+B;
%subtract linear background
counts_002_sub = counts_002-y;
%Peak fit with a Gaussian curve 25.6 to 26.6 2theta
a2 = find(theta_002==25.4);
b2 = find(theta_002==26.6);
theta_002_fit = theta_002(a2:b2);
counts_002_fit = counts_002_sub(a2:b2);
options = fitoptions('gauss1');
options.StartPoint = [86.818, 25.8786,0.159];
options.Lower = [-Inf, 25.8785, 0];
options.Upper = [Inf,25.8786,Inf];
[cfun_002,gof_002,output_002] = fit(theta_002_fit,counts_002_fit...
    ,'gauss1');
%plot(cfun_002,theta_002_fit,counts_002_fit)
rsquare_002 = gof_002.rsquare;
cfun_002_a1 = cfun_002.a1;
cfun_002_b1 = cfun_002.b1;
cfun_002_c1 = cfun_002.c1;
```

```
%Use coefficients determined above to find the FWHM of the 002 ...
    peak
curve_fit_002 = cfun_002_a1*exp(-((theta_002_fit-cfun_002_b1)/...
    cfun_002_c1).^2);
max_index_002 = find(curve_fit_002==max(curve_fit_002));
max_value_002 = curve_fit_002(max_index_002);
halfmax_value_002 = max_value_002/2;
    %find the half max index by taking the minimum difference ...
       between the
    %halfmax value calculated and values in the ...
       fitted_002_counts vector
    diffs = abs(curve_fit_002-halfmax_value_002);
    L2= floor(length(diffs)/2);
    halfmax_index_002_a = find(diffs ==min(diffs(1:L2)));
    halfmax_index_002_b = find(diffs ==min(diffs(L2:length(diffs...
       ))));
    FWHM=theta_002_fit(halfmax_index_002_b)-theta_002_fit(...
       halfmax_index_002_a);
plot(theta_002_fit,curve_fit_002,theta_002_fit,counts_002_fit);...
    hold on
plot(theta_002_fit(halfmax_index_002_a),curve_fit_002(...
    halfmax_index_002_a),'o','MarkerSize',12,'MarkerFaceColor',[...
    .49 1 .63])
plot(theta_002_fit(halfmax_index_002_b),curve_fit_002(...
    halfmax_index_002_b),'o','MarkerSize',12,'MarkerFaceColor',[...
    .49 1 .63])
hold off
pause(2)
%linear interpolation to subtract background around 211 peak
%between 2theta values of 31 and 34.5
%Find index of where theta is between 31 and 34.5
a3 = find(theta==30);
b3 = find(theta==34.5);
counts_211 = counts_smooth(a3:b3);
theta_211 = theta(a3:b3);
l = length(theta_211);
x3 = theta_211(1);%mean(c_t(1:10));
x4 = theta_211(l);%mean(c_t(91:101));
y3 = mean(counts_211(1:10));
y4 = mean(counts_211(l-10:l));
m2 = (y4-y3)/(x4-x3);
B2 = y3-(m2*x3);
X = theta_211;
Y = (m2*X)+B2;
%subtract linear background
counts_211_sub = counts_211-Y;
%Peak fit with a Gaussian curve 31 to 34.5 2theta
a3 = find(theta_211==31);
b3 = find(theta_211==34.5);
theta_211_fit = theta_211(a3:b3);
counts_211_fit = counts_211_sub(a3:b3);
% Plot to visually check the background subtraction
```

```
plot(theta,counts_smooth,x,y,X,Y,'LineWidth',2)
pause(2)
%Fit the region 31-34.5 with 4 gaussian peaks of the same sigma,...
    vary sigma
%range from 0.5 to 1.2
beta = [.5:.01:0.9];
d = 0.0001;
for K = 1:length(beta)
    options = fitoptions('gauss4');
    lower =  [-Inf,31.7728,beta(K)-d,-Inf,32.1956,beta(K)-d,-Inf...
       ,32.9014,beta(K)-d,-Inf,34.0477,beta(K)-d];
    start = [218,31.7729,beta(K),188,32.1957,beta(K),184.76,32...
       .9015,beta(K),141,34.0478,beta(K)];
    upper = [Inf,31.7730,beta(K)+d,Inf,32.1958,beta(K)+d,Inf,32...
       .9016,beta(K)+d,Inf,34.0479,beta(K)+d];
    options.Lower = lower;
    options.StartPoint = start;
    options.Upper = upper;
    [cfun_211,gof_211,output_211] = fit(theta_211_fit,...
       counts_211_fit,'gauss4',options);

    beta(K);
    rsquare(K) = gof_211.rsquare;
    cfun_211_a1(K) = cfun_211.a1;
    cfun_211_b1(K) = cfun_211.b1;
    cfun_211_c1(K) = cfun_211.c1;

    cfun_211_a2(K) = cfun_211.a2;
    cfun_211_b2(K) = cfun_211.b2;
    cfun_211_c2(K) = cfun_211.c2;

    cfun_211_a3(K) = cfun_211.a3;
    cfun_211_b3(K) = cfun_211.b3;
    cfun_211_c3(K) = cfun_211.c3;

    cfun_211_a4(K) = cfun_211.a4;
    cfun_211_b4(K) = cfun_211.b4;
    cfun_211_c4(K) = cfun_211.c4;

%     figure
%     plot(cfun_211,theta_211_fit,counts_211_fit)
%     pause (2)
%     close figure 2

end
    %figure
    %plot(cfun_211,theta_211_fit,counts_211_fit)
o = [rsquare;cfun_211_a1;cfun_211_b1;cfun_211_c1;cfun_211_a2;...
   cfun_211_b2;cfun_211_c2;;cfun_211_a3;;cfun_211_b3;...
   cfun_211_c3;;cfun_211_a4;;cfun_211_b4;;cfun_211_c4];
output = transpose(o);
indexmax = find(output ==max(output(:,1)));
```

```
128 bestfit_211 = output(indexmax,:);
129 curve_fit_211 = (cfun_211_a1(indexmax)*exp(-((theta_211_fit-...
        cfun_211_b1(indexmax))/cfun_211_c1(indexmax)).^2))+(...
        cfun_211_a2(indexmax)*exp(-((theta_211_fit-cfun_211_b2(...
        indexmax))/cfun_211_c2(indexmax)).^2))+(cfun_211_a3(indexmax...
        )*exp(-((theta_211_fit-cfun_211_b3(indexmax))/cfun_211_c3(...
        indexmax)).^2))+(cfun_211_a4(indexmax)*exp(-((theta_211_fit-...
        cfun_211_b4(indexmax))/cfun_211_c4(indexmax)).^2));
130 plot(theta_211_fit,curve_fit_211,theta_211_fit,counts_211_fit);
131 pause (2)
132 % fit_211=(cfun_211_a1(indexmax)*exp(-((theta_211_fit-...
        cfun_211_b1(indexmax))/cfun_211_c1(indexmax)).^2));
133 % fit_112=(cfun_211_a2(indexmax)*exp(-((theta_211_fit-...
        cfun_211_b2(indexmax))/cfun_211_c2(indexmax)).^2));
134 % fit_300=(cfun_211_a3(indexmax)*exp(-((theta_211_fit-...
        cfun_211_b3(indexmax))/cfun_211_c3(indexmax)).^2));
135 % fit_202=(cfun_211_a4(indexmax)*exp(-((theta_211_fit-...
        cfun_211_b4(indexmax))/cfun_211_c4(indexmax)).^2));
136 output_002 = [rsquare_002,cfun_002_a1,cfun_002_b1,cfun_002_c1,...
        FWHM];
137 %output = [gof_002.rsquare, cfun_002.b1, cfun_002.c1, ...
        gof_211.rsquare, cfun_211.b1, cfun_211.c1,cfun_211.b2,...
        cfun_211.c2,cfun_211.b3,cfun_211.c3,cfun_211.b4,cfun_211.c4]
```